Master Thesis
Particle and Astroparticle Physics

Study of the response to isolated muons from collisions of the ATLAS Tile Calorimeter's gap/crack cells

Marco van Woerden

Supervisors:
Dr. Henric Wilkens
Dr. Ivo van Vulpen

Prof. dr. Paul Kooijman

ATLAS Experiment, NIKHEF/CERN
Universiteit van Amsterdam

CERN-THESIS-2012-085
24/04/2012

April 17, 2012

Abstract

This thesis presents a calibration study of the ATLAS Tile Calorimeter's gap/crack cells, using isolated muons from pp collisions at a center of mass energy of $\sqrt{s} = 7$ TeV and an integrated luminosity of 1 fb^{-1}. Muons, as minimum ionising particles, deposit a well-described amount of energy in the calorimeter. Therefore, they can be used to study the agreement between the measured and expected response. The $W \to \mu\nu$ events are selected using high level triggering, after which pion decay remains the main background. Dedicated studies on the TileCal calibration systems have shown that the response of the channels is time-dependent and therefore needs to be monitored. A method is proposed to determine detector modules that are miscalibrated, allowing no more than 3σ deviation from the Monte Carlo predictions. The so-called TileCal Unified Calibration Software has been improved to monitor the calibration status of the detector over time, incorporating the different calibration systems. Miscalibrations should be corrected for.

This thesis is dedicated to my family,
whom I love and cherish.

Contents

1 Introduction **5**
- 1.1 Particle physics . . . 6
- 1.2 Standard Model . . . 6
- 1.3 LHC . . . 8
- 1.4 ATLAS . . . 11

2 Calorimetry **15**
- 2.1 Passage of particles through matter . . . 15
- 2.2 Energy resolution in ATLAS . . . 16

3 Muon detection and momentum resolution **17**
- 3.1 Experimental configuration . . . 17
- 3.2 Track extrapolation algorithms . . . 17

4 ATLAS Tile Calorimeter **19**
- 4.1 Scintillating tiles . . . 19
- 4.2 Overall structure . . . 19
- 4.3 Read-out electronics . . . 21
- 4.4 Trigger system . . . 22
- 4.5 Data taking performance . . . 24
- 4.6 Fake transverse energy E_T^{fake} . . . 25

5 Calibration **28**
- 5.1 Optimal filtering . . . 28
- 5.2 Calibration of the ATLAS TileCal detector . . . 29
- 5.3 Calibration systems . . . 29
- 5.4 TUCS . . . 32

6 TileCal response using isolated muons from collisions **35**
- 6.1 Calibration of the Intermediate Tile Calorimeter in context . . . 35
- 6.2 Event selection $W \to \mu\nu_\mu$ . . . 36
- 6.3 Collision muons data and Monte Carlo samples . . . 39
- 6.4 Path length reconstruction Δx . . . 40
- 6.5 Double ratio $\frac{dE_{\text{data}}/dx}{dE_{\text{Monte Carlo}}/dx}$ . . . 41
- 6.6 Constant fit method . . . 42
- 6.7 Gaussian fit method for cell calibration . . . 44
- 6.8 Intercalibration for cells of different type . . . 48
- 6.9 Method validation by layer intercalibration . . . 48
- 6.10 Maximum likelihood method . . . 49
- 6.11 Chapter summary . . . 50

7 Effects of miscalibration on jet physics **51**
7.1 Jets . . . 51
7.2 Two jet production at the LHC . . . 52
7.3 Jet algorithms . . . 54
7.4 Sequential Clustering Algorithms . . . 54
7.5 Cone algorithms . . . 55
7.6 Jets and calibration . . . 56

8 Results **58**
8.1 Energy depositions . . . 58
8.2 ϕ-uniformity . . . 60
8.3 Calibration tables . . . 60

9 Conclusions and outlook **69**

1 Introduction

Little did Marie Curie know, when she described the faint light originating from her uranium salts. Her 1890 papers are still too radioactive to handle, the same radioactivity that eventually caused her death in 1934. Her studies led to a new understanding of matter and a reconsideration of known physics, as it seemed at the time that radioactivity violated conservation of energy. Later, radioactivity was incorporated into a new theory in physics that explained how energy could still be conserved by radioactive atoms.

Curie's story exemplifies one out of many experiments that physicists have done over the centuries, intended to establish **new physics**, as new phenomena were observed that required an explanation. Any new theory must still be consistent with older established results. In modern experiments one must first be able to reproduce the already established results to be convinced that new physics can even be found, as the experiments have increased in complexity.

This thesis was written during a **one-year Technical Studentship** at CERN. The project concerned the calibration of ATLAS's **Tile Calorimeter**. Only when we understand our detectors, we can trust what we measure and use our experiments to understand nature. This requires a great effort of experimentalists into understanding, optimising, fine-tuning and calibrating the detectors. It was my job to determine the calibration constants in a special region of the Tile Calorimeter, as will be explained.

In this introductory chapter, some terminology is introduced and the experimental conditions are described. It can be skipped by any reader already involved in the ATLAS experiment at CERN. As we are concerned with the hadronic calorimeter, the principles of calorimetry are briefly revisited in chapter 2. Chapter 3 explains how muons are detected in ATLAS. Indeed, our first job will be to reconstruct the energies of isolated muons from proton-proton collisions.

The ATLAS Tile Calorimeter encompasses **three main calibration systems** to facilitate the calibration of its hardware. As the condition of the hardware chain is time dependent, it is safe to say that one is never done with calibrating the detector. It needs continuous monitoring and correction. In chapter 4, the Tile Calorimeter is discussed in greater detail, which allows us to clarify the undertaking of calibrating such a device in chapter 5.

In chapter 6, we propose a **method** to study and improve upon the calibration, which is then further motivated in chapter 7 by describing how miscalibrations in the energy measurements affect ATLAS's ability to measure jets properly. An relevant quantity will be the response: the amount of energy E that particles deposit within a certain pathlength x in calorimeter material. It is the goal of this thesis to increase the understanding of the response of **TileCal's gap/crack cells**, which have up to now been left out of the analyses.

Chapter 8 is a display of the results, on which we finally base our conclusions and outlook in chapter 9.

1.1 Particle physics

What phenomena belong to the terrain of **particle physics**? Although this question remains a tedious matter within the community of philosophers of science - may we include the discovery of the electron by J.J. Thomson (1897) or did the concept 'electron' perhaps change over time? - the physics community has formulated a remarkably consistent answer. In **Nature** we distinguish four types of **fundamental interactions**. The **Standard Model** describes these weak, electromagnetic and strong interactions between leptons and quarks, and from this follows the prediction that all we find around us consists of these few building blocks. The constituents of matter. It is the experimental study of these constituents and the theoretical implications that make up the field we call particle physics.

What are we made of? A question that has occupied human thinking since the beginning of time. Ever since the discovery of the electron [2], the idea that one might have interacting particles[1] found great support in the modern scientific community. A mathematical model has become the Standard Model of particle physics, as its predictions on the allowed interactions and their **coupling strengths** agree well with what is observed in nature by various collider experiments at **LEP**[2] and at the **Tevatron**[3]. But also many deficiencies were found in this theory, rendering it under intense scrutiny; a rather nice overview of the physics that lies **Beyond the Standard Model** is given in Ref. [5]. Even today, the existence of dark matter, dark energy, the origin of mass, oscillating neutrinos and CP violation are not completely understood. It is clear that the Standard Model is not the theory of everything and that new physics is needed. It is the common aim of the particle physics community to discover the processes that will explain these new phenomena. The LHC[4] at CERN is currently in operation and more proton-proton collisions than ever have already been recorded by the four main experiments ATLAS, CMS, ALICE and LHCb.

1.2 Standard Model

The Standard Model can be expressed in covariant form, which means one can very well conceive a model on a curved manifold. However, when this curvature becomes sizeable with respect to the scales at which other interactions take place, the interaction amplitudes diverge and the theory becomes non-renormalizable. The electroweak and strong interactions are deemed the dominant driving forces for the behaviour of elementary particles.

The fundamental forces that have been found in nature are the electromagnetic, strong

[1] Here, one might ask what we actually mean with the word particle. In general, it is often stated that such a question can only be answered in the context of experimental feasibility. Recommended literature is to be found in Ref. [3, 4].

[2] Large Electron-Positron Collider, CERN, Geneva (Switzerand)

[3] Fermilab, Chicago (United States)

[4] Large Hadron Collider

and weak force, and gravity[5]. The Standard Model comprises the first three, by unifying the quantum field theories that describe them. This requires the introduction a higher symmetry. The Standard Model is based on the $SU(3) \times SU(2) \times U(1)$ gauge group.

The Standard Model constituents of matter are the fundamental spin-$\frac{1}{2}$ particles[6]: **quarks** and **leptons**. These are arranged in three families. They interact through mediators, which are spin-1 particles. They are tabulated in Table 1.

fermions	**1**	**2**	**3**	**mediating vector boson**
quarks	u	c	t	strong (g), weak ($W^{\pm}$, Z), EM (γ)
	d	s	b	
leptons	ν_e	ν_μ	ν_τ	weak
	e	μ	τ	weak, EM

Table 1: The Standard Model fermion families and corresponding mediating vector bosons.

The **electromagnetic force** is classically described as the force that is exerted by one charged particle on another charged particle. In the context of the Standard Model, photons mediate this force between leptons and quarks, but leave the chargeless neutrinos untouched. The **weak force**, mediated by the $W^{\pm}$, Z bosons, is often associated to particle decay, as it is responsible for the β decay of atomic nuclei and it is involved in CP violating decay processes. A weak decay that may serve as a background to many interesting physics signal in experimental high energy physics is $\pi^{\pm} \to \mu^{\pm} + \nu_\mu$. Here, ν_μ stands for the anti-muon-neutrino in case of a negatively charged pion. The **strong force** is the short ranged force that bonds neutrons and protons in atomic nuclei, mediated by gluons. In effect, it is the force that is mediated between all coloured particles, namely quarks, which come in three flavours f, and three colours c, and gluons. In the colour classification scheme, there exist eight different gluons. Its quantum field theory, called quantum chromodynamics (QCD), is especially of interest at hadron colliders, as the hard scattering process that follows a collision is governed by the strong force. Moreover, experimentalists will be confronted with **jets**. These arise naturally in hadron colliders and electron-positron colliders, due to the presence of a high flux of **hadrons** coming from the interaction point, moving in similar directions. They are produced by strongly interacting particles which radiate quark pairs and gluons.

[5]Gravity is not described by the Standard Model, but by general relativity, which provides a classical picture of the universe. At the reduced Planck scale $m_{\mathrm{P}} = \sqrt{\hbar c/8\pi G} \approx 2.4 \cdot 10^{18}$ GeV, these two theories are expected to merge. See Ref. [6].

[6]All matter in the Standard Model is fermionic by construction. In the 80's, the theory of supersymmetry (SUSY) was suggested as a solution to various theoretical problems: most notably to finally resolve the issue of the huge differences in coupling strengths amongst the fundamental forces of nature. The new fermions introduced by SUSY have not been observed to date. It remains the theorist's freedom to postulate new theories that encompass new (non-Standard Model) spin-$\frac{1}{2}$ particles. The interested reader is referred to [7].

The Standard Model theory is formulated in terms of a scalar **Lagrangian** on which one applies the **action principle** to obtain the Lorentz invariant equations of motion for the fermion fields. In other words, the same description of the dynamics still applies when moving to a different reference frame by means of a Lorentz transformation. In flat spacetime, one can always find a tensor representation $\Gamma^{\mu'}_{\nu}$ to transport a quantity $x^{\mu'}$ from S to S' by $x^{\mu'} = \delta^{\mu'}_{\mu}\left(\Gamma^{\mu}_{\nu}x^{\nu} + a^{\mu}\right)$. In general, the identity transformation, boosts and spacial translations and rotations are Lorentz transformations.

Conservation laws require the theory to be local gauge invariant under $SU(3)_C \times SU(2)_L \times U(1)_Y$ transformations. Generators of the associated symmetry group are called **gauge fields** to stress that there is redundancy in the Standard Model. By fixing the gauge, one fixes the number and nature of the degrees of freedom. The predictions based on the Standard Model should remain invariant under local gauge transformations. This gauge invariance implies that all particles in the model are massless. The quanta associated to these gauge fields are interpreted as the force mediating gauge bosons.

Spontaneous symmetry breaking is introduced to generate some mass, by allowing a scalar (spin-0) field ϕ with potential $V(\phi)$ to interact with other gauge fields. The quantum related to this additional field is named after professor Peter Higgs, who came up with this so-called **Higgs mechanism**. [83–86] Through this mechanism, one also assigns **mass to the heavy W and Z bosons** for example, which is deemed so important that the search for the Higgs boson now serves as one of the leading justifications used to advocate for the construction of the LHC.

The Lagrangian that governs the electroweak part of the model is nicely revisited in Ref. [8]. An extensive overview of how the dynamics are described in terms of these Lagrangians is given in Ref. [9,10]. In the scope of this study, it suffices to trace down the term that describes the **charged current** interactions, which includes the coupling of the $W^{\pm}$ bosons to leptons l and ν_l and the u and d quarks.

$$\begin{aligned} \mathcal{L}_{cc} &= \tfrac{g}{2\sqrt{2}} W^{\dagger}_{\mu}\left(\bar{u}\gamma^{\mu}(1-\gamma_5)d\right) \\ &+ \tfrac{g}{2\sqrt{2}} W^{\dagger}_{\mu}\left(\bar{\nu}_l\gamma^{\mu}(1-\gamma_5)l\right) + \text{h.c.} \end{aligned} \tag{1}$$

Fermionic (spin-$\frac{1}{2}$) fields ψ are described by the Dirac equation.

$$\left(-i\gamma^{\mu}\partial_{\mu} + m\right)\psi = 0 \tag{2}$$

Here, the mass of the fermion m and gamma matrices γ^{μ} are expressed in natural units, $\hbar = c = 1$, often used for convenience in high energy particle physics.

1.3 LHC

CERN, *Organisation Européenne pour la Recherche Nucléare* (European Organization for Nuclear Research) was founded to facilitate the research on the properties of the smallest constituents of matter by colliding high energetic particles. In November 2009, the LHC colliding **proton beams** were running at $\sqrt{s} = 900$ GeV. At the time, ATLAS published its first physics results on charged particle multiplicities in proton-proton collisions. Ref. [11]. As of March 2010, its Large Hadron Collider (LHC) has reached center-of-mass energies up to $\sqrt{s} = 7$ TeV and will be ramped up to 14 TeV in the coming years.

Protons are freed from a bottle of hydrogen gas in a system commonly referred to as the duoplasmatron ion source, at the very beginning of CERN's second linear accelerator, the LINAC-2. The first 50 MeV proton beams were produced in 1978 and since then they have served as injection beams for the Proton Synchroton (PS) via the PS Booster (PSB). At the time, the PS had already been in operation for almost twenty years. It functioned as direct feeder for experiments, as well as for the larger 400 GeV Super Proton Synchroton (SPS), which was completed in 1979. Some overview of the **injector complex** for the recently constructed LHC (2008) is given in figure 25.

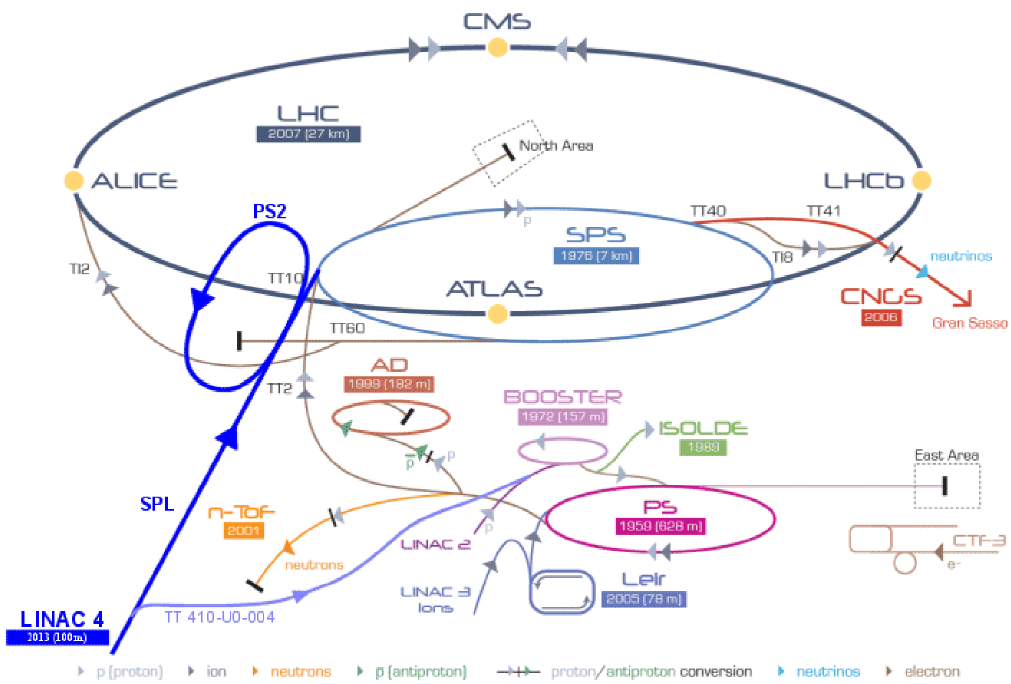

Figure 1: Schematic of the CERN accelerators and the pathways for different types of particles. The new linear accelerator (Linac4), depicted in bright blue, is yet to be completed.

The beam injection scheme for the LHC is rather complicated, as the **proton bunches** are also used to feed various other non-LHC experiments in different stages of the acceleration process. For example, the On-Line Isotope Mass Separator (ISOLDE) experiment is provided with beam by the proton-synchroton, as explained on their official web page [12].

In January 2011, the beam energy was still 3.5 TeV instead of the nominal 7 TeV as more dipole safety was required before going to higher energies. Operating at lower energies also has consequences for the operation safety of the quadrupole magnets used to squeeze the beam. Squeezing is necessary to obtain high collision rate. The quantity[7] that measures how much the beam is squeezed at the interaction point under optimal conditions is denoted as $\beta*$. The nominal energy has not been implemented to date, despite the planning, as can be found in Ref. [13]. The time interval between each interval $\Delta t_{\text{bunches}} \geq 150$ ns has been used during the 2010 runs. While the bunch crossing time is decreased to 75 ns with a total number injected bunches of 950, the "refresh time" needed between each injection has increased to ensure optimal vacuum conditions have been reached. From table 2 we may conclude that the LHC beam parameters have yet to reach their nominal values.

parameter	**value at injection**	**value at collision**
proton energy (GeV)	450	7000
relativistic γ^1	479.6	7461
number of particles/bunch	1.15×10^{11}	1.15×10^{11}
number of bunces	2808	2808
longitudinal emittance^2 (eVs)	1.0	2.5
circulating beam current (A)	0.582	0.582
stored energy per beam (MJ)	23.3	362
peak luminosity in ATLAS ($\text{cm}^{-2}\text{s}^{-1}$)		1.0×10^{34}
peak luminosity per bunch crossing in ATLAS ($\text{cm}^{-2}\text{s}^{-1}$)		3.56×10^{30}
events per bunch crossing		19.02
inelastic cross section (mb)	100.0	100.0
total cross section (mb)	60.0	60.0
beam current lifetime due to beam-beam interaction (h)		44.86
luminosity lifetime due to beam-beam interaction (h)		29.1
beam lifetime due to rest-gas scattering (h)	100	100
beam current lifetime (h)		18.4
luminosity lifetime (h)		14.9
synchroton power loss per proton (W)	3.15×10^{-16}	1.84×10^{-11}
synchroton power loss per meter of main bending (W/m)	0.0	0.206
energy loss per turn (eV)	1.15×10^{-1}	6.71×10^{3}

Table 2: LHC nominal beam parameters, as defined in Ref. [14].

As of June 2011, an integrated luminosity of about 1 fm^{-1} has been recorded by ATLAS (and CMS), as displayed in figure 2.

[7]One may write the actual beam size as $\sigma(s) = \sqrt{\beta(s)\epsilon}$, where $\beta(s)$ is the optical lattice function, obtained from solving the Hills equation, and ϵ is the beam emittance.

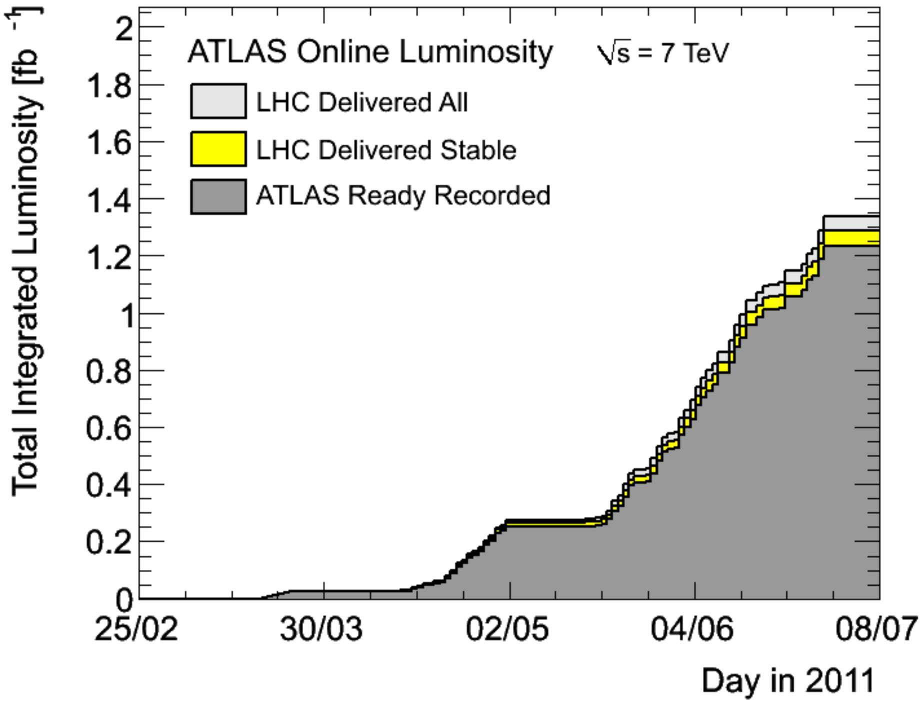

Figure 2: Integrated luminosity recorded by ATLAS as a function of time, as calculated from the values stored in the COOL database for each lumiblock. A lumiblock represents approximately 30 seconds of data-taking.

1.4 ATLAS

The **ATLAS**[8] **detector** is a multi-purpose detector operated at the Large Hadron Collider at CERN, which utilises over 60 million electronic channels to record the signals of particles produced in proton-proton collisions. ATLAS's dimensions are 25×46 meters, having an overall weight of 7000 tonnes it is the largest of the four experiments built for the LHC. Detecting the large numbers of particles passing through is a huge experimental challenge, as the equipment is required to be able to withstand the high dosage of radiation that it receives during its operation. Moreover, the time scales at which the readout electronics operate are small, in the order of 40 MHz. An important feature is the magnetic field generated by the inner **solenoid** that surrounds the inner detectors and the outer **toroidal magnets** that are located beyond the calorimeters.

A new cavern was excavated at **point 1**. The main construction reached its completion in 2004. A schematic overview of the experimental site is provided by figure 3.

[8]The acronym stands for **A** **T**oroidal **L**HC **A**pparatus. Ref. [15].

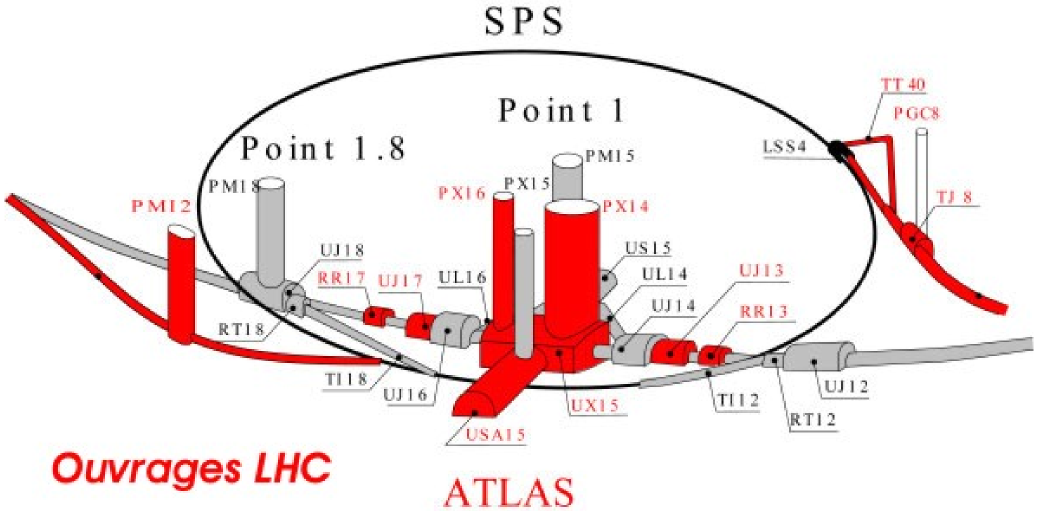

Figure 3: Point 1, the experimental grounds and cavern for ATLAS, the only detector that was built on Swiss soil in close vicinity to the SPS. Protons injected into the LHC will reach the ATLAS detector only after traversing the full collider ring.

The **ATLAS coordinate system** (x, y, z) that is most used is defined with x pointing towards the center of the LHC ring and the y axis pointing vertically upwards, slightly tilted with respect to the overall normal vector that defines the LHC plane. The z coordinate points in the direction of the beam pipe and distinguishes the A-side $(z > 0)$ from the C-side $(z < 0)$. In addition, the cylindrical symmetries of the detector sometimes lead us to use the cylindrical coordinate system $(r, \phi, z) = (\sqrt{x^2+y^2}, \arcsin y/\sqrt{x^2+y^2}, z)$ $(x \geq 0)$. The origin of the coordinate system is the **interaction point**.

Moving outwards from the interaction point, a particle passes the pixel detector, the inner detector, the electromagnetic liquid argon calorimeter (LAr), the hadronic tile calorimeter (TileCal) and the muon chambers. Each system is dedicated to a different measurement that contributes to the final event reconstruction.

Inner detectors

The inner detector consists of the silicon pixel detector (SPD), semiconductor tracker (SCT) and transition radiation tracker (TRT). The purpose of the inner detectors is to detect and localise passing charged particles. This data is used to extrapolate the tracks through the remainder of the detector. The three layers of the SPD contain 80 million pixels, sized 50×400 μm. The SCT, which has 6 million readout channels, records the positions of charged particles to an accuracy of 17 μm per silicon layer. The outer part of the inner detector is the TRT, which utilises straw tubes of diameter 4 mm as a basic detector element. This detector is capable of identifying charged particles that pass by.

The 2 T solenoidal field enables the inner detector to measure the momentum of charged particles independently.

Calorimeters

Calorimeters measure the energy of incoming particles. In order to measure the energy deposits, one needs a system that produces an output signal which has a (linear) dependence on the input. ATLAS's calorimetry is divided into electromagnetic (ECAL) and hadronic (HCAL) calorimeters.

In ATLAS's **liquid argon** (LAr) calorimeter, the electromagnetic calorimeter (ECAL), liquid argon is used as active material as many $e - \mathrm{Ar}^+$ pairs are produced when electrons and photons shower in the calorimeter material [21]. The freed charges are then collected in the electrodes, thus forming a current in the readout electronics. The LAr detector is especially sensitive to electromagnetic interactions, and may therefore be used to measure the energies of electrons and photons. Lead is used as absorber material for the electromagnetic showers that occur during proton-proton collisions. The barrel part extends to $|\eta| < 1.5$ and the two endcaps range $1.4 < |\eta| < 3.2$. A high energy electromagnetic shower is well contained in $25X_0$ [22], as the average energy loss may be modelled by $\bar{E} = E_0 \exp(-X/X_0)$ [23]. The **interaction length** X_0 is an important design parameter for any (sampling) calorimeter.

The LAr calorimeter is able to **distinguish photons from electrons**, aided by the inner detector and its three inner layers, which exhibit a finer granularity. Their energies are reconstructed using a method in which the energies measured by the different layers in the calorimeter are weighted and summed,
$E_{\mathrm{reco}} = A\,(B + W_{\mathrm{presampler}} E_{\mathrm{presampler}} + E_1 + E_2 + W_3 E_3)$. In the crack/gap region, a special parametrisation is applied. $E_{\mathrm{reco,gap}} = A\,(B + E_b + E_e + W_{\mathrm{scint}} E_{\mathrm{scint}})$. Here $E_{\mathrm{presampler}}$ is the cluster energy in the presampler, E_i the energy in layer i, E_b the cluster energy in the barrel calorimeter and E_e the cluster energy in the end-cap calorimeter. The fit parameters A,B,$W_{\mathrm{presampler}}$ and W_3 are obtained by a χ^2 minimisation of $(E_{\mathrm{true}} - E_{\mathrm{reco}})^2/\sigma(E_{\mathrm{true}})^2$.

The **Tile Calorimeter** is ATLAS's hadronic calorimeter (HCAL). Its main purpose is to measure the energies and directions of jets from hadronised quarks and hadronically decaying particles. It consists of steel plates and scintillating tiles, hence its name. The Tile Calorimeter is further described in chapter 3, as this thesis is concerned with the calibration of this detector specifically, using muons from W decay.

Muon spectrometer

The muon spectrometer serves two main purposes, namely triggering on muon signals and reconstructing muon tracks. The muon chambers are situated within the layer of toroidal magnets. The magnetic field is necessary for the momentum measurement of charged particles, as they are bent by the Lorentz force[9] without introducing an acceleration component in the direction of flight.

In a **combined event reconstruction**, the muon track is extrapolated[10] from the inner detector to the muon spectrometers, combining the **standalone measurements**[11] of either system. The extrapolation must take into account the detector geometry, as well as multiple scattering and energy loss in the calorimeters, and is only successful if the inward and outward extrapolated tracks can be matched, using a quantity $\chi^2 = (T_{\mathrm{MS}} - T_{\mathrm{ID}})^{\mathrm{T}}(C_{\mathrm{ID}} + C_{\mathrm{MS}})^{-1}(T_{\mathrm{MS}} - T_{\mathrm{ID}})$, where T_{MS} and T_{ID} are five-dimensional vectors that parametrise the extrapolated tracks and C_{MS} and C_{ID} are the corresponding covariance matrices. Ref. [19].

Figure 4: This artist's impression of ATLAS decorates the ATLAS Control Room building at point 1. The cylindrical shape of the detector can be appreciated at a distance, as the mural tricks the admirer into thinking that the image is 3D. Thousands of tourists take pictures of this painting every week.

In the literature one often finds the **pseudorapidity** η, defined only by the polar angle θ with respect to the beam pipe: $\eta = -\ln \tan \frac{\theta}{2}$.

[9] $p = qBR$ is also known as the cyclotron formula. The force exerted on the particle q by field B does no work, but leads it to move, locally, in a circular orbit with radius R.

[10] The algorithms used for this procedure are called Muonboy (inward) and Moore (outward), Ref. [20].

[11] These measurements consist of connected line segments.

2 Calorimetry

In this section, we briefly discuss the basic principles of calorimetry, for reference.

2.1 Passage of particles through matter

Whenever a particle passes through matter, it may loose a fraction f of its energy through various different physics processes, like ionisation and scatterings. The fraction f is dependent on the particle's initial energy E, the path length Δx and the particle type, which determines the rate of energy loss. The **interaction length** is the path over which a particle looses $\frac{1}{e}$ of its energy. See Ref. [17].

$$f \approx \Delta x \tfrac{dE}{dx} / E \tag{3}$$

For **heavy charged particles**, the energy loss is dominated by ionisation. This behaviour modelled by the Bethe-Bloch formula.

$$-\frac{dE}{dx} = K z^2 \frac{Z}{A} \frac{1}{\beta^2} \left(\frac{1}{2} \ln \frac{2mc^2\beta^2\gamma^2 T_{\max}}{I^2} - \beta^2 - \frac{\delta}{2} \right) \tag{4}$$

Here, $K = 4\pi N_A r_e^2 m_e c^2$ is constant, $Z = \frac{q}{e}$ the charge of the particle, Z the atomic number of the absorbing matter, A the atomic mass of the absorber in gmol^{-1}, $\beta = \frac{v}{c}$ and $\gamma = 1/\sqrt{1-\beta^2}$ the relativistic kinematic variables, m the mass of the particle, T the kinetic energy, I the mean excitation energy in eV and δ the density effect correction to ionisation energy loss.

Electrons show a different behavior, as the ionisation effect becomes negligible in comparison to the emission of Brehmsstrahlung[12]. This effect is quantified independent of the particle's mass[13].

$$-\frac{dE}{dx} = 4\alpha N_0 \frac{Z^2}{A} r_e^2 E \ln \frac{183}{\sqrt[3]{Z}} \approx \frac{E}{Z_0} \tag{5}$$

For **photons**, the interactions with matter are dominated by the photoelectric effect ($\gamma + N \to N^+ e^-$), Rayleigh scattering ($\gamma N \to \gamma N$), Compton scattering ($\gamma e^- \to \gamma' e'^-$) and pair production ($\gamma \to e^+ e^-$). One models the energy attenuation by evoking the Beer-Lambert-Bouguer law.

$$I = I_0 \exp(-\kappa x) \tag{6}$$

[12] In the literature, one often finds $e \to e\gamma$. However, this interaction is prohibited by conservation of four-momentum, unless $E_\gamma = 0$. The radiation of Brehmsstrahlung only occurs in the presence of some other massive particle N, like $eN \to eN'\gamma$. Here, N could be an atomic nucleus that is slowing the electron down by interacting with it. **Bremsen** is the German word for slowing down.

[13] The fine structure constant is defined as $\alpha = e^2/4\pi\epsilon_0\hbar c$.

This formula can be used to retrieve the interaction length of a single photon in a medium with attenuation coefficient κ, namely $X_\gamma = \kappa$.

2.2 Energy resolution in ATLAS

To do physics, we need a list of energy-momentum **four-vectors** $(E, \mathbf{p})$ for all physics objects under study. One might wonder what the precision of the energy and momentum measurement is for particles crossing ATLAS. Let E be the measured energy, given in GeV. Equation 7 is expected to describe the **energy resolution** for (low-energetic) jets. See Ref. [19].

$$\frac{\sigma_E}{E} = \frac{50\%}{\sqrt{E}} \oplus 3\% \tag{7}$$

For photons and electrons, we have a much better resolution.

$$\frac{\sigma_E}{E} = \frac{10\%}{\sqrt{E}} \oplus 0.5\% \tag{8}$$

The basic idea is that one can determine the energy by measuring the track path through the detector Δx and the deposited energy ΔE in the detector active material. If the **stopping power** of the detector is great enough, one may find $E \approx \frac{\Delta E}{f}$ ($f \neq 1$ for a **sampling calorimeter**). This may happen to electrons showering in the electromagnetic part of the detector.

Muons have a relatively high probability of passing the detector with a lower energy loss, which makes it tedious to measure their energies: ΔE and E do not correlate very well for muons. Below 100 GeV, the muon's energy loss is dominated by ionisation. Radiative effects play a role for high energetic muons and their resolutions strongly depend on the resolution of the muon system. The total energy loss is described by the following phenomenological expression.

$$E_{\text{loss}} = a_0 + a_1 \ln p_\mu + a_2 p_\mu \tag{9}$$

3 Muon detection and momentum resolution

In the interest of this study, muons from pp collisions were used to study TileCal's calibration. This chapter elaborates on the various strategies in ATLAS to identify and reconstruct muons.

3.1 Experimental configuration

The ATLAS muon spectrometer has been measured to have a mean resolution on the muon momentum measurement of 4% around $30-60$ GeV. The technology used here is that of drift tubes filled with a pressurised CO_2/Ar gas mixture, in which ionisations occur when charged particles pass. The so-called Monitored Drift Tube (MDT) detectors provide muon tracking at a resolution of $\frac{\Delta p_T}{p_T} < 12\%$ for $p_T < 1$ TeV. Ref. [28]. In principle, a MDT measures the time t_D for a ionisation charge to arrive at the wire in a drift tube, which results in a track resolution determination of 80 μm. To do the momentum measurement, one compares information of typically three MDT chambers. [29]

The combined SPD, SCT and TRT inner detectors of ATLAS measure tracks up to $|\eta| < 2.5$. In fact, the transition radiation tracker covers $|\eta| < 2.0$, which means that the standalone momentum measurement in the region $2.0 < |\eta| < 2.5$ is done by the silicon pixel detector, closest to the interaction point, and the silicon strip detector that surrounds it. The interpolated hits from which tracks are formed can be traced back to the interaction point with a precision of 15 μm in the (x, y) plane. A large effort goes into understanding and monitoring the positions of the detector components, as this affects the reconstruction efficiency. The achieved momentum resolution, using silicon chips, straw tubes and intelligent track software, equals $\frac{\Delta p_T}{p_T} = 0.04\% \oplus 2\%$. Ref. [30].

At the level of the calorimeters, muons are mainly distinguished from other particles by their energy signature and track range. A muon deposits $O(1)$ GeV/m in the ATLAS calorimeters. This corresponds roughly to the minimum value for the ionisation as described by the Bethe-Bloch formula in equation 4. Collision muons behave like **minimum ionising particles**. Ref. [17].

3.2 Track extrapolation algorithms

Standalone muons are reconstructed using only the hits in the muon spectrometer, which are connected to form a segmented track and then extrapolated back to the beamline. Two algorithms, called Muonboy (Staco family), see Ref. [31], and Moore (Muid family), see Ref. [32], are employed, both taking into account energy losses and multiple scatterings in the calorimeters. Muons produced in the calorimeters through particle decay cannot be distinguished from the collision muons when a standalone reconstruction is used.

Combined muons are obtained by refitting the tracks obtained with standalone methods combined with an additional outward extrapolation from the inner tracker to the muon system. Due to the size of the inner tracker, the η coverage is limited to $|\eta| < 2.5$. The purity of the sample of hard scattering[14] muons increases, as muons created in the calorimeter cannot be matched to a track seen by the inner detector and therefore vanish.

Example. Muons from $J/\Psi \to \mu\mu$ are detected by Muonboy with an efficiency of 76.4% and a **fake rate** of 51 μ_{fake} per 1000 events above 3 GeV. In a combined measurement, using the same Staco family algorithms, the efficiency of good reconstructed muons from J/Ψ decay rises to 87.3%. The fake rate is significantly reduced to 0.9 μ_{fake} per 1000 events above 3 GeV.

Muon tracks that are inside jets or in the vicinity of other tracks are less likely to be reconstructed properly by the inner tracker. This means only the standalone information provided by the outer muon system can be taken into account in the computation, which produces a less accurate energy measurement. Also in the regions $2.5 < |\eta| < 2.7$, one abandons the requirement that a track in the muon spectrometer can be matched to a track in the inner detector. Some momentum resolution is sacrificed, but one takes this change in resolution into account by introducing a systematic error, and some information on the muon momentum is gained. Ref. [33].

[14] Hard scattering muons that originate approximately from the interaction point and can be seen as direct products of the proton-proton collisions.

4 ATLAS Tile Calorimeter

The ATLAS **Tile Calorimeter** [15, 39] is the hadronic sampling calorimeter in ATLAS that extends from an inner radius of 2280 mm to a outer radius of 4250 mm. It utilises **scintillator material** and steel plates as active and passive materials, respectively. The tiles are placed in the radial direction.

In this section, we will first describe these scintillators and the overall structure, after which we proceed to a discussion about the readout electronics. As the Tile Calorimeter is part of the trigger system, we describe the three trigger levels in ATLAS. Finally, we discuss TileCal's datataking performance.

4.1 Scintillating tiles

A scintillator has luminescent properties when excited by charged particles, basically converting a fraction of the particle's energy into a flash of light. The PTP material used in the tiles absorbs light induced by the ionising particles at the wavelength range of 240 to 300 nm and emits light in the range of 320 to 400 nm. This will then again be absorbed by a second material in the scintillating mixture, called POPOP, which emits light within the visible range (410 nm, ultra violet). The light is then transported[15] and shifted to an even longer wavelength through wavelength shifting (WLS) fibres. Photo multiplier tubes (PMTs) finally detect the light, converting it into an electronic signal. The cathode of the PMT produces electrons, which are then accelerated towards the dynodes. On direct impact, these dynodes emit secondary electrons, which are further accelerated in the electrode chain. Finally, the electrons reach the anode, where the current has become sizeable. The **gain** of a PMT is defined by $G \equiv I_{\text{anode}}/I_{\text{cathode}}$. See Ref. [41]. Approximately 460.000 scintillating tiles were used, as well as 1120 kilometes of WLS fibre.

4.2 Overall structure

The metal structure that supports the detector components, commonly referred to as the girder, also houses the readout electronics for each **module**. TileCal is highly periodical. There is a long barrel (LB) and two extended barrels (EBA/EBC), each divided up into 64 independent modules along the azimuthal direction. A module contains 48 channels, corresponding to less than 24 cells. The 45 PMTs belonging to each long barrel module are connected to 22 (A-side) and 23 (C-side) cells. The central D0 cell extends into both sides, connected to two PMTs of either drawer. For the extended barrels, the 45 PMTs are used to readout 18 cells on both sides. In total, there are $22 + 23 + 18 + 12 = 81$ cells in each segment in ϕ. In figure 5, an individual TileCal module is depicted.

[15]There is no optical leakage if the light propagates with a surface angle less than the critical angle $\theta_c = \arcsin \frac{n_{\text{air}}}{n_{\text{tile}}}$. See Ref. [40].

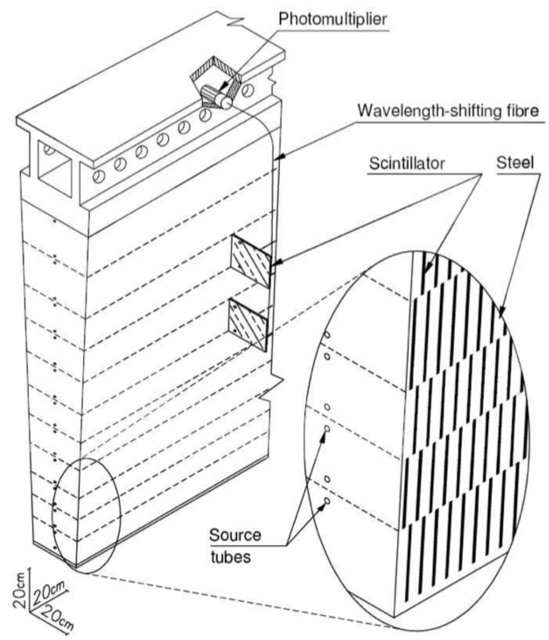

Figure 5: One of the 64 TileCal modules and its optics. A scintillating tile is readout by two separate PMTs to provide redundancy that may later be needed. There exists a total of 9852 PMTs. [42].

For technical and practical reasons, a 600 mm gap is left between the barrels and the extended barrels. Cables from the inner detectors and LAr calorimeter run though here, as well as some electronics and other services. Nevertheless, TileCal fully covers the pseudorapidity range of $|\eta| < 1.7$, with the barrel covering the region $|\eta| < 1.0$ and the extended barrel $0.8 < |\eta| < 1.7$.

Any gap in the detector material may decrease the probability that some physics process will be reconstructed properly, as a hadronic shower may not be fully contained within the detector space. Less detector material will contribute to the systematic error of the measurement. In an effort to minimise this error, additional ladder shaped cells were installed at the edge of the extended barrel: C10, D4, gap scintillators E1/E2 and crack scintillators E3/E4. Figure 6 represents a mapping of PMTs to cells.

The minimum absorption length $5X_0$ occurs at $|\eta| \approx 0.8$, which is increased to $7X_0$ by the installation of the ITC (Intermediate TileCal) plug. The hadronic showers are maximally absorbed at $|\eta| \approx 1.2$, where the absorption length equals approximately $14X_0$. The girder contributes an overall $2X_0$, virtually independent of η.

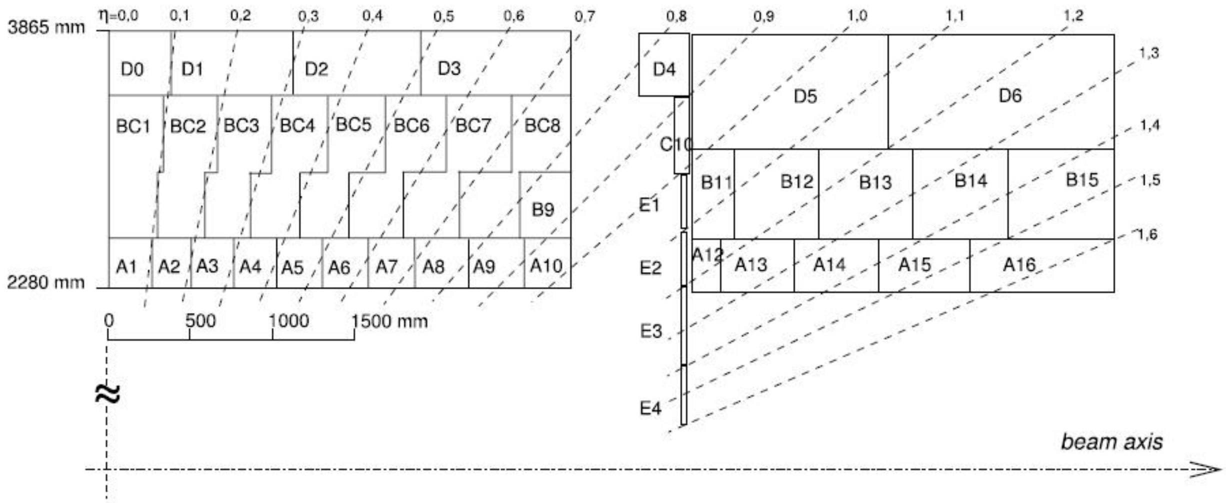

Figure 6: TileCal cell map. Each module consists of 81 cells each of which may correspond to one or more readout PMTs.

4.3 Read-out electronics

Electronics is needed to convert the scintillation light from the tiles into a measurable electronic signal. The purpose of this subsection is to give a brief overview of the read-out electronics.

TileCal's **front-end electronics** is assembled into a device called the **PMT block**. See Ref. [43]. The WLS fibres interface with the PMT by means of a **light mixer**. This light guide mixes light in a uniform, diffuse manner. As the PMT response may not be uniform over its photosensitive surface, mixing the light helps reducing the influence of fibre location at the photocathode. Naturally it needs to be shielded from other light sources, most notably Čerenkov light from incoming particles. The analogue PMT signal is then transported to a **high gain (HG)/low gain (LG) splitter** and a **3-in-1 card**. The entire structure that supplies a high voltage to the PMT gain dividers and a low voltage to the 3-in-1 card is often indicated by the term **superdrawer**. During data-taking, the main purpose of the 3-in-1 card is to shape and amplify the PMT pulses to accommodate the needs of the electronics further down the read-out chain. For calibration and monitoring purposes, charge injection calibration and slow (typical timescale is ms) integration of the PMT current output are added to the card's functionalities. See Ref. [44].

The entire PMT block is shielded from ATLAS's strong magnetic fields by a cylindrical soft iron and mu-metal casing. A 3 mm thick soft iron end-cap closes the PMT block.

Up to 48 PMT blocks are grouped by the superdrawers, which also house the electronic mother boards needed for triggering. There are two drawers for each barrel module and one for each extended barrel module. The front-end electronics and the low voltage power supplies (LVPS) are both located on the calorimeter, withstanding a severe exposure to radiation and magnetic fields. Ref. [21].

The LG and HG signals are retrieved from the circuit boards at a frequency of 40 MHz, which corresponds to the LHC bunch crossing time of 25 ns = 1/(40MHz). A 10-bit analog-to-digital converter (ADC), located in the Data Management Unit (DMU) chip, digitises the PMT pulse peaks, which are then sent via optical fibres to the back-end electronics.

Subsequently, the timing of the pulse is determined on the **digital signal processor** (DSP) and in the offline reconstruction. The pulse peak timing resolution should be 1 ns for a good energy reconstruction. In figure 7, the cell time distribution is shown.

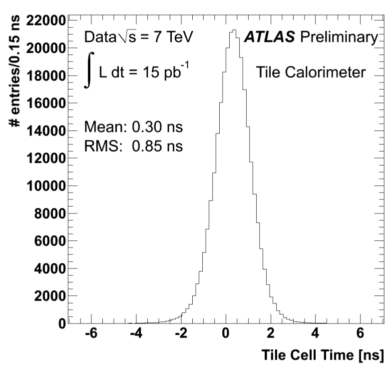

Figure 7: Tile Calorimeter cell time distribution, using jet events with $p_T > 20$ GeV and cells with $E_{\text{cell}} > 20$ GeV. Ref. [48].

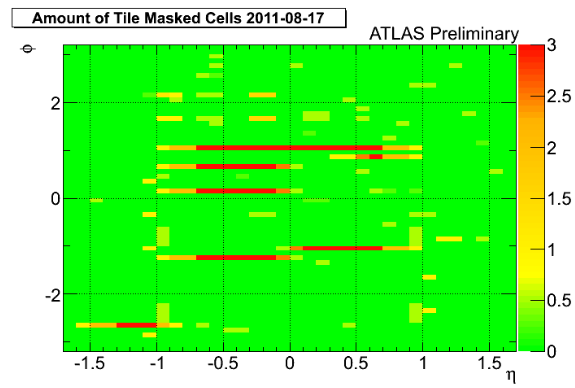

Figure 8: (η, ϕ) overview of the integrated number of masked cells in a calorimeter tower, indicated by the colors.

4.4 Trigger system

Which events do we store? This is the basic question that one tries to answer in the practice and application of trigger systems. Clearly, the particle physics community has matured since the era of the cloud and bubble chambers, which started barely a century ago. New technologies are at the disposal of the experimentalist. The microscopic bubble tracks left by charged particles in a superheated fluid have been replaced by three-dimensional electronic tracks. The photographic read-out has been replaced by vast amounts of digitised data. Even though the latter form of information has many advantages over the numerous photographs that one needed to accumulate for the physics analysis in the past, some new technological challenges arose. There are approximately 10^9 collisions in ATLAS every second, equivalent to a data rate of 1 PB/s. With current technology, one can only store 300 MB/s. Only a fraction of 10^{-5}% of the events should be allowed to be stored.

In general, a **trigger system** is designed to rapidly decide whether an event in a particle detector meets a set of predefined requirements. ATLAS has been designed to have a powerful trigger, that takes **logical decisions** at three levels.

The **first level** (L1) trigger is completely hardware based and looks for signatures of high p_T muons, electrons, photons, jets and other signs of interesting physics at a rate of $75 - 100$ kHz. This implies the system mainly cuts on the multiplicity of these physics objects in the detector and the value of $E_T - E_T^{\text{miss}}$. The data rate is reduced to about 160 GB/s. The status of **Region of Interest** (RoI) is consequently assigned to any small detector region in pseudorapity and angle that complies to the L1 trigger requirements. A $2_\eta \times 2_\phi$ RoI may be centered around a LAr tower cluster that has a local E_T maximum. The L1 **muon trigger decision** is made based upon input from the resistive plate chambers (RPC) for $|\eta| < 1.05$ and the thin gap chambers (TGC) in the endcaps. The information of all ATLAS's channels is stored during 2.5 μs, which is the time the system needs to take a trigger decision, the **latency**. In figures 9 and 10, the L1 muon trigger efficiencies are shown.

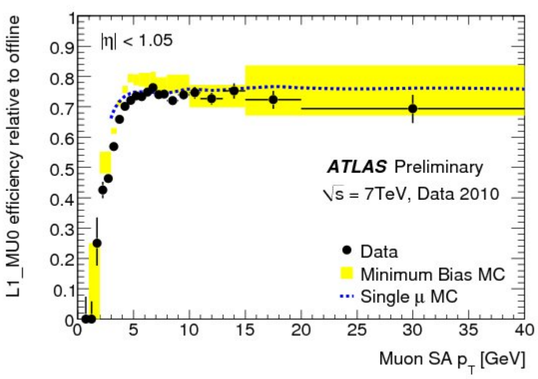

Figure 9: Efficiency of the L1 muon trigger system in the barrel region $|\eta| < 1.05$ as a function of transverse momentum p_T from offline spectrometer-only reconstructed muons, extrapolated to the interaction region. The efficiency is calculated with respect to offline reconstructed combined muons, using spectrometer and the inner detector.

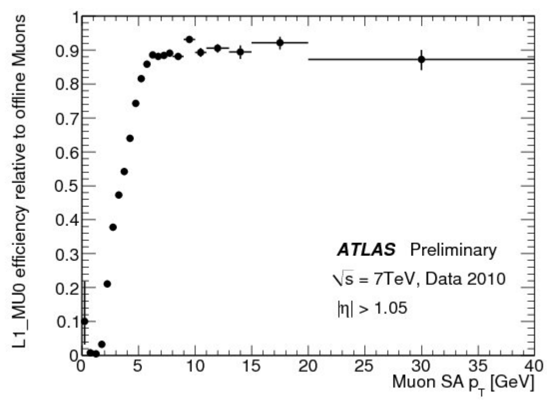

Figure 10: Efficiency of the L1 muon trigger system in the endcap region $|\eta| > 1.05$ as a function of transverse momentum p_T from offline spectrometer-only reconstructed muons, extrapolated to the interaction region. The efficiency is calculated with respect to offline reconstructed combined muons, using spectrometer and the inner detector.

In case of a L1 accept, the output data is read-out by Read-Out Drivers (RODs) and stored in Read-Out Buffers (ROBs). The RoIs are sent to the **second level** (L2) trigger, which uses the L1 output as input. The L2 trigger is software based, using 500 processors in an effort to reduce the data rate to 5 GB/s. Only volumes in the RoIs are used. The latency is 10 ms. A fast pattern recognition algorithm is at work at this stage to determine whether a muon track is visible in the L1 RoI. Data from the MDTs described in section

3 is added to the L1 information.

After a L2 accept, the full event is finally transferred entirely to the Event Builder (EB), after which the **Event Filter** (EF) selects events based on the complete event data. The full detector granularity, calibration, alignment and conditions of the magnetic field are incorporated in the decision making. The EF consists of algorithms, running on a farm of 1800 processors, each of which handle one event every $1-4$ seconds. The data that pass all these final cuts are stored in different **output streams** at a rate of 300 MB/s. We are mainly concerned with the EF_mu20 stream to select muon events in which more than 20 MeV was deposited.

Output stream	**Requirements**
e10, e20	one electron, $p_T > 10, 20$ GeV
mu10, mu20	one muon, $p_T > 10, 20$ GeV
2e5	two electrons, $p_T > 5$ GeV
2mu4	two muons, $p_T > 4$ GeV
e22i	one isolated electron, $p_T > 22$ GeV
mu20	one isolated muon, $p_T > 20$ GeV
2e12i	two isolated electrons, $p_T > 12$ GeV
2mu10	two isolated muons, $p_T > 10$ GeV

Table 3: Main trigger streams for the selection of W and Z boson final states. The first four are mainly relevant at an LHC beam luminosity of $L \propto 10^{31}$ cm^{-2}s^{-1}. The last four streams become more useful at high luminosities ($L \propto 10^{33}$ cm^{-2}s^{-1}), as **overlapping events** (**pileup**) oblige us to make more stringent isolation cuts.

The L2 trigger and EF together form the **High Level Trigger** (HLT). To ensure the system is able to cope with higher luminosities, one may increase the p_T thresholds or apply for example stronger isolation cuts.

4.5 Data taking performance

For various reasons, not all of the 5182 Tile Calorimeter cells can be used for data taking. Some cells are **masked** after displaying fatal problems or data quality problems. Masking a cell means that it is excluded from offline reconstruction and that it is not considered at the HLT. In figure 11, the number of masked cells is shown as a function of time.

During the technical stop in winter 2010, many read-out channels were restored. Conservatively, cells are only masked until the reason for their malfunction has been investigated and the necessary intervention has been completed.

It is the task of the TileCal **Detector Control System** (DCS) to ensure the detector is safely and coherently operated. The DCS enables several crucial detector systems to be **monitored**, most notably the low and high voltage systems and the cooling for the

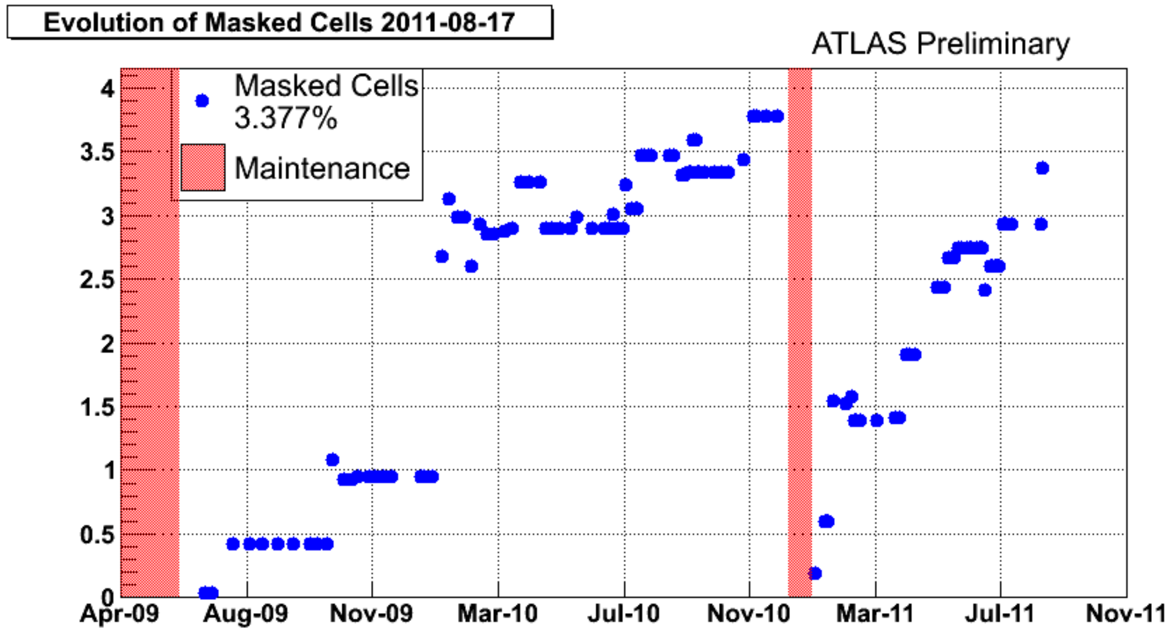

Figure 11: Evolution of cell masking in TileCal. This plot shows the percentage of all cells in the detector that are masked as a function of time, starting from April 2009. The sharp increase in the masked fraction corresponds to losses of entire half of modules. 3.37% of the cells are masked (3% are off) for physics. Ref. [45].

electronics. Although the systems to monitor the TileCal calibration are independent, some information is exchanged with DCS, such that the displayed detector conditions approach the actual status. Moreover, through DCS one has **control** over the cooling. A more detailed description of the DCS implementation is given in Ref. [46]. The detector conditions are stored in a COOL database that is accessed by ATHENA[16] when running a physics analysis.

The performance is often expressed in terms of the overall data taking efficiency, defined by $\frac{L_{\text{recorded}}}{L_{\text{expected}}}$. See figures 12 and 13.

4.6 Fake transverse energy E_T^{fake}

The Tile Calorimeter is not a perfect calorimeter. Limited detector coverage, finite detector resolution, noise and the presence of dead regions have to be considered to ensure that fake transverse energy $E_T^{\text{fake}} \to \epsilon$ is small. In Ref. [24] we find a description of how the

[16]In general, ATHENA is a software framework used in ATLAS, within one can do a physics analysis. For completeness, a reference can be found in Ref. [47].

Inner Tracking Detectors			Calorimeters				Muon Detectors			
Pixel	SCT	TRT	LAr EM	LAr HAD	LAr FWD	Tile	MDT	RPC	CSC	TGC
99.1	99.9	100	90.7	96.6	97.8	100	99.9	99.8	96.2	99.8

Luminosity weighted relative detector uptime and good quality data delivery during 2010 stable beams in pp collisions at $\sqrt{s}$=7 TeV between March 30th and October 31st (in %). The inefficiencies in the LAr calorimeter will partially be recovered in the future.

Figure 12: Data taking performance for all ATLAS subdetectors during 2010. Detector regions that were masked or not participating are not taken into account.

Inner Tracking Detectors			Calorimeters				Muon Detectors				Magnets	
Pixel	SCT	TRT	LAr EM	LAr HAD	LAr FWD	Tile	MDT	RPC	CSC	TGC	Solenoid	Toroid
99.9	99.9	100	90.0	91.3	94.8	98.2	99.5	99.7	99.9	99.6	99.6	99.4

Luminosity weighted relative detector uptime and good quality data delivery during 2011 stable beams in pp collisions at $\sqrt{s}$=7 TeV between March 13th and August 13th (in %). The inefficiencies in the LAr calorimeter will largely be recovered in the future.

Figure 13: Data taking performance for all ATLAS subdetectors during 2011. Detector regions that were masked or not participating are not taken into account.

impact of noise is minimised by building **topological cell clusters** out of the $\Delta\phi \times \Delta\eta = 0.1 \times 0.1$ TileCal cells. These so-called TopoClusters are objects in the (η, ϕ) plane of the calorimeter that are defined by their local hadronic calibration. Ref. [19]. At the level of the entire ATLAS calorimeter, these regions are called **calorimeter towers**. In general, the granularity of the calorimeter is much finer than the trigger tower size. Please refer to Ref. [25] for the cell dimensions in TileCal. For the D-cells, the calorimeter towers are defined as $\Delta\phi \times \Delta\eta = 0.2 \times 0.1$. These clusters have no fixed size, as their shape is the result of running an optimisation algorithm that takes into account cells and their neighbours, see Ref. [26]. Finally we obtain the following total missing energy for electrons and photons, as measured by the calorimeter.

$$E_{x,y}^{\mathrm{e},\gamma,\mathrm{miss}} = E_{x,y}^{\mathrm{Calo,miss}} = - \sum_{\mathrm{TopoCells}} E_{x,y} \tag{10}$$

In the muon channel, a similar expression can be written down, using the track momenta measured by other ATLAS detectors.

$$E_{x,y}^{\mu,\mathrm{miss}} = - \left(\sum_{\mathrm{isolated}} p_{x,y} + \sum_{\mathrm{non-isolated}} p_{x,y} \right) + E_{x,y}^{\mathrm{Calo,miss}} \tag{11}$$

This type of calculation can be done for all physics objects separately. In Ref. [27], it

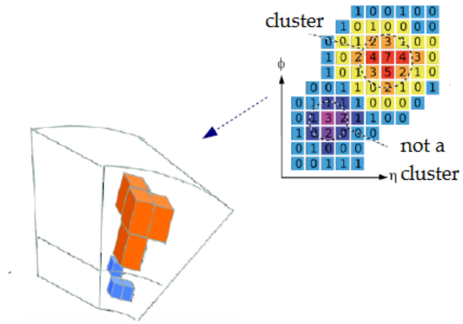

Figure 14: Physics objects measured by the calorimeter are handled as clusters of cells in which energy is deposited. These form three dimensional objects over which all energies are summed to get a handle on the energy, calibrated up to the electromagnetic scale.

is described that topological clusters are formed around cells with $|E_{\text{deposit}}| > 4\sigma_{\text{noise}}$ and $E_{\text{neighbour cells}} > 2\sigma_{\text{noise}}$, greatly reducing the influence of noise in the energy measurement.

5 Calibration

In this chapter, TileCal's calibration systems are described: the cesium system, the charge injection system and the laser system. These systems are required to convert the amplitude of a pulse, as described in section 5.1, to an energy measurement. The conversion formula is given in section 5.2, the calibration systems are described in section 5.3. Dedicated software to monitor the calibration status quo, which was partly developed in the course of this study, is explained in section 5.4.

The term **calibration** signifies the comparison of a measured signal S_{data} with some known signal S_0 with the objective of correcting for the deviation $\frac{S_{\mathrm{data}}-S_0}{S_0}$. As described in Ref. [49], we discern **low-level calibration** and **high-level calibration**, which include converting the ADC counts from the front-end electronics into a physics quantity and applying software corrections in the reconstruction phase, respectively.

5.1 Optimal filtering

Pulses are reconstructed by a so-called **optimal filtering** algorithm, described in Ref. [50]. The algorithm extracts the pulse amplitude A, phase τ and baseline p, which is more often referred to as the pedestal. Let $S(t)$ represent the digital signal determined by the shape form function $g(t)$. Then we can sample the distribution by getting N values at different times t_i.

$$S_i = p + Ag(t_i) \equiv p + Ag_i \tag{12}$$

Let's incorporate the imperfections due to real electronics and perform a Taylor's expansion, as was done in Ref. [51].

$$S_i \approx p + Ag_i - A\tau g_i' + n_i \tag{13}$$

One can now calculate the sought quantities.

$$A = \sum_i^N a_i S_i \tag{14}$$

$$A \cdot \tau = \sum_i^N b_i S_i \tag{15}$$

$$p = \sum_i^N c_i S_i \tag{16}$$

Here, a_i, b_i and c_i are optimal filtering coefficients. A quality factor Q_F is defined to indicate how well the phase and amplitude, or the time and energy respectively, were reconstructed. In case of pileup or saturation, these quality factors may be influenced and can therefore be used to clean the data sample. Although the factor is not actively used in this study, it is defined by equation 17 for completion.

$$Q_F = \sum_{i=1}^{n} \left[S_i - A g_i + A \tau g_i' + p \right] \tag{17}$$

A and p are measured in ADC counts, τ in nanoseconds.

5.2 Calibration of the ATLAS TileCal detector

TileCal makes use of different calibration systems with which one determines the correction factors f needed to obtain the actual measured energy E_i from the signal amplitude A_i. In this section, we describe how this signal reconstruction and calibration is implemented in TileCal.

$$E_i = A_i f_{\mathrm{ADC}\to\mathrm{pC}} f_{\mathrm{pC}\to\mathrm{GeV}} f_{\mathrm{Cs},i} f_{\mathrm{laser}} \tag{18}$$

Fixing $f_{\mathrm{pC}\to\mathrm{GeV}}$, $f_{\mathrm{Cs},i}$ and $f_{\mathrm{laser}} = 1$, one finds that channels have a tendency to drift, as shown in the plot [82]. In other words, we find a time-dependent systematic error $\sigma_{E_i}(t)$ for every channel i. This error $\sigma^2_{E_i}(t) \propto \sum_j \sigma_j^2$ is a convolution of the errors stemming from different sources j. Sources one might consider are the possible changes in the optical part that concerns the transport of scintillation light, the variations in the properties of the PMTs and instabilities in the readout electronics over time. The total received radiation dosage increases over time, introducing a time-dependent degradation of the detector materials. The exposure to secondary particles from proton-proton collisions is different for different parts of the detector, but it roughly affects all the TileCal modules in a similar way as the conditions are symmetric in ϕ. There may be temperature fluctuations that affect the material properties, the electrical conductivity of the wires and the PMT gain. The PMT gain may vary due to temperature fluctuations and high voltage deviations. These effects have been measured to be approximately 1% per 5° C. and 1%/V at 700 V, respectively. Ref. [52, 53].

These sensitivities affect the systematic error on the global energy measurement if not corrected and may even lead to a miscalibration of independent channels. However, instabilities in the light propagation or in the read-out chain as described in section 4 may introduce non-uniformities in the signal response. The three calibration systems that monitor TileCal are designed to find values of f such that $\sigma_{S_i}(t)$ is minimised and the uniformity is preserved [49].

5.3 Calibration systems

The **cesium calibration system** is composed of a hydraulic system and a movable cesium-137 source, which decays isomerically via $^{137}\mathrm{Cs} \to {}^{137}\mathrm{Ba} + \beta^- + \gamma(61\mathrm{keV})$, as described in Ref. [54]. In figure 5, the holes through which the source tube can be transported are pointed out explicitly. The interaction length of the photon is comparable to the thickness of the scintillator tiles, enabling a calibration of the individual tiles. The evolution of the optical response and PMT gains can be monitored over time and can be corrected for if necessary, by fine-tuning the high voltage supplies. The cesium run readout chain is different from the standard readout. A current divider redirects 1% of the PMT output current to a set of slow electronic integrators printed on the 3-in-1 cards. These **integrators** in TileCal are used to construct a voltage signal from a large number of low-energetic light pulses to which the PMTs are exposed during cesium calibration runs. The cesium source radiates off photons at 370 MBq. The integrator sums up the signals over a period of $O(10)$ ms, such that the pulse roughly corresponds to a MeV signal. The integrator system provides 0.5% accuracy in calibrating the response of a single cell [55]. The gain equalisation, that is to say the determination of $f_{\text{Cs},i}$ for each channel i, is done approximately once every month.

As an estimator for the response dE/dx for a module m, we will always use the (truncated at highest 1%) mean value.

$$\left(\frac{dE}{dx}\right)(m) = \frac{1}{N}\sum_{i=1}^{N}\left[\left(\frac{dE}{dx}\right)_i(m)\right] \tag{19}$$

In figure 15, the results are displayed after applying the equalisation procedure with cesium.

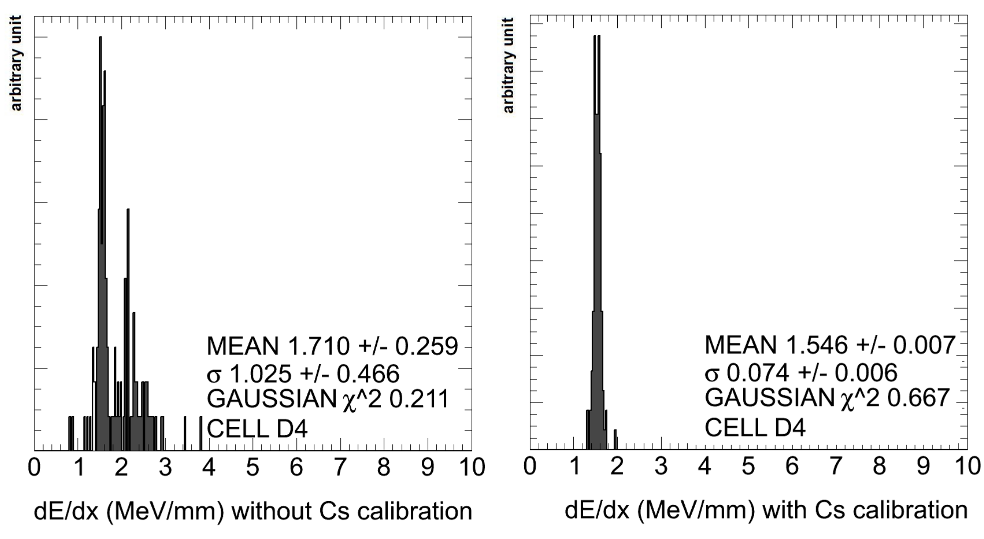

Figure 15: Response equalisation by applying cesium corrections to cell D4 in the ITC region. dE/dx is measured for muons $W \to \mu\nu_\mu$ from collisions over the periods 2010 (B-I) and 2011 (B-I). The standard deviation σ is significantly reduced.

The **laser monitoring system** will be used to monitor the short term deviations in the PMT response with respect to the reference value set by the cesium calibration. The 532 nm green light is delivered in pulses with a width of approximately 10 ns and nominal energy of order TeV. However, after passing through an adjustable filter, one lowers the energy by one order of magnitude to 200 GeV to facilitate the low gain channels. The high gain filter even reduces the energy to the GeV range. The light pulses are sent simultaneously to all 9852 PMTs, which allows for a measurement of the response linearity and relative gain variations over their full sensitive ranges by scanning them with different filters. For each PMT, the factor $f_{\text{laser}} = \frac{L}{L_0}$ is measured, where L is the measured response and L_0 the reference value. One requires the laser system to be **uniform** in the sense that the laser light is distributed to all channels equally. This is done by using diffusers that scatter the light such that it looses its spatial coherence. Moreover, the light intensity should be extraordinarily **stable**. A system of intercalibrated photodiodes is in place to monitor the laser stability. These photodiodes are exposed to a ^{241}Am alpha source approximately once a week. The diode stability is measured to be less than 0.20%. The ratio $R_{i,j} = \frac{S_{\text{channel},i}}{S_{\text{diode},j}}$ for the signal $S_{\text{channel},i}$ from channel i and the signal $S_{\text{diode},j}$ from diode j is required to show deviations less than 1%. The relative gain variation for some channel i monitored by diode j at time t away from the reference run is defined by $\Delta_{i,j} = R_{i,j}(t)/R_{i,j}(0) - 1$. The correction factors that need to be applied at the level of the channels is obtained by evaluating $f_{\text{laser},i} = \frac{1}{1+\Delta_{i,j}}$. See Ref. [49] for an elaborate description of the laser system performance. The experimental setup of the laser system is described in Ref. [56]. In the current predicament, however, there have been unresolved difficulties in using the laser system to correct for any deviations. Optical crosstalk between adjacent photodiodes and electronic crosstalk between photodiodes refute the validity of the laser method. During the long shutdown in 2013, a new laser will be installed to replace the current one.

Finally, a miscalibration of the readout electronics may introduce additional systematic uncertainty into TileCal's energy measurements. The **charge injection system** (CIS) is responsible for reducing this uncertainty by calibrating the readout electronics, which include 10-bit analog to digital converters (ADC) to digitise the analog signals, rendering the data processable further up the chain. To this end, a well-known charge is injected to simulate a physics signal. The initial design can be found in Ref. [57] and its performance is elaborated upon in Ref. [58]. The factor $f_{\text{ADC}\to\text{pC}}$ is measured for each ADC in units of pC.

It seems natural to mention here that the detector-wide factor $f_{\text{pC}\to\text{GeV}} = 1.05$ has been measured in the test beam setup, using a clean sample of electrons with a well-known momentum in the first radial layer. The factor is globally applied, corrected for any radial dependencies. Moreover, the cesium factors are defined with respect to $f_{\text{Cs},i} \equiv 1$ at the moment $f_{\text{pC}\to\text{GeV}}$ was measured in June 2009. The cesium calibration system compensates for changes that occurred since that time. See Ref. [59] for an industrious article on the first TileCal results using test beam data.

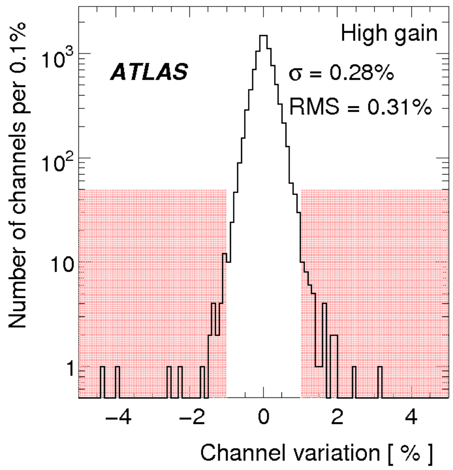

Figure 16: Gain variation of TileCal PMTs over a period of 50 days with respect to a run recorded in september 2010. PMTs are flagged bad when their gain variation exceeds the 1% limit. In this period, 0.14% of the total number of PMTs included in this analysis was considered bad.

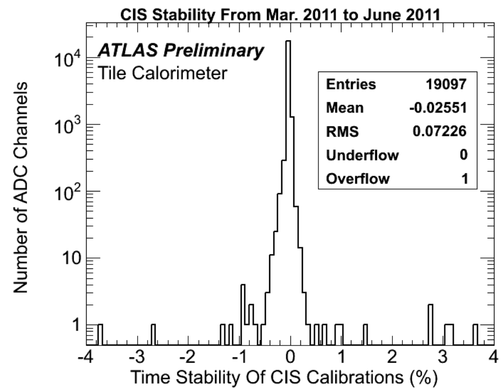

Figure 17: Charge injection stability over a period of three months between March and June 2011. Each entry corresponds to an individual ADC channel. Correction factors are applied for channels with a variation larger than 1%. Both high-gain and low-gain readout signals are shown here. This concerns a fraction of 0.1% of the ADC channels.

Naturally, some degree of cross calibration is needed in order to check for any effects that may be further down the readout chain. A PMT that shows some large gain variation ΔG should provoke some correction by the laser system and the Cs system consequentially. The gain G as a function of the applied voltage V is given by $G(V) = \alpha V^{\beta}$. The time stability of the parameters α and β have been monitored and studied during use and even before installing the PMTs. One influences the gain by choosing a different voltage, as $\frac{\Delta G}{G} \approx \beta \frac{\Delta V}{V}$.

Currently, the cesium and charge injection systems are used for calibration and monitoring purposes.

5.4 TUCS

A Python framework called **TileCal Unified Calibration Software (TUCS)** has been developed to enable sharing functionalities that are useful in the studies of all calibration systems, like plotting calibration constants and reading from and writing to databases. The TUCS framework provides us with a human readable script to analyse the calibration data. Moreover, one would like to have the possibility to make comparisons between the data from different calibration systems. In the scripting language Python, one creates modules that call upon worker classes to do some specific task.

The information handled by TUCS is stored in different parts of the **detector tree**, defined by the **region** class. This class makes use of the structure that we find in the TileCal detector. There are **two tree representations**, one tree related to the readout electronics chain, with 4(barrels)$\times$64(modules)$\times$48(channels)$\times$2(gains) = 12288 tree leafs, and one tree associated to the physical geometry that is organised in cells and towers, with the latter two branches replaced by 5(cell layers) $\times$ $N_{\text{towers in layer}}$. The software handles the specifics of each event by storing them into lists of **event** data members. Each region object carries an **event list**.

To this end, a rudimentary **event** class is defined that contains the **run type**[17], **run number**[18] of the run to which this event belongs, the time at which the event was recorded and the event data. For practical purposes, basic functionality is added to convert a time string into Unix time[19].

A **generic worker** class then defines the layout of user-generated workers. This layout consists of a part called ProcessStart, where the values of data members are set that are not region dependent. In a second part called ProcessRegion, one explicitly defines what actions should be taken on the level of each region. Generally, one accesses the data and specifies in what way the event lists are handled and in which possible data members information is altered or stored. At the end, ProcessStop is the place to store the data in the final format. However, it should be pointed out that programming a TUCS worker can be done in many different ways, depending on the functionalities of the worker. It is common practice to try to follow a structure that is the most efficient in terms of memory usage and that contains the least number of necessary nested loops.

With an instance of the **Go** class, one loops over the workers list that needs to be processed.

A core worker is the **Use** class, which is responsible for retrieving all the calibration run numbers within a user-specified time interval. In the course of this study, additional functionality was added that now includes the possibility to specify the start and end dates. More importantly, in the light of a comparative analysis, one is now able to obtain lists of run numbers for different run types in parallel. Some indispensable workers are in place to read the ROOT[20] Ntuples that contain the calibration data, like **ReadLaser**, **ReadCIS** and **ReadCsFile**. These calibration ROOT Ntuples are stored in a common **tilecali** AFS account, together with relevant SQL databases, macros and shell scripts.

Figures 18 and 19 how the time stability of the laser and charge injection systems, respectively. These plots were generated using the TUCS workers Use, ReadLaser/ReadCIS

[17]Type here being the type of calibration run: Cs, laser or CIS.

[18]Sub-detector cesiumcalibration runs are numbered differently than the ATLAS-wide physics runs.

[19]**Unix time** is a scalar time defined in seconds. The standards are fixed by so-called **POSIX conventions** to convert the human clock-value `YYYY-MM-DD hh:mm:ss.sss` to a mere number. See Ref. [60].

[20]Throughout this study, knowledge of ROOT has been essential as it is used as the framework for almost all physics analyses. Extensive resources are available online, as in Ref. [61].

and ReadDB consequentially to retrieve measured constants. Some additional workers compute the variations at fiber level and the globally corrected PMT shifts. An analysis worker performs the analysis and stores the plots on file. Dedicated TUCS analysis workers have been developed for each calibration system. do_summary_plot and do_pmts_plot are often used to monitor the laser system. In the course of this study, another worker called calibration_overview_tool has been developed to retrieve the Ntuple information from different calibration systems and combine them in a single plot.

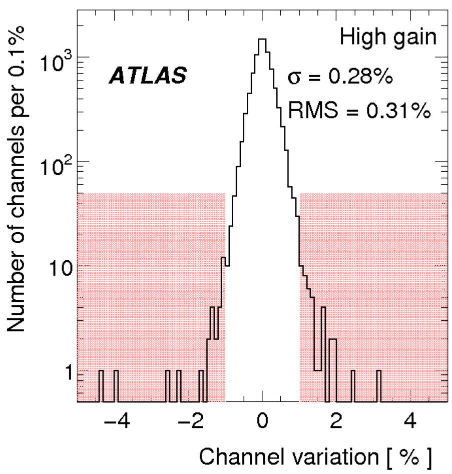

Figure 18: Gain variation of TileCal PMTs over a period of 50 days with respect to a run recorded in september 2010. PMTs are flagged bad when their gain variation exceeds the 1% limit. In this period, 0.14% of the total number of PMTs included in this analysis was considered bad.

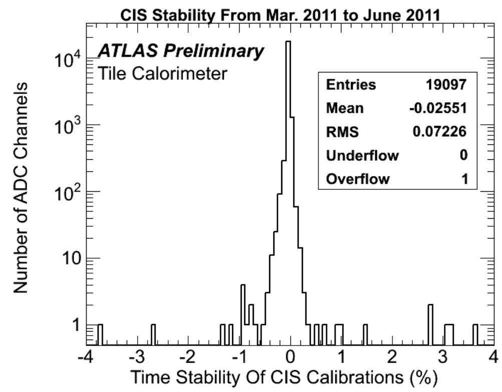

Figure 19: Charge injection stability over a period of three months between March and June 2011. Each entry corresponds to an individual ADC channel. Correction factors are applied for channels with a variation larger than 1%. Both high-gain and low-gain readout signals are shown here. This concerns a fraction of 0.1% of the ADC channels.

Some additional work done in the course of this study to understand the calibration systems is summarised in appendix D.

6 TileCal response using isolated muons from collisions

This chapter describes the method that we have used to determine which TileCal modules were miscalibrated. From this method, we may calculate the proper calibration constant to correct for any miscalibration.

Let us define the **response** of a particular cell as the amount of energy deposited per unit length, $\Delta E/\Delta x$. In a cylindrical detector, this quantity may to first order be expected to be **uniform** in ϕ for every cell type. Provided the cesium scans are applied correctly to equalise the cell responses, described in section 5, we should observe this rotational symmetry by construction.

The cell response for muons depends only logarithmically on E and can therefore be considered an intrinsic property of the material. This allows us to compare cells of different types and draw conclusions about the **intercalibration** of these cells.

6.1 Calibration of the Intermediate Tile Calorimeter in context

The TileCal project dates back to 1992, when it was decided to start the first research and development (R&D) program to support the design and construction of the ATLAS hadronic calorimeter. In 1996, the final design of the modules was proposed. The first electromagnetic (EM) scale $\frac{E_{\text{beam}}}{E_{\text{pC}}}$ was set with the studies performed with data from the (electron) test beams. Between 1999 and 2004, numerous data-taking periods took place with the primary goal to set the EM scale. At the same time, the high voltages were tuned to achieve a cell-by-cell equalisation. The calibration systems, following the description given in section 5, were then used to correct the high voltages. See the article (and its references) in Ref. [62] for a more elaborate historic perspective.

In recent years, **cosmic muons** were used to study and validate the early calibrations, as they serve as a background for the proton-proton events. [20, 40, 63] This background is not uniform in (η, ϕ), as the presence of a huge physical body, the Earth, affects the measurement asymmetrically. Dedicated studies have been performed to understand this effect. Ref. [16]. As the tiles are placed vertically, these muons were only considered well-constructed if their angles with respect to vertical were $\theta > 0.13$. Moreover, only cells downstream with respect to the inner tracker were used in these analyses, to obtain a better momentum resolution. We will use the cosmics results and previous studies with collision muons to validate our method using collision.

The Intermediate Tile Calorimeter increases the particle reconstruction efficiency in the gap/crack region and optimises the response uniformity to hadrons and jets that cross the gap. Particles that loose a substantial amount of energy in the gap may not be reconstructed properly and can be vetoed based on the gap/crack scintillator responses. See Ref. [64]. An issue here is that the scintillators are read-out by only one PMT, whereas the other TileCal cells always have a double read-out. The response of tiles with only a single read-out is not uniform. Therefore, additional noisy contributors to the signal due to PMT, optics or other uniformities cannot independently be corrected for by the cesium system. It is crucial for rare events, like high p_T jets, that these cells are optimally calibrated.

6.2 Event selection $W \to \mu\nu_\mu$

In this thesis, muons from W decay are used. The history of W and Z bosons now extends over a period of almost thirty years since these gauge bosons were discovered in the days of the SPS, in 1983. The experiments that discovered them were called UA1 and UA2. [34] Since then, the intrinsic properties have been measured extensively.

The production rate of the electroweak $W^\pm$ and Z bosons in ATLAS has been studied for various theoretical and experimental reasons. One would like to use the measured cross sections σ_W and σ_Z as a first check that the results from QCD measurements agree with what has been calculated[21] for the new energy range opened up by the LHC. Indeed, $W \to l\mu_l$ and $Z \to ll$ will also function as dominating background in other analyses. [22]

From a instrumentalist point of view, the $W \to \mu\nu_\mu$ signal is a very clean signal that can be used to increase and optimize the understanding of our detectors, as there exist quantitative cuts to eliminate the influence of background muons as much as possible.

The massless neutrinos are not detected and cause transverse energy to seep out silently. One may try to measure this E_T^{miss} by evoking the law of energy conservation, taking into account that there are other effects that may contribute to the missing energy. A large value may be a sign of neutrinos or a beyond the Standard Model physics event.

One has to take into account the existence of background processes that may also contribute to any selected sample of W decay muons. A large sample of low-energetic muons may originate from pion decay. Experimentally these effects are taken into consideration by carefully selecting the events from the muon sample. One usually specifies some set of cuts to clean the muon sample, tabulated in table 4.

A $W \to \mu\nu_\mu$ candidate was recorded on 16 May 2010, with $p_T^{\mu^-} = 22$ GeV, $\eta^{\mu^-} = 2.0$, $E_T^{\text{miss}} = 51$ GeV, $M_T = 61$ GeV. By inspecting the event display in figure 21, we clearly

[21] In QCD, physical quantities are often expanded in orders of α_S, the strong coupling constant. Perturbatively, a cross section may be expressed as follows.

$$\sigma = \sum_i A_i \alpha_s^i \tag{20}$$

Here, the constants A_i are found by calculating the **Feynman diagrams** belonging to all the processes that may occur in order i. Resummation techniques are often considered to solve the many divergences that show up in calculating the quantum field theory path integrals. These techniques should be studied and validated for any new experimental energy range.

[22] The Standard Model (e.g. $qq \to WW$) background is in fact huge compared to new physics signals (e.g. $H \to WW$), as can be concluded from their relative cross sections. A "five sigma" **discovery** requires an excellent understanding of all backgrounds present. See Ref. [35] for a more detailed description on the statistical methods used in ATLAS. In a nutshell, one may think of using the **frequentist** and the **Bayesian** approaches to test the background H_b and "signal plus background" H_{s+b} hypotheses. Both methods should be made to agree, or the disagreement should be understood.

see three jets that we distinguish using the $R = 0.4$ anti-k_T algorithm. All three jets have $E_T > 40$ GeV.

Finally we introduce a cut F in the dE/dx distributions. F is the level of truncation that we use to cut out the tails of the dE/dx distributions, expressed as a percentage of the total integral $\int d(dE/dx)$. We cut all events with a response higher than $(dE/dx)_{\text{cut}}$.

$$\frac{\int_0^{(dE/dx)_{\text{cut}}} d(dE/dx)}{\int_0^{\infty} d(dE/dx)} = F \tag{21}$$

This cut is applied to select only signals from ionisation.

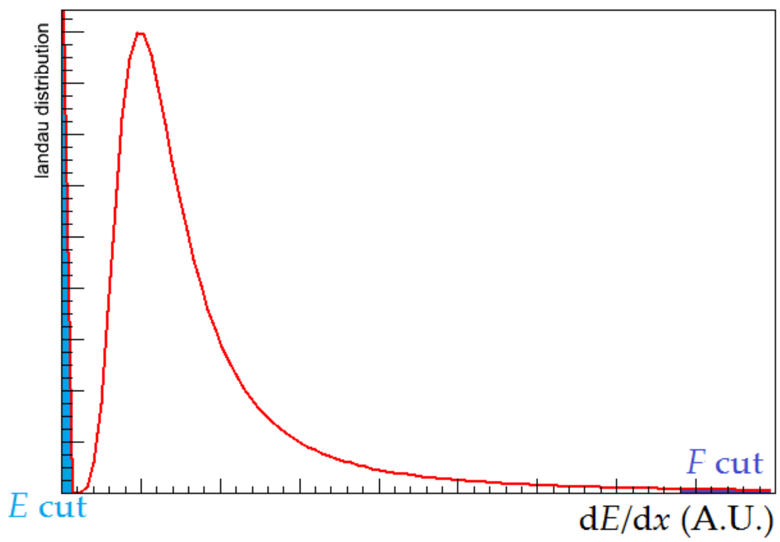

Figure 20: Landau distributed response dE/dx with a noise peak at zero is cut, using E for noise reduction and F to counter higher order ionisation effects that are not well-described in the Monte Carlo, which only occur in the tail of the distribution.

requirement	$W \to e\nu_e$	$W \to \mu\nu_\mu$	$Z \to ee$	$Z \to \mu\mu$
reconstructed lepton	$p_T > 20$ GeV, $\lvert\eta\rvert < 2.5$			
isolation	$E_T^{\text{cone}}/E_T < 0.2$	N/A	$E_T^{\text{cone}}/E_T < 0.2$	N/A
missing energy	$E_T^{\text{miss}} > 20$ GeV	N/A	$E_T^{\text{miss}} > 20$ GeV	N/A
crack region	remove $1.3 < \lvert\eta\rvert < 1.6$	N/A	remove $1.3 < \lvert\eta\rvert < 1.6$	N/A
recoil momentum	$p_T < 50$ GeV			

Table 4: Selection criteria for the W and Z decays as given in the note in Ref. [19].

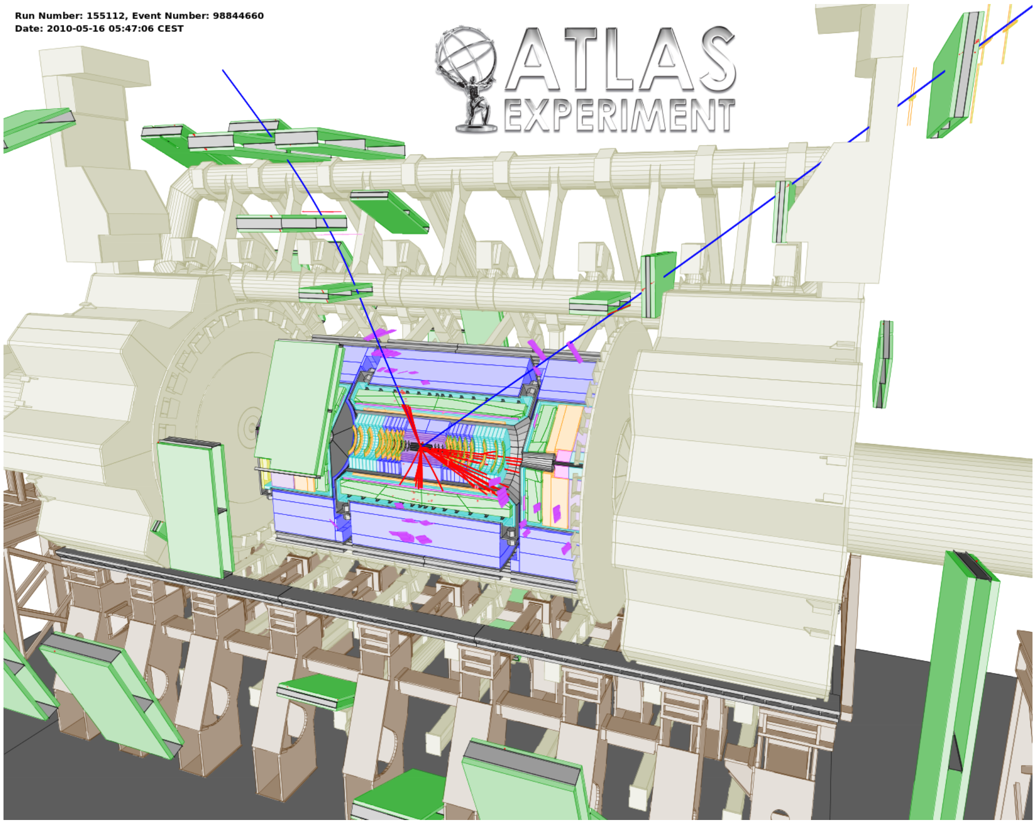

Figure 21: A candidate for $W \to \mu\nu_\mu$ decay, collected on 16 May 2010. Ref. [36].

In this analysis, we select events on the basis of the high level trigger decision. We introduce a dominant cut in the trigger stream, by requiring that event filter mu20 is passed. See table 3 in section 4.4 for the context of this cut. To suppress the presence of background events, we introduce a missing energy cut $E_T^{\text{miss}} > 25$ GeV and use the isolation cuts mentioned in table 4, see figure 22. In addition, one may further clean the sample by imposing that the measured transverse mass of the μ-E_T^{miss} system must be greater than some parameter M_T^{cut}, see figure 23. The mass is defined by equation 22.

$$M_T^W \equiv \sqrt{2p_T^l p_T^{\nu_l}\left(1 - \cos\phi^l - \phi_l^\nu\right)} \tag{22}$$

Cells are selected based on the energy deposited $E_{\text{deposit}} > 30$ MeV and to further remove the noise we require $p_\mu > 40$ GeV.

It should be mentioned here that any cut may introduce systematic uncertainties into the results of the analysis. Errors are fully correlated if they come from the same source. See Ref. [38]. However, this discussion will appear less obvious here, as our main effort goes into quantifying the calibration using ratio $\frac{\text{data}}{\text{simulation}}$ quantities. The systematics introduced

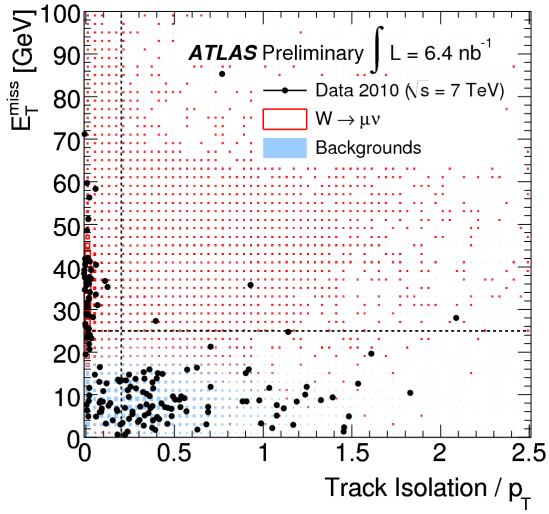

Figure 22: E_T^{miss} versus track isolation parameter.

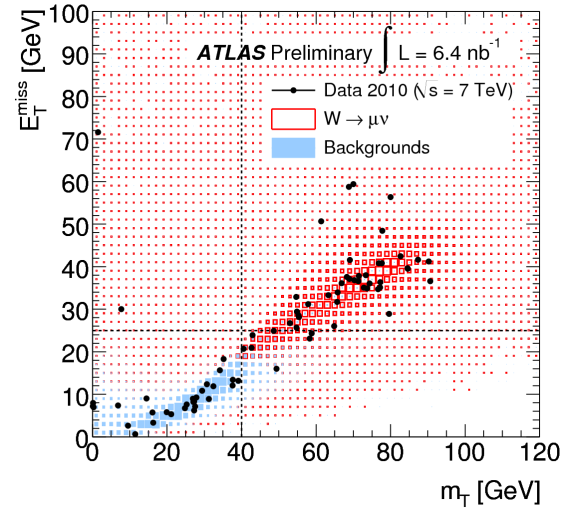

Figure 23: E_T^{miss} versus transverse mass m_T of the μ-E_T^{miss} system. Ref. [37].

by the event selections cancel out, provided we apply the same cuts on data and Monte Carlo and only if our final sample still contains a large enough number of entries.

This type of reasoning is justified if one uses a Monte Carlo that is generated to specifically describe the data. As we are using isolated muons from collisions, this is requirement is fulfilled.

6.3 Collision muons data and Monte Carlo samples

The data is divided into different periods. The periods used in this analysis are tabulated in table 5.

Monte Carlo simulations are used to generate distributions that can also be obtained from the data, in such a way that a comparison between data and simulated events is possible. The experimental conditions, detector geometries and possible physics interactions are modelled correctly if any observable has $\frac{\text{data}}{\text{Monte Carlo}} \approx 1$. These simulations are fine-tuned and validated to secure that the detector is understood.

After applying the cuts, we **reweight** the Monte Carlo to the level of **pile-up**, which is equivalent to the number of proton-proton collisions taking place in the same bunch crossing. This reweighting is done by assigning to every event a weight $w = \frac{g(N_{\text{vertices,data}}=n)}{g(N_{\text{vertices,MC}}=n)}$, where n is the number of interaction vertices in the event, and $g(N_{\text{type}})$ is the normalised probability density function for the number of vertices N_{type} of a certain type (data or Monte Carlo). Simple as it sounds, it requires one to run over the same Monte Carlo sample twice, making it technically convoluted.

period	first run	last run	integrated luminosity recorded by ATLAS (fb^{-1})
2010	152166	167844	$45.0 \cdot 10^{-3}$
2011-D	179710	180481	$17.7 \cdot 10^{-2}$
2011-E	180614	180776	$49.6 \cdot 10^{-3}$
2011-F	182013	182519	$15.0 \cdot 10^{-2}$
2011-G	182726	183462	$55.5 \cdot 10^{-2}$
2011-H	183544	184169	$27.5 \cdot 10^{-2}$
2011-I	185353	186493	$40.0 \cdot 10^{-2}$
2011-J	186516	186755	$23.3 \cdot 10^{-2}$
2011-K	186873	187815	$66.1 \cdot 10^{-2}$
2011-L	188902	190236	$13.3 \cdot 10^{-1}$

Table 5: Data taking periods used in this analysis.

In the course of this study, we used the following Pythia generated Monte Carlo $W \to \mu\nu_\mu$ samples for 2010 and 2011.

mc10_7TeV.106044.PythiaWmunu_no_filter.merge.AOD.e574_s933_s946_r2302_r2300

mc11_7TeV.106044.PythiaWmunu_no_filter.merge.AOD.e815_s1272_s1274_r2730_r2700

Data and Monte Carlo are both converted from the Event Summary Data (ESD) format into Ntuples using an ATHENA package, called **Tile Muon Dumper**, resulting in files with the same variable structure.

6.4 Path length reconstruction Δx

In order to quantify the response, we need the deposited energy E and the **path length** Δx of a track t through a particular cell c.

Muon tracks are extrapolated using the ATLAS extrapolator, which is coded to perform the extrapolation procedure discussed in section 3. [65]. There are several ways to parametrise the extrapolated track parameters. One natural discretisation for collision muon tracks through TileCal is to use the radial **cell layers** l. In this terminology, the LB-A cells belong to layer $l = 12$, LB-BC cells to $l = 13$ and LB-D to $l = 14$, in the ITC/gap region we find the layers $l = 15$ for C10, $l = 16$ for D4 and $l = 17$ for the scintillators. The extended barrel layers are 18, 19 and 20.

Depending on the success of matching the track in the inner detector with the one in the muon spectrometer, the ATLAS extrapolator tool may provide a number $N > 1$ of track parameters for each layer. Let x_n^l denote the nth track parameter in layer l. We can use this information to calculate the track length through a cell c, provided the cell's position

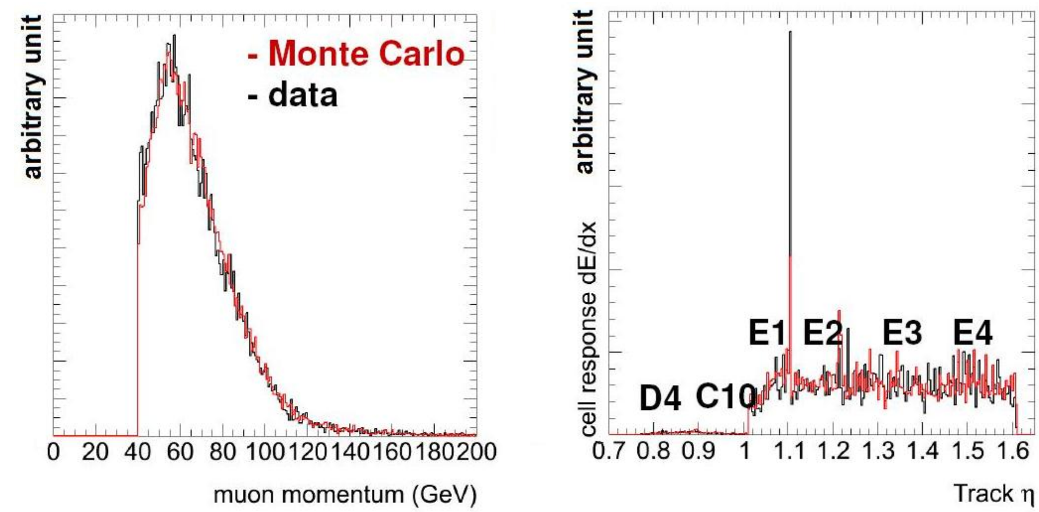

Figure 24: *(left)* Momentum distributions of $W \to \mu\nu_\mu$ muons from collisions, data and Monte Carlo. *(right)* The response of the Intermediate Tile Calorimeter as a function of η, a radiography.

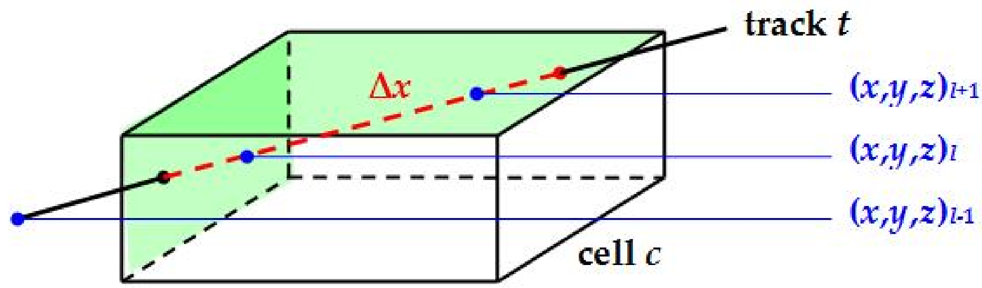

Figure 25: Extrapolated track t over different layers l through cell c. In this schematic overview, $\Delta x \neq 0$. The number of extrapolated parameters that can be obtained per cell layer depends strongly on the success of the track extrapolation. As depicted, there may be

(r_c, ϕ_c, z_c) and dimensions $(\Delta r_c, \Delta\phi_c, \Delta z_c)$ are known. The exact path computation is described in appendix A.

6.5 Double ratio $\frac{dE_{\text{data}}/dx}{dE_{\text{Monte Carlo}}/dx}$

Given a cell type c in a certain data taking period p, we can express the agreement between data and Monte Carlo by defining the **double ratio** $R_{c,p,E,F}$ to quantify the agreement between data and Monte Carlo. E is the lower energy cut in MeV that we use to take out low-energetic noise, as this is not well-described by the simulation. F is the level of truncation, as described in section 6.2.

$$R = \frac{dE_{\text{data}}/dx}{dE_{\text{Monte Carlo}}/dx} \tag{23}$$

The path lengths are constructed at a second level as described in section 6.4, using a ROOT macro. The cuts described in section 6.2 are applied on a third level. E and F cuts are taken to be 60 MeV and 1%, respectively.

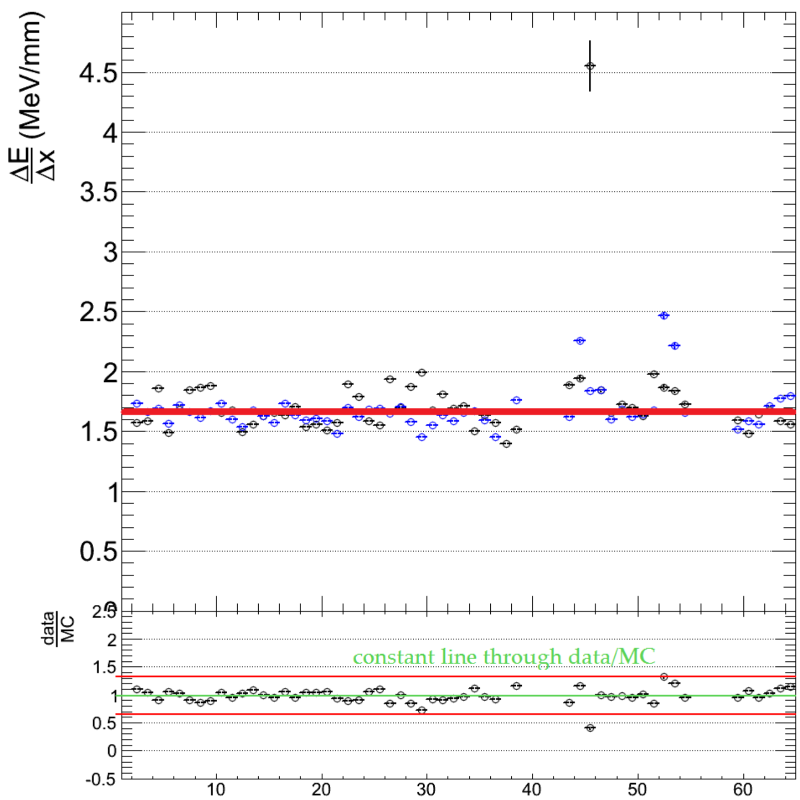

Figure 26: Double ratio R with a constant line fitted through it.

6.6 Constant fit method

This section describes how one may fit a constant line through the double ratio R, as can be seen in figure 26. We will argue that this method is not suitable for our calibration purposes.

The division of two finite, non-zero constants is another constant. For reasons of symmetry, one might assume that the response dE/dx is the same for each module m in either data and Monte Carlo. Under this assumption, the ratio between the two responses, measured and simulated, would therefore also be a constant with respect to the module number.

To test the hypothesis H_0 that the response double ratio $R_{c,p}(m) = \frac{dE_{\text{data},c,p}}{dx} / \frac{dE_{\text{Monte Carlo},c,p}}{dx}$ is constant over all cells c of the same type, in a particular period p, one could naively perform a constant fit.

This is a model in which the expectation value of $R_{c,p,E,F}(m)$ is a constant $\lambda \pm \sigma_\lambda/\sqrt{N}$, where σ_λ denotes the unbiased sample standard deviation and N the sample size. Here, E is the cut in energy in MeV, and F is the level of truncation in the highest values of dE/dx, in percentage. These cuts are applied to reduce the effect of the bad noise description in the Monte Carlo at low energies and to select signals from ionisation only, respectively. To test this hypothesis for a value of $\mu_{c,p,E,F}$, we compute the $\chi^2_{c,p,E,F}$ probability of the **constant fits**[23].

$$R_{c,p,E,F}(m) \equiv \left(\left[\frac{dE}{dx} \right]_{c,p,E,F} \right)_{\text{data}} / \left(\left[\frac{dE}{dx} \right]_{c,p,E,F} \right)_{\text{Monte Carlo}} = \lambda_{c,p,E,F} \tag{24}$$

The fit takes into account the module dependent statistical error on the ratio. Let X, Y be two stochastic variables with standard deviations σ_X, σ_Y and let $Z = X/Y$ be the ratio variable. From error propagation, we know that $\sigma_z^2 = (dz/dx)^2 \sigma_x^2 + (dz/dy)^2 \sigma_y^2 = \sigma_x^2/y^2 + x^2/y^4 \sigma_y^2$. This expression can be simplified to $\sigma_z/z = \sqrt{\sigma_x^2/x^2 + \sigma_y^2/y^2}$, after some algebra.

$$\sigma_R^2 = \left(\frac{\sigma^2_{\text{data}}}{(dE/dx)^2_{\text{data}}} + \frac{\sigma^2_{\text{MC}}}{(dE/dx)^2_{\text{MC}}} \right) R^2 \tag{25}$$

At this stage, $\lambda_{c,p,E,F}$ is the fit parameter and its standard deviation $\sigma_{\lambda_{c,p,E,F}}$ is calculated after performing the fit. $N_{c,p,E,F}$ denotes the number of sampled events in module m.

Why the constant fit method does not work

Even though dE/dx is **Landau distributed**, we are using the direct mean values in an effort to simplify the analysis. Large unphysical fluctuations generated by the Monte Carlo are not taken into account, as the distributions are truncated at the highest $F = 1\%$ values. The mean can no longer diverge.

[23] The method of **least squares** (LSQ) fitting dictates here that if $y = a$ is a (constant) line that describes the data $y_1, \ldots, y_N$, we obtain the best fit parameter a by minimising the sum of the squares $\sum_{i=1}^{N} (y_i - a)^2$. In this simple case, one quickly finds $a = \frac{1}{N} \sum_{i=1}^{N} y_i$ and $\sigma_a^2 = \frac{1}{N} \sum_{i=1}^{N} y_i^2 - \frac{1}{N^2} \left(\sum_{i=1}^{N} y_i \right)^2$. a is just the **sample mean**. See [81].

$$\left(\frac{dE}{dx}\right)(m) = \frac{1}{N}\sum_{i=1}^{N}\left[\left(\frac{dE}{dx}\right)_i(m)\right] \quad (F = 1\%) \tag{26}$$

Using the constant fit method with these estimations, one finds the ratios $1.01 \pm \frac{0.01}{\sqrt{128}}$ for C10, $1.00 \pm \frac{0.01}{\sqrt{128}}$ for D4, $0.93 \pm \frac{0.09}{\sqrt{128}}$ for E1, $0.94 \pm \frac{0.06}{\sqrt{128}}$ for E2, $1.07 \pm \frac{0.06}{\sqrt{128}}$ for E3 and $0.94 \pm \frac{0.08}{\sqrt{128}}$ for E4, respectively. The factor $1/\sqrt{128}$ comes in by taking the data from the two sides (2×64 modules) of the detector together. This simplifies the analysis.

Before interpreting these results, one should ask whether they have any meaning at all. One needs a measure to establish the **goodness of fit**. The quantity $P(n, \chi^2_{c,p,E,F})$ denotes the probability that the observed $\chi^2_{\text{observed},c,p,E,F}$ exceeds the value $\chi^2_{c,p,E,F}$ by chance, given a number of degrees of freedom n, even for a correct model. In short, a higher value of P means a better description of the observable by the model.

When performing the fits in ROOT, one can exploit the built-in hypothesis testing functionality to calculate the χ^2 probabilities. In the case of a constant fit, one merely has one degree of freedom: the parameter that determines the value of the constant. Choosing $E = 60$ MeV and $F = 1\%$, we find that $P(n, \chi^2_{c,p,60,1})$ vanishes, even if we vary E by ± 30 MeV or F by $\pm 1\%$. That is, the χ^2 probabilities turn out to be smaller than 0.001.

We find that this model does not describe the double ratio well. The module-by-module fluctuations are larger than the statistical errors. This implies that we cannot properly interpret the meaning of the fit parameter. For the purposes of a calibration study, another estimator for the double ratio is needed. One can then define some significance level that is used to distinguish statistical fluctuations in the double ratio from real deviations. Modules that deviate too much are called miscalibrated. By excluding these modules from the analysis, one is able to check the intercalibrations between cells of different types c. Also, one can monitor the evolution over time p.

In short, we need some other model that does not use the constant fit described here.

6.7 Gaussian fit method for cell calibration

Let us now develop a method to study the uniformity, calibration and intercalibration of the cells in the gap/crack region. We compute the double ratio $R_{c,p,E,F}$ for each module m separately. In section 6.6, it is shown that a simple constant fit through the $(R_{c,p,E,F}, m)$ histogram has no meaning. One suspects some unaccounted systematic effect needs to be taken into consideration. The truncated means of the module-by-module dE/dx responses seem to be Gaussian distributed, as can be seen in figure 27.

If we assume that the (truncated mean) energy depositions in data and Monte Carlo are both Gaussian distributed, the ratio distribution becomes very complicated. Let us pause here to understand the concept of a **ratio distribution**.

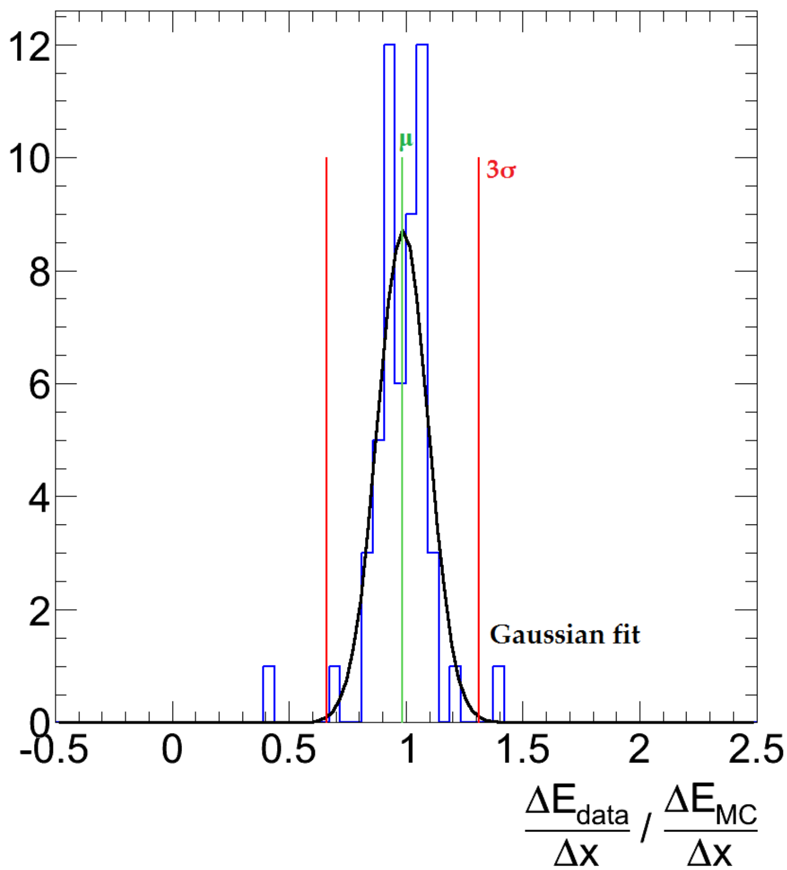

Figure 27: Double ratio R with a Gaussian fitted through it. The distribution mean μ and three-standard deviations σ are shown.

Intermezzo: ratio distribution of two Gaussian distributed variables

Let X and Y be independent stochastic variables and let $R = X/Y$ denote the ratio of the two. In general, the ratio distribution $P_R(R = r)$ can be computed as follows.

$$P_R(r) = \int_{-\infty}^{\infty} |y| P_{X,Y}(ry, y) dy \tag{27}$$

Here, $P_{X,Y}(x, y)$ denotes the joint probability density function of X and Y. In principle, we can do the integral if we know how X and Y are distributed. Let X and Y be independent Gaussian distributed stochastic variables with mean values μ_x and μ_y and standard deviations σ_x and σ_y.

$$P_R(r) = \frac{b(r)c(r)}{a^3(r)}\frac{1}{\sqrt{2\pi}\sigma_x\sigma_y}\left(2\Phi\frac{b(r)}{a(r)}-1\right)+\frac{1}{a^2(r)\pi\sigma_x\sigma_y}\exp\left[-\frac{1}{2}\left(\frac{\mu_x^2}{\sigma_x^2}+\frac{\mu_y^2}{\sigma_y^2}\right)\right] \quad (28)$$

We define the following auxiliary functions.

$$a(r) = \sqrt{\frac{r^2}{\sigma_x^2}+\frac{1}{\sigma_y^2}} \quad (29)$$

$$b(r) = \frac{\mu_x}{\sigma_x^2}r+\frac{\mu_y}{\sigma_y^2} \quad (30)$$

$$c(r) = \exp\left[\frac{b^2(r)}{2a^2(r)}-\frac{1}{2}\left(\frac{\mu_x^2}{\sigma_x^2}+\frac{\mu_y^2}{\sigma_y^2}\right)\right] \quad (31)$$

$$\Phi = \int_{-\infty}^{r}\frac{1}{\sqrt{2\pi}}\exp\left(-\frac{1}{2}u^2\right)du \quad (32)$$

One can argue that the ratio distribution of equation 28 will itself be **approximately Gaussian** if the standard deviation in the numerator variable X is much larger than the standard deviation of the denominator quantity Y, whilst maintaining approximately the same central values for both X and Y.

Double ratio distribution approached by a Gaussian

In our case, these **requirements** can be cast in the following mathematical form.

$$\mu_{dE/dx,\mathrm{data}} \approx \mu_{dE/dx,\mathrm{MC}} \quad (33)$$

The first requirement is fulfilled. The mean values of the response are quite the same, as the ratios are approximately 1.

$$\sigma_{dE/dx,\mathrm{data}} > \sigma_{dE/dx,\mathrm{MC}} \quad (34)$$

The second requirement may be fulfilled, but it cannot be said with certainty. The Monte Carlo generator used a simulation of the Tile Calorimeter that is symmetric in ϕ. As the real detector is less symmetric, for example due to the presence of more (or less) detector material at some places, we may find that the response dE/dx is not uniformly distributed over ϕ. This would result in a response distribution for the data with a larger width than the Monte Carlo distribution, fulfilling the second requirement. Another effect is that the size of our Monte Carlo sample is much bigger than the size of the data sample, resulting in bigger statistical errors for the numerator of the double ratio, as defined in equation 24. However, this is of less importance as we know from the constant fit considerations that the standard deviation of the ratio distribution is dominated by the systematic deviations, $\sigma \approx \sigma_{\mathrm{syst.}} > \sigma_{\mathrm{stat.}}$.

Nevertheless, we have grounds to **assume** the **double ratio distribution behaves like a Gaussian**. We allow for small deviations by modelling the double ratio by a Gaussian distribution with a central value $\mu_{c,p,E,F}$ and a standard deviation $\sigma_{c,p,E,F}$. We will test whether the double ratio distribution really behaves like a Gaussian, using once again the χ^2 as our test statistic.

$$H_0 : P(R_{c,p,E,F}(m)) \propto \exp\left[-\frac{1}{2}\left(\frac{R_{c,p,E,F}(m) - \mu_{c,p,E,F}}{\sigma_{c,p,E,F}}\right)^2\right] \tag{35}$$

The estimator for the double ratio is obtained as the central value of the Gaussian fit. Provided all cells of the same type c are calibrated correctly, which is not at all clear at this stage, and provided they are well-described by the Monte Carlo, one expects to see $\mu_{c,p,E,F} \approx 1$. In this study, the energy cut E is taken to be 60 MeV and the truncation level F is set at 1% in an effort to improve the agreement between data and Monte Carlo.

Miscalibration and calibration factor

The standard deviation is the fit parameter in which we absorb the statistical and systematic deviations, $\sigma = \sigma_{\text{stat.}} \oplus \sigma_{\text{syst.}}$, as there is no apparent way to disentangle these errors at this level. The cesium calibration system handles the cell equalisation. One should find $\sigma_{c,p,E,F} \approx 0$ if this is done properly. At the level of individual modules, we call a module m **miscalibrated** if $|R_{c,p,E,F}(m) - \mu_{c,p,E,F}| < 3\sigma_{c,p,E,F}$ is not satisfied. At this significance level, the probability to commit the type II error, to identify a miscalibrated module that is actually calibrated properly, is 0.27%. In figure 28, the double ratios are shown for all cells E2-A. The distribution is Gaussian.

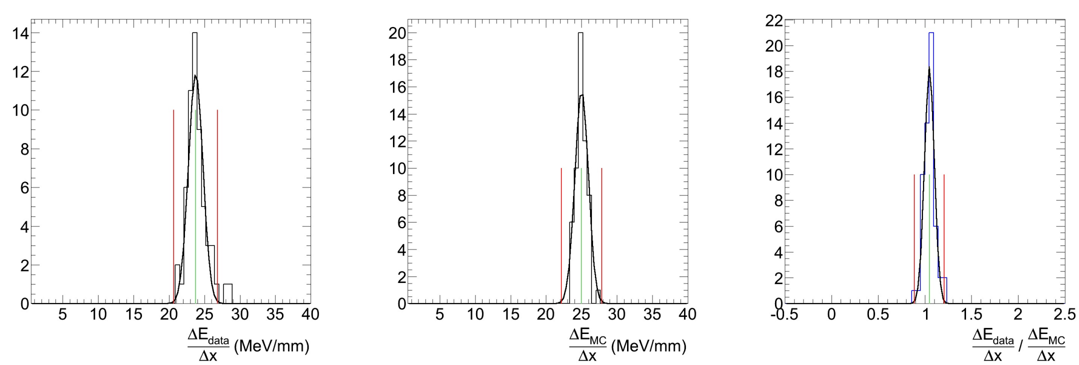

Figure 28: Double ratio distribution for all the cells E2, A-side. The mean value μ_R (green) and the $3\sigma_R$ level (red) are displayed to visualise how miscalibrations are found.

The **calibration constant CalFactor**(m) for an individual module then becomes the following ratio.

$$\text{CalFactor}(m) = \frac{\mu}{R(m)} \oplus \Delta\text{CalFactor(statistical)} \oplus \Delta\text{CalFactor}(E) \oplus \Delta\text{CalFactor}(F) \qquad (36)$$

We will consider the gap/crack cells, summarised in appendix B, table 12, as different types of cells.

6.8 Intercalibration for cells of different type

Intercalibration is the effort to equalise the response of cells of different types. The logic is as follows. One takes out the miscalibrated modules based on the criterium stated by the Gaussian fit method. After, one reapplies the method to calculate the central values.

Checking the intercalibration is a check of the success of the cesium calibration. Assuming the cesium constants have been applied correctly, one can use the intercalibration between layers to check if the method is consistent with earlier results.

6.9 Method validation by layer intercalibration

Unless the experimental conditions changed dramatically, the results obtained by the method described here should not be too different from the results obtained in earlier studies. The response dE/dx can largely be considered as a material property. Therefore, even though the analysis done with cosmic muons involved cuts that we do not (or cannot) use here, namely $N_{\text{tracks}} = 1$, $\Delta x > 200$ mm and a different momentum range, we should still see resemblance with the results from collisions.

Let us apply the Gaussian fit method to cells $c \in l$ that belong to some layer l. The results are tabulated in table 6.

cell	$\mu_{c,p,E,F}$	$\sigma_{c,p,E,F}/\sqrt{N}$	$\sigma(E)$	$\sigma(F)$
LB-A	0.99202	± 0.00014	$^{+0.00441}_{-0.00783}$	$^{-0.00261}_{+0.00199}$
LB-BC	1.00031	± 0.00013	$^{+0.00306}_{+0.00003}$	$^{-0.00141}_{+0.00323}$
LB-D	1.01397	± 0.00017	$^{+0.00118}_{-0.00143}$	$^{+0.00188}_{-0.01463}$
EB-A	0.99971	± 0.00282	$^{+0.00405}_{-0.00891}$	$^{-0.00177}_{-0.00167}$
EB-BC	0.99128	± 0.00009	$^{+0.00143}_{-0.00038}$	$^{-0.00156}_{-0.00167}$
EB-D	1.00026	± 0.00011	$^{+0.00139}_{-0.00032}$	$^{-0.00191}_{+0.00067}$

Table 6: Intercalibration of TileCal layers. Central values $\mu_{c,p,E,F}$ were obtained using the Gaussian fit method on the double ratio $R_{c,p,E,F}(m)$ distributions. The statistical error is denoted by $\sigma_{c,p,60,1}/\sqrt{N}$ and the systematic errors introduced by truncating and cutting in energy are given by ${}^{+\Delta_{E=90}}_{-\Delta_{E=30}}(E)^{+\Delta_{F=2}}_{+\Delta_{F=0}}(F)$. Miscalibrated cells have been taken out.

Please note the statistical and systematic errors are quite small and the central values are approximately 1. The bulk of the events lies within the parameter space that is well described by the Monte Carlo, after reweighting has been applied. Moreover, the number of events considered is quite large, $O(10^6)$.

As discussed in Ref. [63], similar results can be obtained using cosmics. They are tabulated in 7.

layer	R^l (2008)	R^l (2009)	R^l (2010)
LB-A	0.966 ± 0.012	0.972 ± 0.015	0.971 ± 0.011
LB-BC	0.976 ± 0.015	0.981 ± 0.019	0.981 ± 0.015
LB-D	1.005 ± 0.014	1.013 ± 0.014	1.010 ± 0.013
EB-A	0.964 ± 0.043	0.965 ± 0.032	0.996 ± 0.037
EB-BC	0.977 ± 0.018	0.966 ± 0.016	0.988 ± 0.014
EB-D	0.986 ± 0.012	0.975 ± 0.012	0.982 ± 0.014

Table 7: Results from cosmics. The double ratios data/MC are displayed with their statistical errors for the different periods that were taken into account. This table was taken from Ref. [63].

In another study, see Ref. [66], a table was produced for collision muons, using a constant line fit, different cuts and not taking into account the Intermediate Tile Calorimeter. The results are tabulated in 8.

cell	2010	2011-D	2011-E	2011-F	2011-G	2011-H
LB-A	0.960 ± 0.003	0.966 ± 0.002	0.952 ± 0.003	0.962 ± 0.002	0.959 ± 0.001	0.959 ± 0.002
LB-BC	0.975 ± 0.002	0.975 ± 0.001	0.977 ± 0.002	0.975 ± 0.002	0.975 ± 0.001	0.973 ± 0.001
LB-D	1.010 ± 0.003	1.005 ± 0.002	1.001 ± 0.003	1.003 ± 0.002	1.006 ± 0.001	1.004 ± 0.002
EB-A	0.958 ± 0.004	0.969 ± 0.002	0.967 ± 0.004	0.965 ± 0.003	0.967 ± 0.001	0.970 ± 0.002
EB-BC	0.976 ± 0.003	0.973 ± 0.002	0.966 ± 0.003	0.972 ± 0.002	0.973 ± 0.001	0.966 ± 0.002
EB-D	0.976 ± 0.003	0.976 ± 0.002	0.986 ± 0.004	0.977 ± 0.002	0.978 ± 0.001	0.975 ± 0.002

Table 8: Results from collisions, not taking into account the Intermediate Tile Calorimeter. The double ratios data/MC are displayed with their statistical errors for the different periods that were taken into account. This table was taken from Ref. [66].

The results are comparable within a margin of 4%. The argument here is that the double ratios should correspond to 1 in either method, in case of an overall well calibrated detector. Small differences are to be expected, as different cuts are used, but a clear deviation of the double ratios from 1 should be made visible by both methods, provided some global shift has not been corrected for. We see that the different studies agree.

6.10 Maximum likelihood method

It is interesting to approach the topic of intercalibration with a method that takes the module-by-module fluctuations as an extra parameter. We first apply the Gaussian fit method to take out miscalibrated modules. Then we extend the notion that the double ratios are Gaussian distributed, by introducing a **smearing** s that quantifies the module dependent systematics. The following two-parameter **likelihood function** L is fitted to the data using an instance of the ROOT TMinuit class. Let $T = h(X_1, X_2, \cdots, X_n)$ be a random variable. From Ref. [67], we know that the maximum likelihood estimator of θ is the value $t = h(x_1, x_2, \cdots, x_n)$ that maximises the likelihood function $L(\theta)$. T is called the maximum likelihood estimator of θ.

$$L = \prod_{m=1}^{2\times 64} \frac{1}{\sqrt{2\pi(\sigma_m^2 + s^2)}} \exp\left(-\frac{1}{2}\left[\frac{R_m - \mu}{\sigma_m^2 - s^2}\right]\right) \tag{37}$$

One finally obtains some quantifiable handle on the systematics. The central values should not be different from the ones found by the Gaussian fit method. An example of how the smearing s is determined using a likelihood surface is displayed in figure 29.

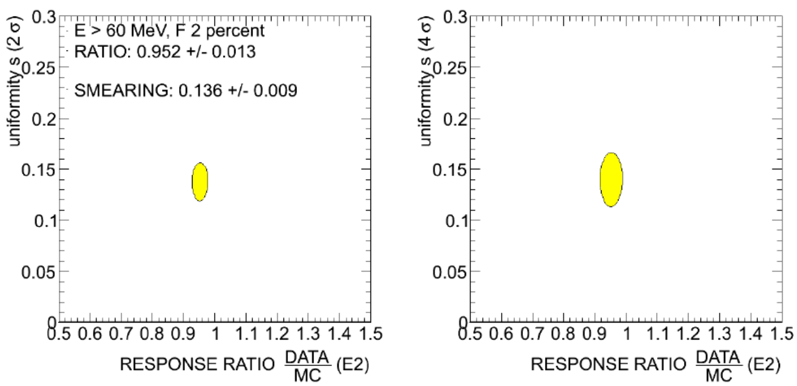

Figure 29: Likelihood surface to determine the smearing s, which quantifies our "ignorance" of the real double ratio distribution, in the sense that it measures how well the Gaussian fit may be performed.

6.11 Chapter summary

Summarising, we will use the double ratio $\frac{\text{data}}{\text{MC}}$ to determine which of TileCal's gap/crack cells are miscalibrated. The term "double ratio" refers to the fact that the responses dE/dx in data and Monte Carlo are already ratios, which are then compared by division. As the double ratio is approximately Gaussian distributed, we will use the Gaussian fit method as described in this chapter. Any cell that deviates more than 3σ from the mean μ will be flagged miscalibrated, and for these we recalculate its calibration factor. This way we equalise the cell responses for cells of the same type.

Cells of different types may be intercalibrated, by applying an overall calibration constant.

7 Effects of miscalibration on jet physics

This chapter provides a motivation for calibrating the Tile Calorimeter. As described in section 2.2, the ATLAS Tile Calorimeter is a hadronic calorimeter, that is optimised to have the best energy resolution for jets. What is the effect of miscalibrated cells to the measured energy of jets?

In section 7.1, jets are discussed in general. Section 7.2 discusses dijet events at the LHC. To study jets, one needs jet algorithms that sum up the energy and momenta at the level of the hadronic calorimeter, as discussed in sections , and . A qualitative conclusion is drawn about jets in section .

7.1 Jets

At detector level, a **jet** is a group of hadrons detected within a certain narrow cone. In event displays, one often considers tracks that seem to travel from the interaction point towards similar directions. Obviously, jets are not fundamental objects of nature, as they are **composite systems of particles**. However, they do obey the laws of conservation of energy and momentum and one can attempt to describe them in terms of their constituents.

Given a jet j consisting of particles $p_1, \cdots, p_N$, one may try to reconstruct which process must have resulted in this particular jet. Here, we see the first indication that there will not be a unique way to associate the final jet state with a particular initial state. After all, the hard scattering process[24], at the interaction point involved quarks and gluons which, governed by the strong force, exchange color charge when they interact, whereas jets are color neutral. See Ref. [68].

Therefore, the collection of jets in a single event may in some ways be thought of as an indirect representation of the event itself. See Ref. [69]. This ambiguity opens up the possibility to develop different methods, often called jet algorithms, to reconstruct jets from physics events.

However, at first glance this does not seem to be logical. One event may contain a high degree of particles, all carrying energy and momentum (E_i, p_i) over a certain track (t_i, x_i). Combining these four-vectors into one jet four-vector seems a decrease the amount of available information. It must be pointed out that a jet finder is an experimentalists tool, which in effect projects the lower energetic particles onto higher energetic objects, obtained by combining separate high energetic particles and summing their momenta. In the simplified picture, a higher energy E comes along with a smaller de Broglie wavelength λde Broglie. Jets are sometimes referred to as parton-like, as they provide a better resolution for studying the (higher energetic) hard scattering process. One can use this narrow stream of momentum to probe the characteristics of the hard scattered matter. By clustering the hadronic final states, one may be able to determine the underlying parton structure. See Ref. [70] for an example of such a clustering method.

[24] $qq \to qq$, $qg \to qg$, etcetera.

7.2 Two jet production at the LHC

Using proton-proton collisions, an event with jets j in the final state will look like $pp \to Nj$, $N > 1$. The latter is dictated by conservation laws. The majority of jet events will consist of two approximately back-to-back jets, as **dijet events** simply have a higher cross section than events with $N > 2$ jets. See Ref. [77]. Various phenomenological models aim to describe jet production in collider experiments. These models are the backbone of Monte Carlo simulations.

One such a model is the **Lund model**, linking the concept of quark confinement to the presence of string shaped color fields. In nature, one often finds baryons of the meson type $q\bar{q}$, which in the context of this model is seen as two end-points of a gluonic string, the quarks, yoyo-ing back and forth under an exerted color force that is considered to be linearly proportional to the distance between the quarks. In the process of simulating jet formation using phenomenological models like the Lund model, one distinguishes several phases in which the matter behaves differently. Close to the interaction point, quark pair production take place governed by the strong force. This process is referred to as **fragmentation**. After the **hadronisation** step, we are left with jets of hadrons.

In a two-body scattering $(1) + (2) \to (3) + (4)$, one generally finds the following expression for the cross section σ in the center-of-mass frame.

$$\frac{d\sigma}{d\Omega} \propto \frac{|M|^2}{(E_1 + E_2)^2} \tag{38}$$

Here, Ω is the solid angle with $d\Omega = \sin\theta d\theta d\phi$, E_i is the energy of particle i and M is the matrix element that describes the amplitude of going from the initial to the final state. See Ref. [78].

In figure 30, the Feynman diagrams are drawn for the lowest order processes that contribute to the production of dijet events.

These processes contribute to the matrix elements squared $|M_{qq}|^2$, $|M_{qq'}|^2$ and $|M_{q''q'''}|^2$, where the subscript denotes the final state. Let us first write down the first two matrix elements.

$$\overline{|M_{qq}|^2} = \left(\frac{4\pi}{2 \cdot 3}\right)^2 [T_{gg} + T_{ZZ} + T_{\gamma\gamma} + T_{gZ} + T_{g\gamma} + T_{Z\gamma}] \tag{39}$$

$$\overline{|M_{qq'}|^2} = \left(\frac{4\pi}{2 \cdot 3}\right)^2 \left[T'_{gg} + T'_{WW} + T'_{ZZ} + T'_{\gamma\gamma} + T'_{gW} + T'_{WZ} + T'_{W\gamma} + T'_{Z\gamma}\right] \tag{40}$$

The bar denotes initial state spin and colour averaging. T_{ij} is the sum of the interference between two particles i and j. The contributions are taken from Ref. [79].

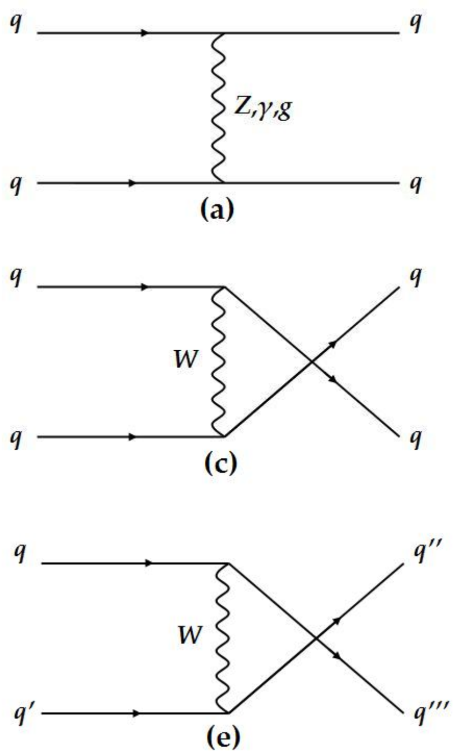

Figure 30: Feynman diagrams for the lowest order processes that contribute to the production of hadronic jets in a proton-proton collider; *(a)* scattering of two identically flavoured quarks with the same charge, *(b)* scattering of two different flavoured quarks with the same charge, *(c)* scattering of two identically flavoured quarks with different charges, *(d)* scattering of two different flavoured quarks with different charges and *(e)* scattering of two different flavoured quarks that result in yet another pair two different flavoured quarks.

7.3 Jet algorithms

A jet defnition is a full set of rules for merging the information from all the separate particles to obtain just a few parton-like jets. One may ask which particles should be put together into a common jet, but also how one should combine their momenta. Sofar, we have not defined yet what a jet is. In fact, each method to reconstruct jets distinguishes itself from other jet algorithms by the jet definition it corresponds to. Different jet definitions result in different types of jets with different properties. However, physical results should not depend on the definition.

This remark translates into the stringent requirement that one would like to have a jet definition that is insensitive to the emission of soft gluons ($E \to 0$) or collinear gluons ($\theta \to 0$), where the probability for a quark to radiate of a gluon is proportional to the following expression.

$$\int \alpha_S \frac{dE}{E} \frac{d\theta}{\theta} \gg 1 \tag{41}$$

Here α_S is the strong coupling constant[25], E the energy of the quark and θ the emission angle.

Defining a jet is tricky. The process of **parton fragmentation** is what causes the high multiplicity of particles to form in the first place and there are many examples of physical quantities that are affected by this process. The multiplicity of gluons is obviously variant under each soft or collinear splitting that takes place. This is an example of an **infrared and collinear unsafe** quantity. The energy of the hardest particle is a second example. See Ref. [71].

As jet algorithms may be iterative in nature, calculating jet axes and energies may scale with the number of involved particles N. Jet finding may be computationally cumbersome and in recent years, much effort has gone into inventing intelligent ways to cope with this.

7.4 Sequential Clustering Algorithms

Naively, one could try to specify a certain radius R upon which one decides whether the particle still belongs to the current jet. More specifically, one could calculate the distances ΔR_{ij} between every two particles i and j in (η,ϕ) space and require them to be smaller than R.

$$\Delta R_{ij}^2 = (\eta_i - \eta_j)^2 + (\phi_i - \phi_j)^2 < R^2 \tag{42}$$

There are several variants of these **sequential clustering algorithms** that are iterative in nature. An important concept here is the particle[26] around which one starts forming such a protojet, called a seed. The k_T algorithm distinguishes so-called **protojets** based

[25] At low energy scales, this α_S approaches 1.

[26] In hadronic calorimetry, we consider the calorimetric towers that reflect upon the detector's granularity.

on a distance proportional to transverse momentum k_T, the anti-k_T algorithm utilises the reciprocal $\frac{1}{k_T}$ and the Cambridge/Aachen (C/A) algorithm does not take into account the momenta and just considers cones in the spacial plane.

The step by step approach is as follows.

1. Find the smallest value for $d_{ij} = \min\left(p_{ti}^{2n}, p_{tj}^{2n}\right) \Delta R_{ij}^2 / R^2$ and $d_{iB} = p_{ti}^{2n}$.
2. If $d_{ij} < d_{iB}$, recombine them using $p^2_{\mathbf{protojet}} = p_{ti}^2 + p_{tj}^2$.
3. If $d_{ij} > d_{iB}$, protojet i is considered a jet and will not be considered anymore.
4. Iterate until only jets are left.

n determines the algorithm variant. It is worth noticing that the anti-k_T algorithm will start forming jets around hard seeds, as higher momenta lead to smaller distances d_{ij}, whereas the k_T algorithm will first start recombining the soft particles. This is interesting in terms of infrared and collinear safety.

n	algorithm	IR safe	collinear safe	clustering time
-1	anti-k_T	safe	safe	N^3
0	C/A	safe	safe	N^3
1	k_T	safe	safe	N^3

Several extensions or variants of these methods exist, such as the usage of flavour dependent distances, or variable parameters R that are given as a function of the transverse momentum, fine-tuned for the studied event type. One distinguishes **exclusive jet algorithms**, which just measure distances between protojets without any parameter R, and **inclusive algorithms** that take into account the cone distance. One may verify the jet reconstruction with smaller angles $R_{\mathbf{redo}} < R$, a procedure called **trimming** [80].

Moreover, it has to be pointed out that the jet clustering time of N^3 is applicable to the brute force method. Many attempts have been made to reduce this time. In [72], the clustering time has been brought down to $N \log N$. The main improvement here lies in the way the protojets are ordered. [73].

7.5 Cone algorithms

Cone algorithms search for stable cones with a certain radius, by checking that the cone axis, which is the line between the cone center and the interaction point, is pointing in the same direction as the total momentum of the particles within the cone.

$$\frac{\sum_i p_{ti}}{|\sum_i p_{ti}|} - \frac{r_{\text{cone}}}{|r_{\text{cone}}|} \approx 0 \tag{43}$$

Cone algorithms work purely geometrical, making the algorithms less dependent on the quality of the particle's energy reconstruction.

In general this may result in multiple overlapping cones, which then have to be resolved using splitting and merging procedures. This approach is inspired on the occurrence splitting and merging in particle detectors, as two particles might end up being detected by the same calorimeter cell. Moreover, when a particle showers, it may distribute its energy over multiple calorimeter towers. As collinear splitting and the presence of soft particles have the potential to shift the jet energy scale or even the final jet states, one often seeks a way to make cone algorithm IRC safe. In other words, one does not want the properties of the detector to effect the physics results.

Historically, cone algorithms have been the most successful algorithms in hadron colliders and there exist many varieties. Ref. [74, 75]. An often employed trick to ensure IRC safety is to scan the entire event hitmap for all stable cones, rendering the jet definition seedless. SISCone is one of the more recent examples of such a seedless, IRC safe, cone algorithm.

In ATLAS, the anti-k_T algorithm with radii 0.4 and 0.6 as well as seeded cone algorithms with radii 0.4 and 0.7 are often used.

7.6 Jets and calibration

Setting the **jet energy scale** (JES) is the action of applying a correction to the measured energy E_{calo} that depends on the coordinates in (p_{jet}, η) space.

First, the background due to pileup is corrected for, taking out the background formed by particles from other vertices. Secondly, the jet position is corrected in such a way that the axis points back to the interaction point. Then a correction is applied based on a comparison with a Monte Carlo simulation of the calorimeters to obtain values that approach the simulated jet energies E_{truth} more realistically. These corrections are needed to take into account that the sampling fraction $f \neq 1$ and that the calorimeter may have holes or dead regions through which potential energy contributions have leaked away. Moreover, the jet reconstruction may have resulted in signal loss. These issues are often referred to as the **JES uncertainties**. See Ref. [76] for a more detailed description on how these corrections are applied.

After some considerations stated in Ref. [76], we parametrise the correction as follows.

$$F_{\text{calib},k}(E_{\text{calo}}^{\text{EM}}) = \sum_{i=0}^{N_{\text{max}}} a_i (\ln E_{\text{calo}}^{\text{EM}})^i \tag{44}$$

$$E_{\text{calo}}^{\text{EM,JES}} = \frac{E_{\text{calo}}^{\text{EM}}}{F_{\text{calib},k}(E_{\text{calo}}^{\text{EM}})} \tag{45}$$

Here, $N_{\text{max}} \leq 6$. The measurement of high momentum jets is aided by the Tile Calorimeter, which sets its electromagnetic energy scale by calibration methods. The absolute value of the uncorrected energy $E_{\mathrm{calo}}^{\mathrm{EM}}$ influences the corrected energy $E_{\mathrm{calo}}^{\mathrm{EM,JES}}$. The correction function is implicitly dependent on the η bin that is to be corrected.

Qualitatively, it is clear that any miscalibration ϵ will linearly affect the measured energy by the calorimeter by $(1+\epsilon)E_{\mathrm{calo}}^{\mathrm{EM}}$. This means $E_{\mathrm{calo}}^{\mathrm{EM,JES}}$ will be ϵ-dependent. A typical jet may have a jet uncertainty of 2% and transverse momentum $p_T = 100$ GeV. The energy measurement of such a jet should match the Monte Carlo within a few GeV, such that no additional systematic error introduced by any miscalibration.

8 Results

The purpose of this thesis is to study the calibration of TileCal's gap/crack cells. These are the cells as described in section 4.2, namely C10, D4 and the scintillator tiles E1, E2, E3 and E4. A cell map is shown in figure 6. They were introduced into the gap/crack region between the long barrel and the endcap to reduce the systematic error on the energy measurement. Some of these cells have deviating dimensions to provide space for electric wires and cooling. These results for these special gap/crack cells are also shown here.

In this chapter, we will show which calorimeter cells in the gap/crack region are miscalibrated, obtained using the method described in section 6.7. Calibration constants will be tabulated to correct for the miscalibrations.

8.1 Energy depositions

The energy deposited in the cells is approximately linearly dependent on the track length, as can be seen in the scatterplots 31, 32 and 33.

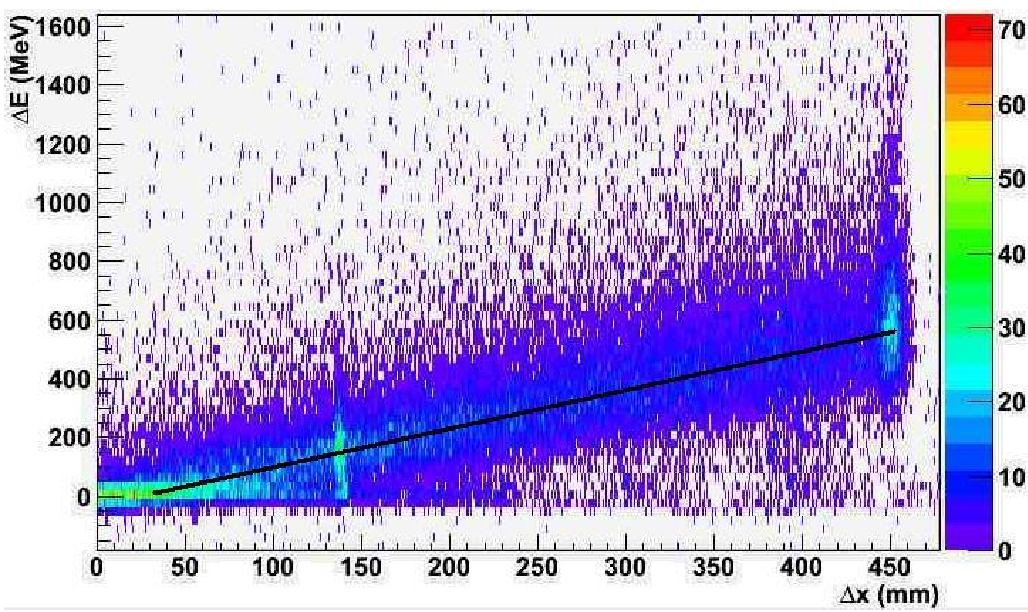

Figure 31: Deposited energy E versus the path length Δx of muons traversing the D4 cells. The D4 cell is a cuboid like all other D-cells. The slope of the straight black line is approximately 1 MeV/mm and represents the additional deposited energy per extra unit path length through D4.

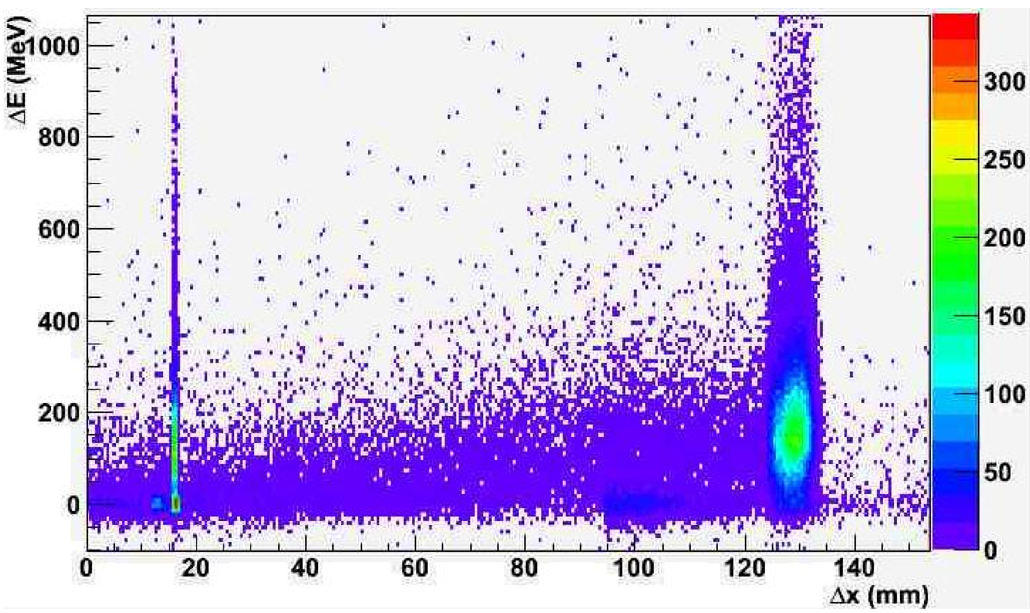

Figure 32: Deposited energy E versus the path length Δx of muons traversing the C10 cells. The normal C10 cell is a cuboid, but the special C10 cells are scintillators with a very limited thickness and can thus be associated to a limited path length of a track through the cell. The two different type of cells occupy very distinctive regions in the plot, around 130 mm and 16 mm respectively.

8.2 ϕ-uniformity

The ϕ-uniformity of response in the Monte Carlo is in dispute, as the response in the Monte Carlo cannot be described by a constant line. Module-by-module fluctuations are bigger than the statistical errors and the χ^2 probabilities associated to the constant fits vanish. A similar effect is observed in the data. These fluctuations are not taken out by computing the double ratios, as is depicted in figures 34 to 45 for all cells that interest us here. Therefore, a constant fit does not suffice for our study and a Gaussian fit method was introduced.

8.3 Calibration tables

With this method, we found a layer intercalibration that is comparable to previous studies, within a discrepancy of 4%, using all 2010 and 2011 data up to period 2011-H. Therefore, the method can be applied to study the specific cells in the Intermediate TileCal region. Miscalibrated cells are cells that deviate more than 3σ from the central value. The calibration factors for each of the miscalibrated cells are tabulated in table 9. Systematic errors introduced by the E and F cuts are included.

After taking out the miscalibrated cells, we compute the central values of the double

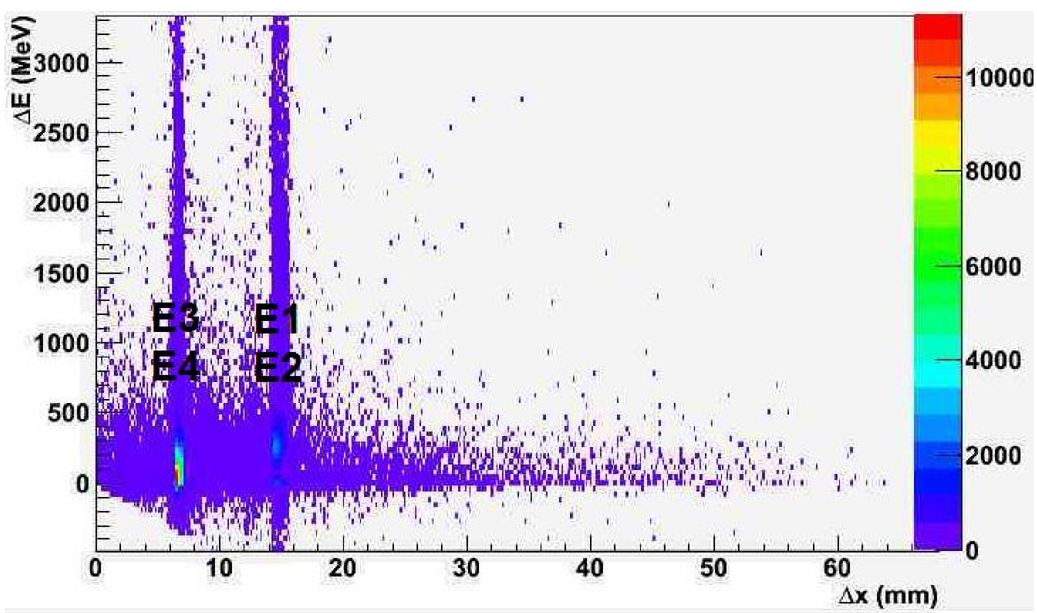

Figure 33: Deposited energy E versus the path length Δx of muons traversing the gap/crack scintillators E1, E2, E3 and E4. The scintillating tiles have a very limited thickness. This makes it unlikely to find large values for Δx, and also $\Delta x = 0$ is quite improbable.

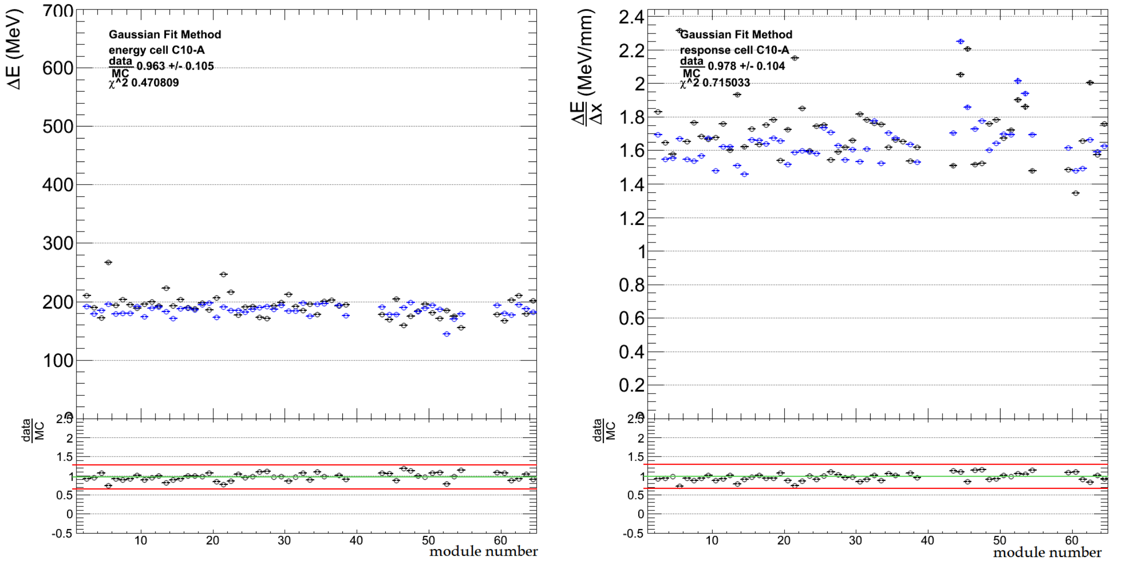

Figure 34: Energy deposited by muons from $W \to \mu\nu$ *(left)* and the cell response dE/dx *(right)* as a function of module m in **C10, A-side**. The cuts used here are $E = 60$ MeV, $F = 1\%$. The data/Monte Carlo ratios are shown.

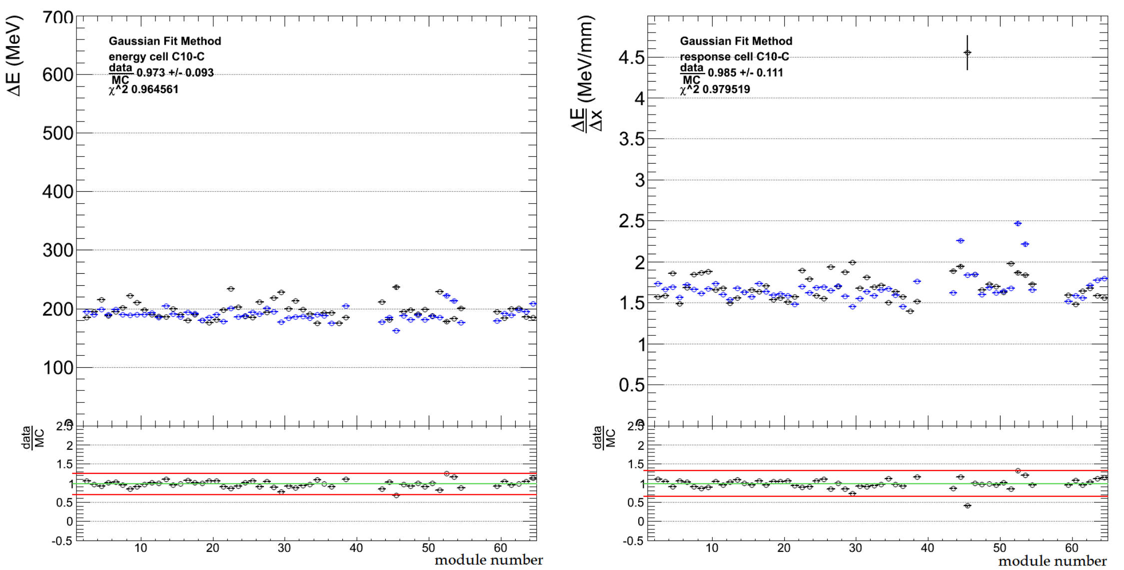

Figure 35: Energy deposited by muons from $W \to \mu\nu$ *(left)* and the cell response dE/dx *(right)* as a function of module m in **C10, C-side**. The cuts used here are $E = 60$ MeV, $F = 1\%$. The data/Monte Carlo ratios are shown.

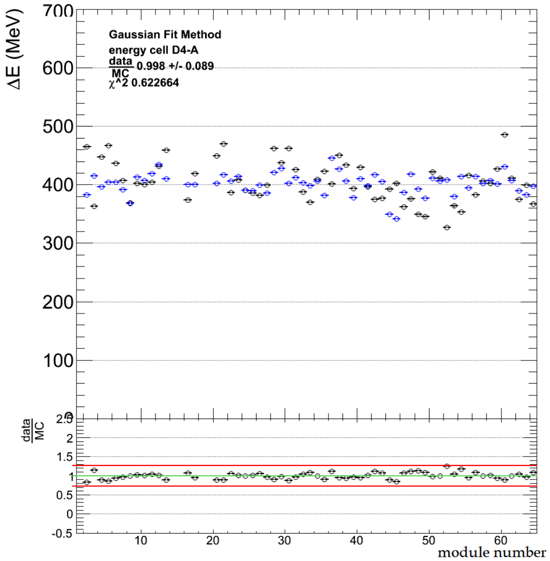

Figure 36: Energy deposited by muons from $W \to \mu\nu$ *(left)* and the cell response dE/dx *(right)* as a function of module m in **D4, A-side**. The cuts used here are $E = 60$ MeV, $F = 1\%$. The data/Monte Carlo ratios are shown.

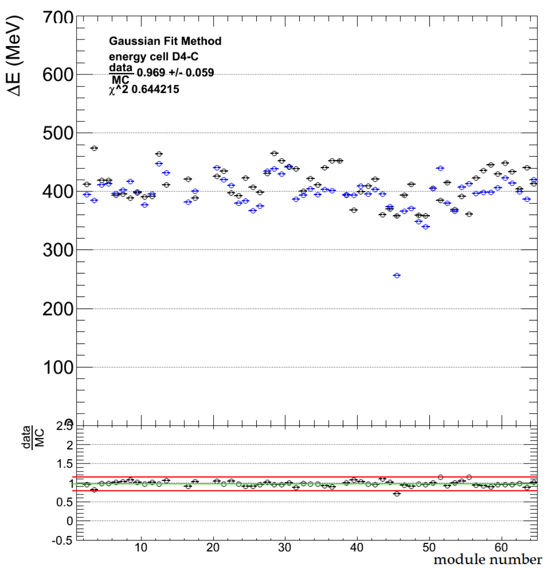

Figure 37: Energy deposited by muons from $W \to \mu\nu$ *(left)* and the cell response dE/dx *(right)* as a function of module m in **D4, C-side**. The cuts used here are $E = 60$ MeV, $F = 1\%$. The data/Monte Carlo ratios are shown.

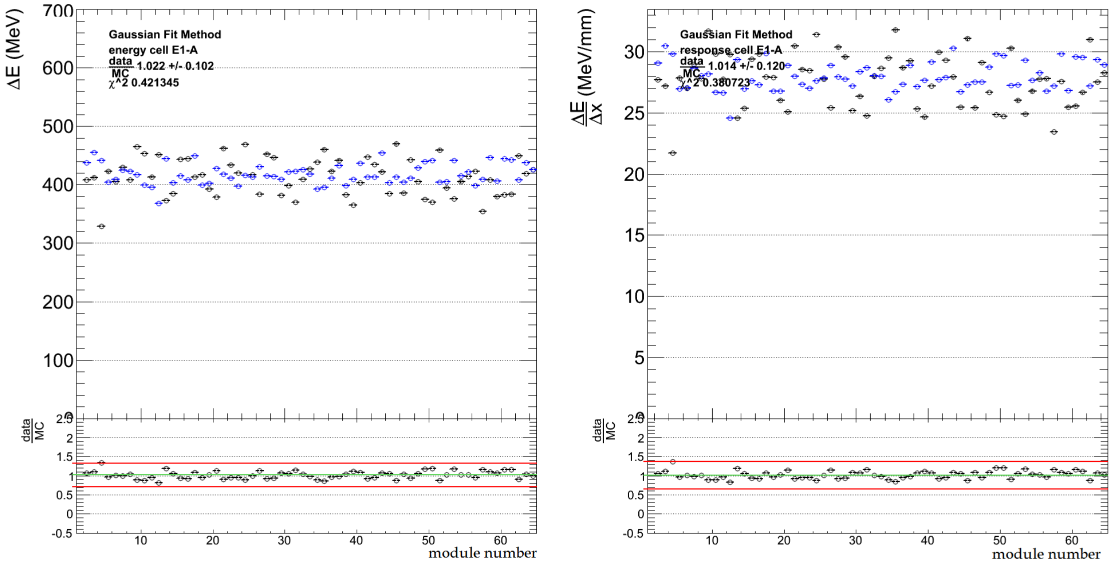

Figure 38: Energy deposited by muons from $W \to \mu\nu$ *(left)* and the cell response dE/dx *(right)* as a function of module m in **E1, A-side**. The cuts used here are $E = 60$ MeV, $F = 1\%$. The data/Monte Carlo ratios are shown.

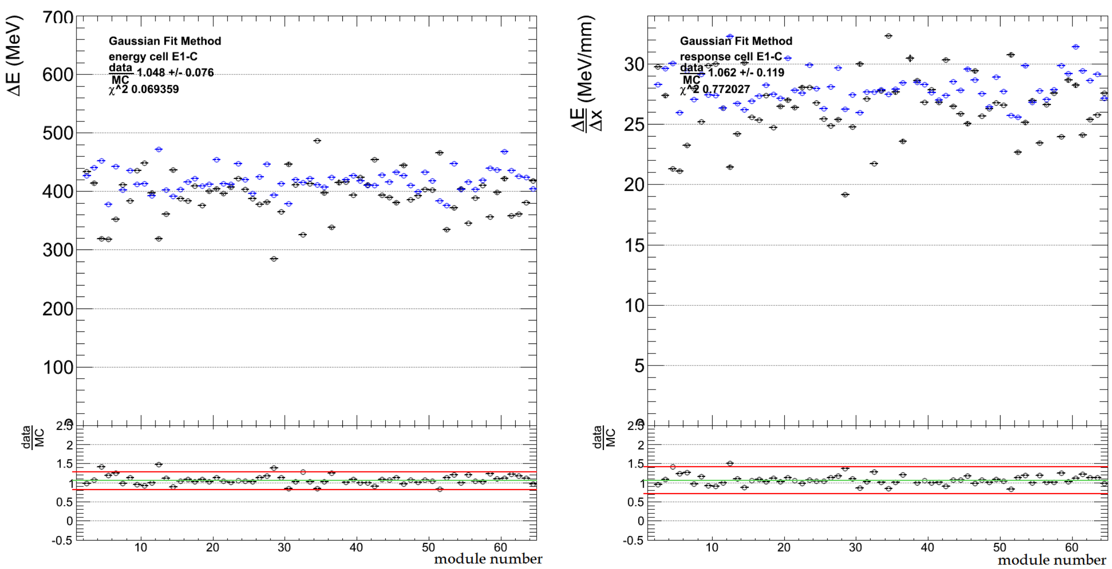

Figure 39: Energy deposited by muons from $W \to \mu\nu$ *(left)* and the cell response dE/dx *(right)* as a function of module m in **E1, C-side**. The cuts used here are $E = 60$ MeV, $F = 1\%$. The data/Monte Carlo ratios are shown.

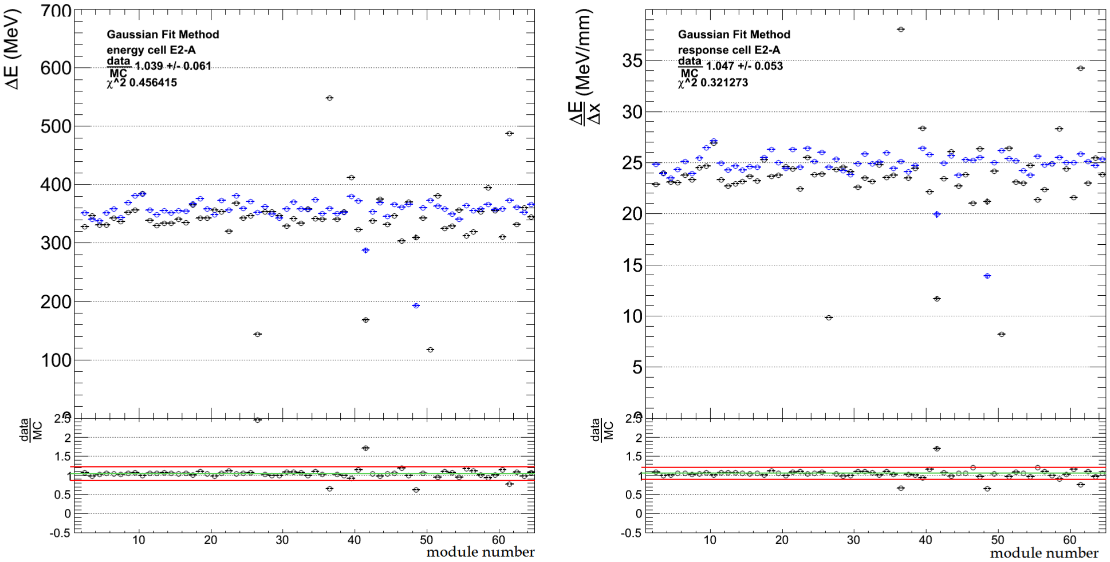

Figure 40: Energy deposited by muons from $W \rightarrow \mu\nu$ *(left)* and the cell response dE/dx *(right)* as a function of module m in **E2, A-side**. The cuts used here are $E = 60$ MeV, $F = 1\%$. The data/Monte Carlo ratios are shown.

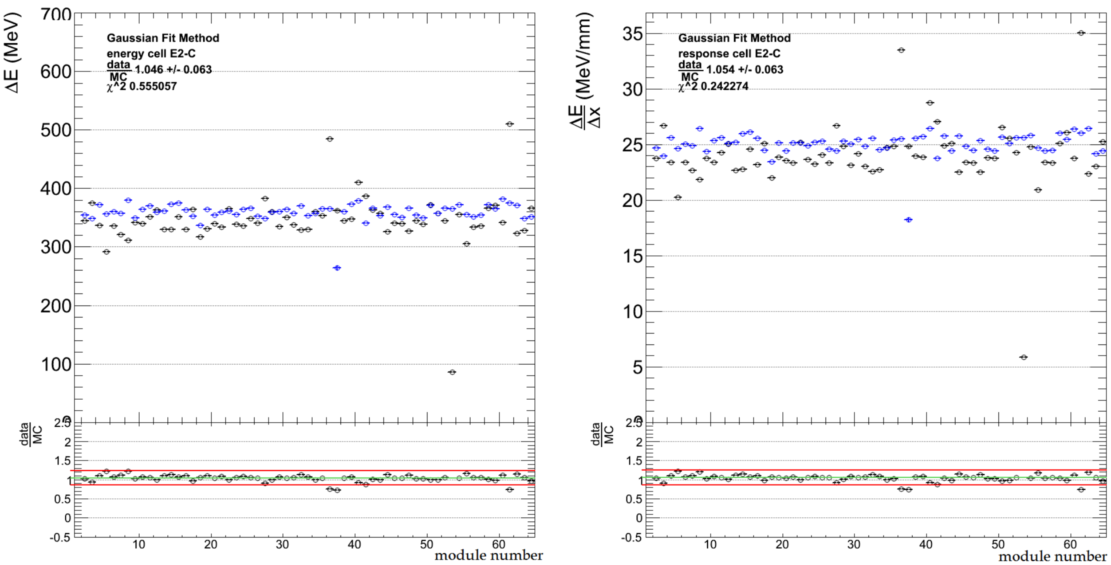

Figure 41: Energy deposited by muons from $W \rightarrow \mu\nu$ *(left)* and the cell response dE/dx *(right)* as a function of module m in **E2, C-side**. The cuts used here are $E = 60$ MeV, $F = 1\%$. The data/Monte Carlo ratios are shown.

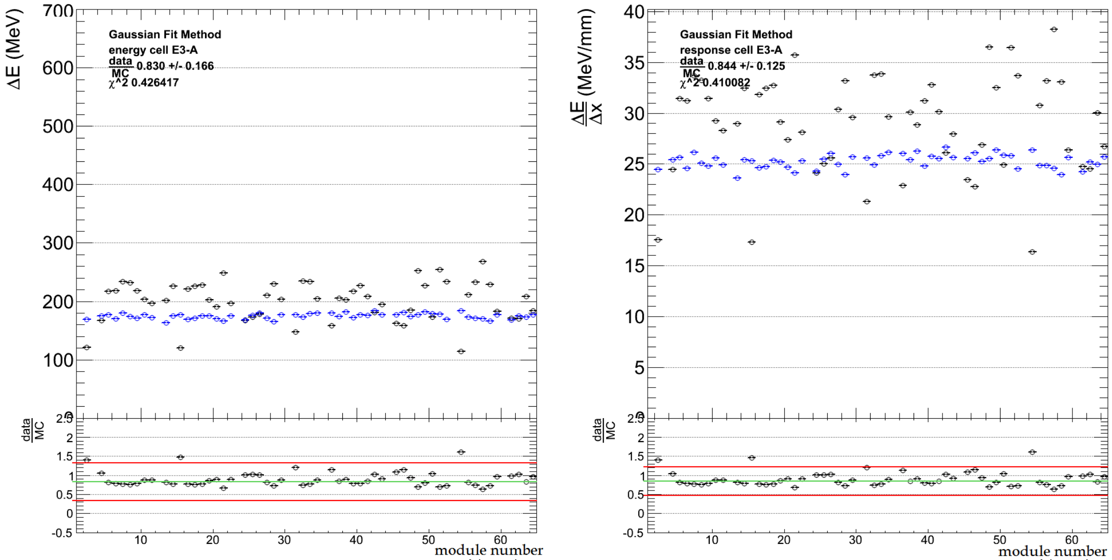

Figure 42: Energy deposited by muons from $W \to \mu\nu$ *(left)* and the cell response dE/dx *(right)* as a function of module m in **E3, A-side**. The cuts used here are $E = 60$ MeV, $F = 1\%$. The data/Monte Carlo ratios are shown.

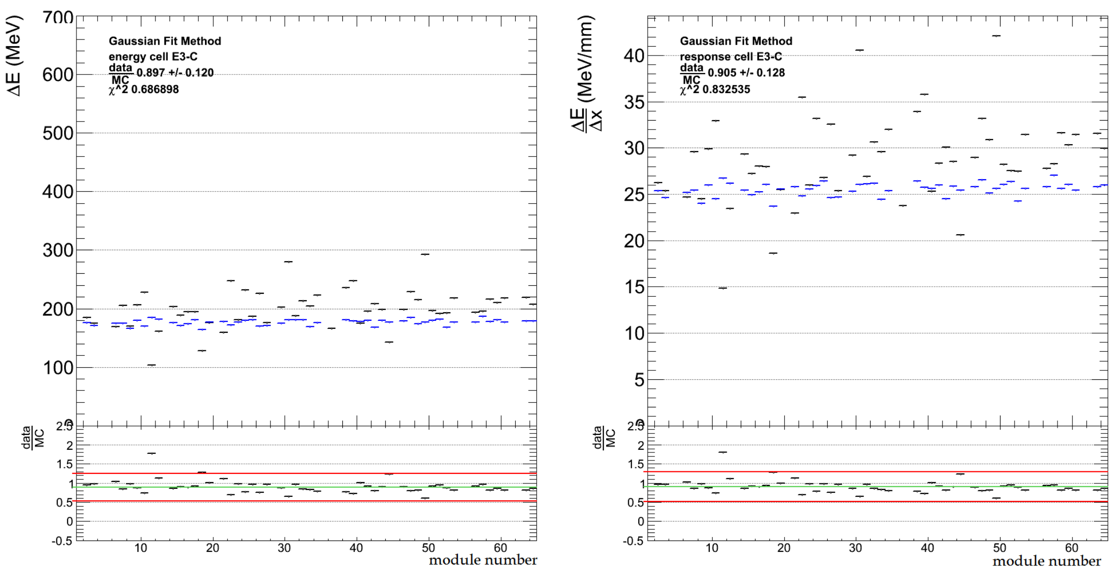

Figure 43: Energy deposited by muons from $W \to \mu\nu$ *(left)* and the cell response dE/dx *(right)* as a function of module m in **E3, C-side**. The cuts used here are $E = 60$ MeV, $F = 1\%$. The data/Monte Carlo ratios are shown.

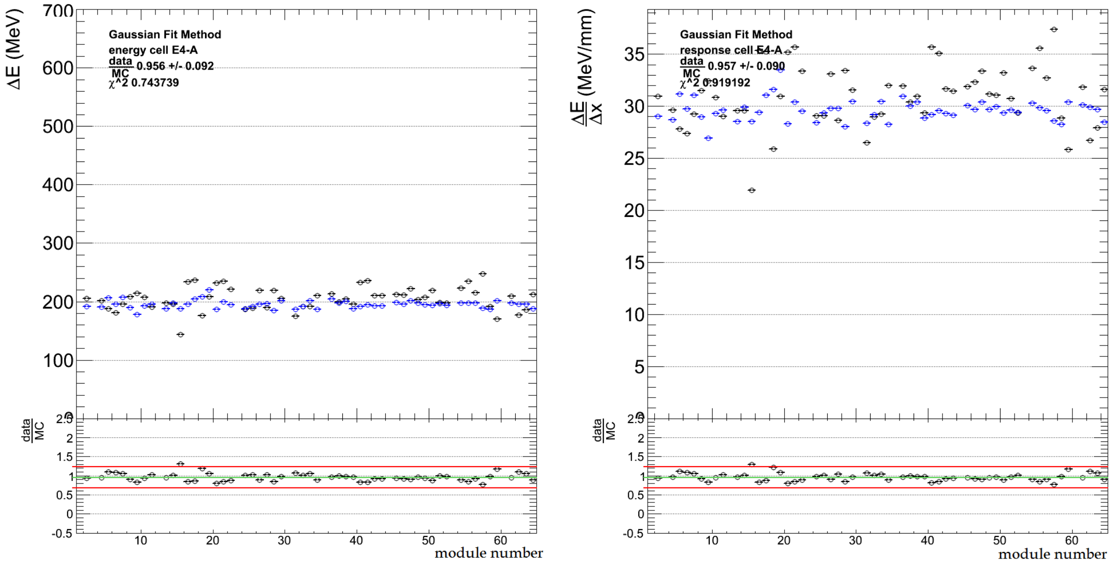

Figure 44: Energy deposited by muons from $W \to \mu\nu$ *(left)* and the cell response dE/dx *(right)* as a function of module m in **E4, A-side**. The cuts used here are $E = 60$ MeV, $F = 1\%$. The data/Monte Carlo ratios are shown.

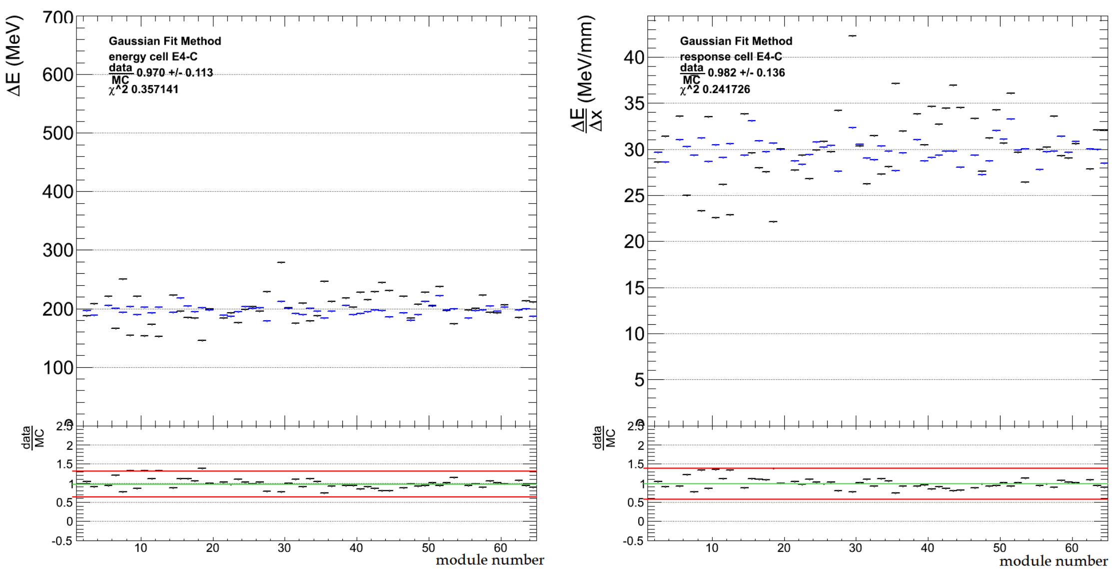

Figure 45: Energy deposited by muons from $W \to \mu\nu$ *(left)* and the cell response dE/dx *(right)* as a function of module m in **E4, C-side**. The cuts used here are $E = 60$ MeV, $F = 1\%$. The data/Monte Carlo ratios are shown.

cell	module	CalFactor(m)
C10	45-C	$1.4621^{+0.01216}_{-0.01222}$
	52-C	$0.8008^{+0.07878}_{-0.07878}$
special C10		
D4	2-A	$1.2153^{+0.02041}_{-0.00237}$
	3-A	$0.8743^{+0.04000}_{-0.01980}$
	5-A	$1.1545^{+0.00175}_{-0.04265}$
	10-A	$0.9843^{+0.00196}_{-0.00981}$
	13-A	$1.1193^{+0.05074}_{-0.04148}$
	29-A	$1.0241^{+0.03602}_{-0.11255}$
	30-A	$1.1506^{+0.01938}_{-0.01410}$
	31-A	$1.0326^{+0.00547}_{-0.01131}$
	36-A	$0.9020^{+0.00824}_{-0.00775}$
	38-A	$1.0674^{+0.00386}_{-0.01268}$
	50-A	$1.0260^{+0.07485}_{-0.00376}$
	51-A	$1.0108^{+0.08641}_{-0.02322}$
	52-A	$0.8016^{+0.05055}_{-0.23198}$
	54-A	$0.8535^{+0.01874}_{-0.06202}$
	64-A	$0.9238^{+0.00484}_{-0.00524}$
special D4		
E1	12-C	$0.6764^{+0.02810}_{-0.03200}$
E2	26-A	$0.4070^{+0.00855}_{-0.01203}$
	36-A	$1.5240^{+0.04140}_{-0.01722}$
	41-A	$0.5848^{+0.58495}_{-0.77402}$
	48-A	$1.6092^{+0.18460}_{-0.62358}$
	50-A	$0.3129^{+0.01765}_{-0.04201}$
	61-A	$1.3076^{+0.00484}_{-0.03653}$
	12-C	$0.6764^{+0.35738}_{-0.32854}$
	36-C	$1.3289^{+0.00135}_{-0.00176}$
	37-C	$1.3716^{+0.13584}_{-0.09258}$
	53-C	$0.2341^{+0.03767}_{-0.05364}$
	61-C	$1.3616^{+0.00918}_{-0.02509}$
E3	2-A	$0.7156^{+0.00454}_{-0.03324}$
	15-A	$0.6800^{+0.00993}_{-0.00364}$
	54-A	$0.6198^{+0.00777}_{-0.04624}$
	11-C	$0.5634^{+0.00746}_{-0.12823}$
E4	15-A	$0.7647^{+0.01284}_{-0.00409}$

Table 9: Miscalibrated cells in the Tile Calorimeter gap/crack region. Calibration constants **CalFactor**(m) are calculated based upon data from 2010 (all) and 2011 (B-I).

ratios using 2010 and 2011 data, up to data taking period 2011-H, listed in table 10.

cell	$\mu_{c,p,60,1} \pm \frac{\sigma_{c,p,60,1}}{\sqrt{N}}(\text{stat.})^{+\delta_{E=90}}_{-\delta_{E=30}}(E)^{+\delta_{F=2}}_{+\delta_{F=0}}(F)$
C10-A	$0.9628 \pm 0.01466^{+0.01808}_{-0.00622}$
C10-C	$0.9848 \pm 0.01584^{+0.01229}_{-0.01234}$
special C10-A	$0.9741 \pm 0.03554^{+1.44176}_{+0.08258}$
special C10-C	$0.9171 \pm 0.03145^{+0.03245}_{-0.01556}$
D4-A	$0.9977 \pm 0.01111^{-0.00790}_{-0.00825}$
D4-C	$0.9691 \pm 0.07007^{-0.00335}_{+0.00163}$
special D4-A	$0.9297 \pm 0.09568^{+0.00539}_{-0.03010}$
special D4-C	$0.95978 \pm 0.12656^{-0.03549}_{-0.02366}$
E1-A	$1.02190 \pm 0.01276^{+0.01466}_{-0.02375}$
E1-C	$1.04762 \pm 0.00949^{+0.01508}_{-0.01294}$
E2-A	$1.03886 \pm 0.00762^{-0.00953}_{-0.00287}$
E2-C	$1.04615 \pm 0.00789^{+0.00757}_{-0.00659}$
E3-A	$0.83024 \pm 0.02073^{-0.01669}_{-0.01239}$
E3-C	$0.89662 \pm 0.01502^{+0.00133}_{-0.03550}$
E4-A	$0.95590 \pm 0.01153^{+0.00479}_{-0.04572}$
E4-C	$0.97000 \pm 0.01417^{-0.02563}_{-0.02206}$

Table 10: Central values $\mu_{c,p,E,F}$ obtained by using the Gaussian fit method on the double ratio $R_{c,p,E,F}(m)$ distributions from 2010-2011 data. The statistical error is denoted by $\sigma_{c,p,60,1}/\sqrt{N}$ and the systematic errors introduced by truncating and cutting in energy are given by ${}^{+\delta_{E=90}}_{-\delta_{E=30}}(E)^{+\delta_{F=2}}_{+\delta_{F=0}}(F)$. Miscalibrated cells have been taken out.

The maximum likelihood method described in section 6.10 can also be used to quantify the intercalibration, taking into account a second parameter s that measures the smearing. The results produced with this method, after applying the usual cuts and Monte Carlo reweighting, are tabulated in table 11. Systematic errors are included in the analysis for either the double ratios and smearing parameters.

cell	$\mu_{c,p,60,1} \pm \frac{\sigma_{c,p,60,1}}{\sqrt{N}}(\text{stat.})^{+\delta_{E=90}}_{-\delta_{E=30}}(E)^{+\delta_{F=2}}_{+\delta_{F=0}}(F)$	$s \pm \frac{\sigma_s}{\sqrt{N}}(\text{stat.})^{+\delta_{E=90}}_{-\delta_{E=30}}(E)^{+\delta_{F=2}}_{+\delta_{F=0}}(F)$
C10	$1.012 \pm 0.005^{+0.022+0.026}_{-0.010-0.019}$	$0.000 \pm 0.230^{+0.068+0.068}_{+0.066+0.054}$
D4	$1.010 \pm 0.007^{-0.001+0.007}_{-0.002-0.023}$	$0.055 \pm 0.006^{-0.004-0.003}_{-0.006+0.005}$
E1	$0.952 \pm 0.009^{+0.007+0.003}_{-0.012+0.005}$	$0.082 \pm 0.008^{-0.002+0.001}_{-0.001-0.002}$
E2	$0.952 \pm 0.013^{+0.014+0.000}_{-0.009-0.000}$	$0.135 \pm 0.009^{-0.028-0.001}_{+0.007+0.001}$
E3	$1.120 \pm 0.018^{-0.001+0.007}_{-0.053-0.006}$	$0.178 \pm 0.013^{-0.037+0.004}_{+0.017-0.008}$
E4	$0.961 \pm 0.011^{-0.042+0.003}_{-0.006+0.003}$	$0.106 \pm 0.008^{-0.035+0.002}_{+0.021-0.008}$

Table 11: Quantifying the intercalibration of TileCal gap/crack cells using a maximum likelihood method. An additional smearing factor s is introduced to model fluctuations of the double ratio with respect to the central value.

9 Conclusions and outlook

One can use a 3‰ significance level to reject the hypothesis that a module is calibrated, using a gaussian fit to obtain the central value and the standard deviation of the double ratio R = data/MC.

In this study, we checked the response of the TileCal cells in the gap/crack region to $W \to \mu\nu_\mu$ collision muons and found that 3 C10 cells are miscalibrated. Amongst the scintillators, 2 E1 cells, 7 E2 cells and 1 E4 cell were found to be miscalibrated. The calibration constants provided in table 9 should be applied to correct for these miscalibrations.

The intercalibrations found by the Gaussian fit method, tabulated in table 10, do not quite agree with cosmics results that were obtained earlier this year. See Ref. [64]. Values of the central values using the Gaussian fit overestimate the values obtained using cosmics by 3-15% with respect to the previous study. This discrepancy is not understood and requires further attention. It must be pointed out however, that the momentum range chosen in the cosmics study, $p_\mu > 10$ GeV, does not agree with the selection to obtain a clean muon track sample used in this collision study, namely $p_\mu > 40$ GeV. Moreover, for the scintillators E3 and E4 that cannot be calibrated by the cesium system, no energy cut E was used in the cosmics study.

Overall, different cell types are intercalibrated between ranges of -11% and +4%.

Using a maximum likelihood method, we find that the intercalibration is between -5% and +1%. The smearing s quantifies some unknown systematic that may explain the non-uniformities found in the data. The smearing is found to take on values between the minimum of 0% for C10 and the maximum of 18% for the E3 scintillator.

We have found that calibrating the Tile Calorimeter is important in setting the jet energy scale.

This year and next year, more collision data will be recorded that can be used to monitor the calibration of our hadronic calorimeter, before the planned technical stop commences in 2013. This calibration campaign needs continuous attention of the experimentalists working in the TileCal collaboration, as an optimal calibration is the key to a just energy measurement. If we can convince ourselves that the Intermediate Tile Calorimeter is properly calibrated and well understood by simulations, we may fully utilise its potential experimental value, increasing the overall achieved energy resolution. A better energy resolution means that less data is necessary to study interesting physics channels, taking us one step closer to discovery.

Notes

[1]Einstein postulated that the speed of light c is invariant under Lorentz transformation. A light pulse moving back and forth a distance d between two mirrors takes $t = \frac{2d}{c}$ per turn. An observer in a moving train, however, measures $t = \gamma \frac{2d}{c}$ per turn, due to this postulate. The γ factor takes into account that the travelled distance has increased, but the speed remained the same value, and follows from direct calculation.

[2]$\epsilon_s = 4\pi\sigma_t\sigma_{\delta E/E_0}E_0$, where σ_t is the bunch duration in seconds, $\sigma_{\Delta E/E_0}$ the relative energy spread and E_0 the beam energy.

Appendices

A. Path reconstruction in TileCal

Consider a muon track t, extrapolated to all detector layers using the **ATLAS Track-Extrapolator** functionality in ATHENA. **What is the path of this track t through cell c?** The track extrapolator parametrises the track in three dimensions. One obtains the layer l dependent coordinates $(r_n(l), \phi_n(l), \eta_n(l))$ or $(x_n(l), y_n(l), z_n(l))$ for each track. Here, n counts the number of track parameters per layer. This may be more than one, depending on the quality of the extrapolation. Continuing in Cartesian coordinates as defined in section 1.4, we enclose a cell by the two adjacent layers that are also crossed by the track.

Now, let (x_0, y_0, z_0) be the point where the extrapolated track intersects the adjacent layer that is further away from the interaction point than the cell itself. Similarly, we define (x_1, y_1, z_1) on the layer that is closer to the interaction point. In other words, $z_1 < z_c < z_0$ for cells with $\eta > 0$ and $z_0 < z_c < z_l$ for cells with $\eta < 0$. The first step is to calculate the coordinates of the points where the track intersects the inner and outer radial planes of the cell. In the ROOT analysis, the two cylinders at $R_{-'} = r_c -' \frac{\Delta r_c}{2}$ and $R_{+'} = r_c +' \frac{\Delta r_c}{2}$ are considered. Some algebra reveals that the coordinates are given by $(x_\pm, y_\pm, z_\pm)$.

$$\begin{aligned}
x_\pm &= \frac{-b \pm \sqrt{b^2 - 4ac}}{2a} \\
y_\pm &= y_0 + \frac{y_1 - y_0}{x_1 - x_0}\left(\frac{-b \pm \sqrt{b^2 - 4ac}}{2a} - x_0\right) \\
z_\pm &= z_0 + \frac{z_1 - z_0}{x_1 - x_0}\left(\frac{-b \pm \sqrt{b^2 - 4ac}}{2a} - x_0\right)
\end{aligned} \tag{46}$$

One computes a, b and c as follows.

$$\begin{aligned}
a &= 1 + \left(\frac{y_1 - y_0}{x_1 - x_0}\right)^2 \\
b &= 2\frac{y_1 - y_0}{x_1 - x_0}\left(y_0 - \frac{y_1 - y_0}{x_1 - x_0}x_0\right) \\
c &= y_0^2 + R_{\pm'}^2 + \left(\frac{y_1 - y_0}{x_1 - x_0}\right)^2 x_0^2 - 2x_0 y_0 \frac{y_1 - y_0}{x_1 - x_0} && (47) \\
& && (48)
\end{aligned}$$

The index $\pm$ is based on whether plus or minus results in the lowest value for $(x_\pm - x_0)^2 + (y_\pm - y_0)^2 + (z_\pm - z_0)^2$. After this calculation has been performed for both $R_{\pm'}$, one checks whether the track has intersected or missed the cell with these values. To do this, one first looks at the (ϕ, z) coordinates. If both requirements $z_\pm \in \left[z_c - \frac{\Delta z_c}{2}, z_c + \frac{\Delta z_c}{2}\right]$ and $\phi_\pm \in \left[\phi_c - \frac{\Delta \phi_c}{2}, \phi_c + \frac{\Delta \phi_c}{2}\right]$ hold, one intersection of the track with the cell has been found. In fact, if both requirements hold for either the inner and outer radial surfaces, the path length of the track through the cell is readily computed.

$$\Delta x = \sqrt{(x_{\pm,\text{inner}} - x_{\pm,\text{outer}})^2 + (y_{\pm,\text{inner}} - y_{\pm,\text{outer}})^2 + (z_{\pm,\text{inner}} - z_{\pm,\text{outer}})^2} \tag{49}$$

However, the three-dimensional cell has six sides. If only one intersection point is found using the above described method, it is quite likely that the other intersection point can be found on the remaining four sides. These four sides can be characterised in words by the plane at $z_{c,\min}$, the plane at $z_{c,\max}$, the plane at $\phi_{c,\min}$ and the plane at $\phi_{c,\max}$. Let us calculate the Cartesian coordinates of the extrapolated tracks in these planes, respectively.

$$\begin{aligned}
x_{\text{plane}} &= x_1 + \tfrac{x_0 - x_1}{z_0 - z_1}\left(z_{c,\min/\max} - z_1\right) \\
y_{\text{plane}} &= y_1 + \tfrac{y_0 - y_1}{z_0 - z_1}\left(z_{c,\min/\max} - z_1\right) \\
z_{\text{plane}} &= z_{c,\min/\max} && (50) \\
& && (51)
\end{aligned}$$

$$\begin{aligned}
x_{\text{plane}} &= \frac{x_1 - \frac{x_0 - x_1}{y_0 - y_1} y_1}{1 - \frac{x_0 - x_1}{y_0 - y_1} \tan\phi_{c,\min/\max}} \\
y_{\text{plane}} &= x_{\text{intersection}} \tan\phi_{c,\min/\max} \\
z_{\text{plane}} &= z_1 + \tfrac{z_0 - z_1}{x_0 - x_1}\left(x_{\text{intersection}} - x_1\right) && (52) \\
& && (53)
\end{aligned}$$

These coordinates are intersections if all following requirements are fulfilled.

$$\begin{aligned}
R_{\pm} &\in [R_{c,\min}, R_{c,\max}] \\
\phi_{\pm} &\in [\phi_{c,\min}, \phi_{c,\max}] \\
z_{\pm} &\in [z_{c,\min}, z_{c,\max}]
\end{aligned} \tag{54}$$

When two intersection points are found, one applies equation 49 to get the path length Δx.

B. Cells in the Intermediate TileCal region

The dimensions of the relevant cells are shown here. Table 12 lists the module numbers and (R, z) dimensions for all the **special cells** in the ITC region. Special cells are necessary to provide space for cables and electronics and are always smaller than the normal specimens in the same layer.

partition	**module**	**cell**	R	dR	$\|z\|$	dz	**remarks**
EBA	42/55	C10	3215	450	3511	12	scintillator
EBA	39/40/41/56/57/58	C10	3215	450	3511	12	scintillator
EBC	42/55	C10	3215	450	3501	12	scintillator
EBC	39/40/41/56/57/58	C10	3215	450	3501	12	scintillator
EBA	14/18/19	D4	3630	380	3405	95	reduced size
EBC	14/15/19	D4	3630	380	3395	95	reduced size
EBA	15	D4	3630	380	3405	308.3	merged with D5
EBC	18	D4	3630	380	3395	308.3	merged with D5

Table 12: Dimensions of the TileCal special cells in the ITC region, in mm.

Table 13 lists the η positions and (R, z) dimensions for all the normal cells in the ITC region.

cell	$\|\eta\|$	R	dR	$\|z\|$	dz	**remarks**
C10	0.96	3215	450	3511	95	A-side
C10	0.96	3215	450	3501	95	C-side
D4	0.86	3630	380	3405	309	A-side
D4	0.86	3630	380	3395	309	C-side
E1	1.06	2803	313	3552	12	gap scintillator, A-side
E1	1.06	2803	313	3542	12	gap scintillator, C-side
E2	1.16	2476	341	3552	12	gap scintillator, A-side
E2	1.16	2476	341	3542	12	gap scintillator, C-side
E3	1.31	2066	478	3536	6	crack scintillator, A-side
E3	1.31	2066	478	3526	6	crack scintillator, C-side
E4	1.51	1646	362	3536	6	crack scintillator, A-side
E4	1.51	1646	362	3526	6	crack scintillator, C-side

Table 13: Dimensions of the normal TileCal cells in the ITC region, in mm.

There exists a one-to-one and onto mapping between the ϕ coordinate and module number m, tabulated in 14.

module	ϕ (rad)	**module**	ϕ (rad)	**module**	ϕ (rad)	**module**	ϕ (rad)
1	0.0491	17	1.6199	33	-3.0925	49	-1.5217
2	0.1473	18	1.7181	34	-2.9943	50	-1.4235
3	0.2454	19	1.8162	35	-2.8962	51	-1.3254
4	0.3436	20	1.9144	36	-2.7980	52	-1.2272
5	0.4418	21	2.0126	37	-2.6998	53	-1.1290
6	0.5400	22	2.1108	38	-2.6016	54	-1.0308
7	0.6381	23	2.2089	39	-2.5035	55	-0.9327
8	0.7363	24	2.3071	40	-2.4053	56	-0.8345
9	0.8345	25	2.4053	41	-2.3071	57	-0.7363
10	0.9327	26	2.5035	42	-2.2089	58	-0.6381
11	1.0308	27	2.6016	43	-2.1108	59	-0.5400
12	1.1290	28	2.6998	44	-2.0126	60	-0.4418
13	1.2272	29	2.7980	45	-1.9144	61	-0.3436
14	1.3254	30	2.8962	46	-1.8162	62	-0.2454
15	1.4235	31	2.9943	47	-1.7181	63	-0.1473
16	1.5217	32	3.0925	48	-1.6199	64	-0.0491

Table 14: ϕ coordinates for all 64 TileCal modules m. The module numbers can be mapped bijectively to the ϕ interval $(-\pi, \pi)$. Please note $|\Delta\phi| = 0.0982$ for $|\Delta m| = 1$. The module numbers are defined in such a way that $m(\phi)$ is discontinuous at $\phi = 0$.

D. Cross calibration

Especially useful in diagnosing problems or monitoring the time stability is to check the correspondence between the different calibration systems. It would serve as a validation of the calibration systems when a PMT gain variation (for example) that is spotted by the laser system is also detected in the next cesium run.

In the context of this study, a macro has been created concerning the cross calibration. One could perform a Kolmogorov-Smirnov test to check or consistency amongst the calibration systems. A Kolmogorov-Smirnov test uses the accumulative distributions to enable one to compare two samples of measured values. One expects the different calibration stems to respond to changes in a similar way. In particular, the laser system should complement the cesium system. The (module,channel,p) histogram is in particular interest here, where p is the Kolmogoriv-Smirnov probability. It measures the degree of correspondence between two systems.

Moreover, a graphical user interface was developed to display the output of the SaveTree worker. This worker retrieves the calibration constants of the different systems and stores them into a single Ntuple, organised by detector region.

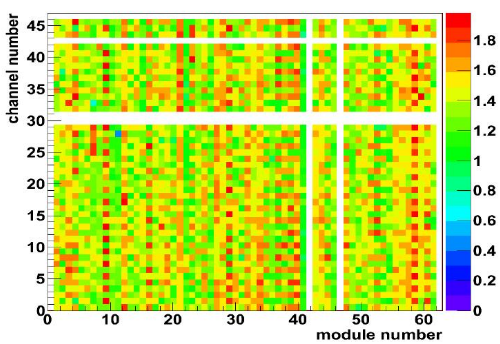

Figure 46: Relative Kolmogorov-Smirnov probability densities for the TileCal LBC partition obtained by comparing the deviations in laser system and charge injection system. The values are not normalised. The white lines reveal that for some modules and cells, the Ntuples used over this period (May 2010 - March 2011) did not contain data.

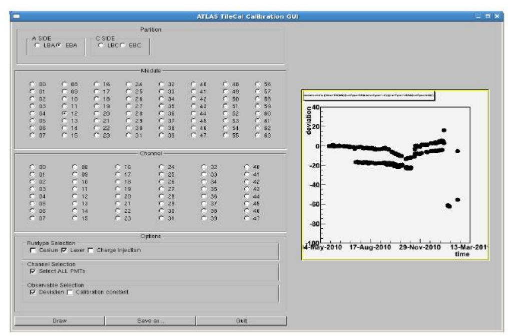

Figure 47: A graphical user interface was developed that handles the output of the SaveTree worker. It has not been actively used sofar. The structure of the detector in terms of partitions, modules and channels is displayed in the options menu on the left. On the right, we can see the deviations in the laser constant plotted for the extended barrel (A-side), module 12.

E. Momentum cut and period dependencies

In tables 15 and 16, we list the central values from the Gaussian fit method for the different layers and each period, cutting the energy at 30 MeV and 90 MeV respectively.

layer	**2010**	**2011-D**	**2011-E**	**2011-F**	**2011-G**	**2011-H**
LB-A	0.9508 ± 0.0041	0.9702 ± 0.0039	0.8806 ± 0.0067	0.9582 ± 0.0047	0.9693 ± 0.0058	0.9589 ± 0.0032
LB-BC	0.9768 ± 0.0038	0.9838 ± 0.0033	0.9285 ± 0.0063	0.9862 ± 0.0043	1.0024 ± 0.0027	0.9798 ± 0.0030
LB-D	0.9751 ± 0.0043	0.9443 ± 0.0054	0.9462 ± 0.0106	0.9678 ± 0.0050	1.0049 ± 0.0033	0.9918 ± 0.0035
EB-A	0.9706 ± 0.0034	0.9874 ± 0.0031	0.9316 ± 0.0059	0.9709 ± 0.0037	0.9962 ± 0.0023	0.9922 ± 0.0026
EB-BC	0.9617 ± 0.0025	0.9753 ± 0.0024	0.9377 ± 0.0044	0.9598 ± 0.0027	0.9675 ± 0.0017	0.9746 ± 0.0020
EB-D	0.9525 ± 0.0031	0.9627 ± 0.0031	0.9058 ± 0.0060	0.9601 ± 0.0038	0.9754 ± 0.0024	0.9768 ± 0.0028

Table 15: Central values $\mu_{c,p,E,F}$ obtained by using the Gaussian fit method on the double ratio $R_{c,p,E,F}(m)$ distributions. The energy cut E is taken to be 30 MeV, the truncation level F is 1%. The errors shown are the statistical errors.

layer	**2010**	**2011-D**	**2011-E**	**2011-F**	**2011-G**	**2011-H**
LB-A	0.9599 ± 0.0040	0.9716 ± 0.0038	0.8936 ± 0.0064	1.0000 ± 0.0000	1.0000 ± 0.0000	0.9657 ± 0.0031
LB-BC	0.9776 ± 0.0037	0.9880 ± 0.0034	0.9323 ± 0.0062	1.0000 ± 0.0000	1.0000 ± 0.0000	0.9820 ± 0.0029
LB-D	0.9756 ± 0.0043	0.9811 ± 0.0040	0.9479 ± 0.0105	1.0000 ± 0.0000	1.0000 ± 0.0000	0.9915 ± 0.0035
EB-A	0.9880 ± 0.0034	0.9956 ± 0.0031	0.9386 ± 0.0058	1.0000 ± 0.0000	1.0000 ± 0.0000	0.9992 ± 0.0027
EB-BC	0.9655 ± 0.0035	0.9761 ± 0.0024	0.9376 ± 0.0045	1.0000 ± 0.0000	1.0000 ± 0.0000	0.9751 ± 0.0031
EB-D	0.9539 ± 0.0031	0.9589 ± 0.0031	0.9057 ± 0.0060	1.0000 ± 0.0000	1.0000 ± 0.0000	0.9819 ± 0.0029

Table 16: Central values $\mu_{c,p,E,F}$ obtained by using the Gaussian fit method on the double ratio $R_{c,p,E,F}(m)$ distributions. The energy cut E is taken to be 90 MeV, the truncation level F is 1%. The errors shown are the statistical errors.

Interestingly, the response is found to drift over time. In the gap/crack region, we find an upward drift as displayed in figure 48.

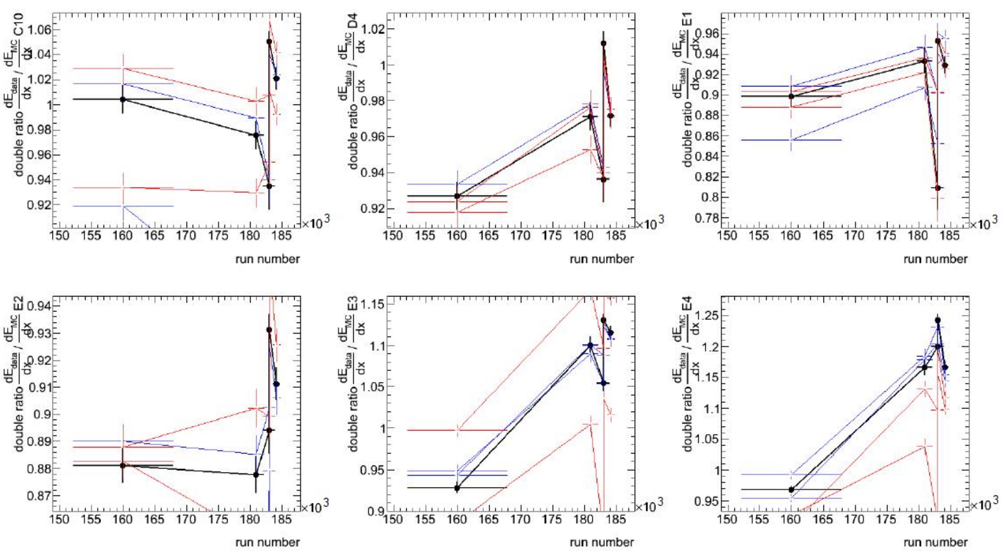

Figure 48: Time evolution of the response double ratio $(dE/dx)_{\mathrm{data}}/(dE/dx)_{\mathrm{MC}}$. The data points correct to periods 2010, 2011-D, 2011-F, 2011-G and 2011-H. An up-drift of approximately 6% is visible. From left top to right bottom are displayed C10, D4, E1, E2, E3 and E4. The black line is generated using $E = 60$ MeV, $F = 1\%$, the blue line by varying the energy cut by ± 30 MeV with respect to the black line, and the red line by varying the truncation level by $\pm 1\%$ with respect to the black line.

References

[1] Esposito, G., *An introduction to quantum gravity*, arXiv:1108.3269v1

[2] Robotti, N. *The discovery of the electron*, Eur. J. Phys. 17 (1996) 133-138

[3] Dosch, H.G., Volkhard, F.M., Sieroka, N., *Quantum Field Theory, its Concepts Viewed from a Semiotic Perspective*, Universität Heidelberg, Springer 2005

[4] Popper, K., *The Logic of Scientific Discovery*, translated from German, *Logik der Forschung*, Routledge Classics, 2002

[5] Quigg, C., *Beyond the Standard Model in many directions*, arXiv:hep-ph/0404228v1, 2004

[6] Howl, R., King, S.F., *Planck Scale Unification in a Supersymmetric Standard Model*, arXiv:0705.0301v2, 2007

[7] Martin, S.P. *A Supersymmetry Primer*, arXiv:hp-ph/9709356v5, 2008

[8] Erler, J., Langacker, P., *Electroweak Model and Constraints on New Physics*, arXiv:hep-hp/0407097v1, 2004

[9] Cottingham, W.N., Greenwood, D.A., *An introduction to the Standard Model of particle physics*, Cambridge University Press, 2008

[10] Pich, A., *The Standard Model of Electroweak Interactions*, arXiv:hep-ph/0502010v1, 2005

[11] ATLAS Collaboration, *Charged-particle multiplicities in pp interactions at sqrts* = 900 *GeV measured with the ATLAS detector at the LHC*, Phys. Lett. B 688, 1, $21 - 42$, arXiv:1003.3124v2, 2010

[12] The ISOLDE facility, http://isolde.web.cern.ch/isolde/

[13] Wenninger, J., *Parameters and operation plans for 2011*, 2nd Evian 2010 Workshop on LHC Beam Operation, 2010

[14] LHC beam department, *Chapter 2 - Beam parameters and definitions*, http://lhc.web.cerb.ch/lhc/

[15] ATLAS Tile Calorimeter Collaboration, *Tile Calorimeter design Report*, CERN/LHCC, 1996

[16] ATLAS Collaboration, *Studies of the performance of the ATLAS detector using cosmic-ray muons*, Eur. Phys. J. C 71 1593, 2011

[17] Particle Data Group, *Passage of particles through matter*, Review of Particle Physics, 2002

[18] Wang, J., *Alignment of the ATLAS Inner Detector Tracking System*, arXiv:0910.5156v1, Uxbridge, UK, 2011

[19] The ATLAS Collaboration, *Expected Performance of the ATLAS Experiment, Detector, Trigger and Physics*, CERN-OPEN-2008-020

[20] Resende, B., *Muon identification algorithms in ATLAS*, EPS-HEP, 2009

[21] The ATLAS Collaboration, *Readiness of the ATLAS liquid argon calorimeter for LHC collisions*, Eur. Phys. J. C, 2010

[22] Green, D., *At the leading edge: the ATLAS and CMS LHC experiments*, World Scientific Publishing, 2010

[23] Kleinknecht, K., *Detectors for particle radiation, second edition*, Cambridge University Press, 1998

[24] The ATLAS Collaboration, *Measurement of Missing Transverse Energy*, CERN-OPEN-2008-020

[25] Rossetti, V., *Commissioning of the ATLAS Tile Hadronic Calorimeter with cosmic muons, single beams and first collisions*, ATL-TILECAL-PROC-2010-009

[26] Lampl, W., et al., *Calorimeter Clustering Algorithms: Description and Performance*, ATL-LARG-PUB-2008-002, 2008

[27] ATLAS Collaboration, *Performance and Missing Transverse Momentum Reconstruction in Proton-Proton Collisions at* $\sqrt{s} = 7\ TeV$ *with ATLAS*, arXiv:1108.5602, CERN, 2011

[28] Rauscher, F., *Calibration and Performance of the precision chambers of the ATLAS muon spectrometer*, ATL-MUON-SLIDE-2011-306, 2011

[29] Borroni, S., *Study of the Performance of the ATLAS Muon Spectrometer*, INFN Roma1, CERN, 2011

[30] Limper, M., *Track and vertex reconstruction in the ATLAS inner detector*, CERN-THESIS-2009-061, 2009

[31] Hassini, S., et al., *Muon identification algorithms in ATLAS*, NIM A572, 2007

[32] Adams, D., et al., *Track reconstruction in the ATLAS Muon Spectrometer with MOORE*, ATL-SOFT-2003-007, 2003

[33] ATLAS Collaboration, *Muon Reconstruction Performance*, ATLAS-CONF-2010-064

[34] UA2 Collaboration, Bagnaia, P., et al., *Evidence for* $Z^0 \rightarrow e^+e^-$ *at the CERN* $p\bar{p}$ *collider*, Phys. Lett. B129, 1983

[35] Casadei, D., *Statistical methods used in ATLAS for exclusion and discovery*, arXiv:1108.2288v1

[36] ATLAS Collaboration, *ATLAS Event Displays from 2010 and 2011 Collision Data*, https://twiki.cern.ch/twiki/bin/view/AtlasPublic/EventDisplayPublicResults#Candidate_W_decays_to_electron_o

[37] ATLAS Collaboration, *Observation of* $W \rightarrow l\nu$ *and* $Z \rightarrow ll$ *production in proton-proton collisions at sqrt(s) = 7 TeV with the ATLAS detector*, ATLAS-CONF-2010-044, 2010

[38] Bock, P., *Computation of confidence levels for search experiments with fractional event counting and the treatment of systematic errors*, J. High Energy Phys. 01 080, 2007

[39] ATLAS Collaboration, Aad, G., et al., *The ATLAS experiment at the CERN Large Hadron Collider*, JINST 3, 2008

[40] Karyukhin, A., Solodkov, S., Solovyanov, O., Starchenko, J., Wilkens, H., *Laboratory 2B: Characterization of the optics properties of a scintillating plastic Tile read by WLS fibres using 90-Sr source*, 2011

[41] Leo, W.R., *Techniques for nuclear and particle physics experiments*, Springer-Verlag, 1987

[42] Clement, C., *figure: A Tile Calorimeter module and the corresponding optics.*, Tile kalorimetern, Stockholms universitet

[43] Adragna, P., et al., *A PMT-Block Test Bench*, arXiv:physics/0605074v1, 2006

[44] Costanzo, D., et al., *The PMT-Block Test Bench Developed in Pisa*, ATL-TILECAL-2000-012, 2000

[45] ATLAS Tile Calorimeter, *Approved Tile Calorimeter Plots*, `https://twiki.cern.ch/twiki/bin/view/AtlasPublic/ApprovedPlotsTile#Detector_Status`

[46] Pina, J., et al., *The TileCal Detector Control System*, Proceedings of ICALEPCS07, 2007

[47] Calafiura, P., *The athena control framework in production, new developments and lessons learned*, CERN, 2005

[48] ATLAS TileCal, *TileCal public plots 2010 Collisions*, CERN, 2011

[49] ATLAS TileCal, *Commissioning of the ATLAS tile calorimeter LASER calibration system*, ATL-COM-TILECAL-2010-014, 2010

[50] Usai, G., *Signal Reconstruction of the ATLAS Hadronic Tile Calorimeter: implementation and performance*, ATL-TILECAL-PROC-2010-008, CERN, 2010

[51] Fullana, E., et al., *Optimal Filtering in the ATLAS Hadronic Tile Calorimeter*, ATL-TILECAL-2005-001, 2005

[52] Calkins, R., *The ATLAS Tile Calorimeter performance at the LHC*, CERN, 2011

[53] ATLAS TileCal, *Testbeam studies of production modules of the ATLAS Tile Calorimeter*, ATL-COM-TILECAL-2009-004, 2009

[54] Helmer, R.G., Chechev, V.P., *Table de Radionucléides*, LNE-LNHB/CEA, 2007

[55] ATLAS TileCal, *Integrator based readout in Tile Calorimeter of the ATLAS experiment*, ATL-TILECAL-PROC-2011-010, 2011

[56] ATLAS TileCal, *ATLAS tile calorimeter LASER calibration system*, ATL-TILECAL-INT-2010-001, 2010

[57] ATLAS TileCal, *A Charge Injection System for the TileCal CAEN ADCs*, ATLAS-TILECAL-NOTE-82, 1996

[58] ATLAS TileCal, *Performance and Calibration of the TileCal Fast Readout Using the Charge Injection System*, ATL-TILECAL-INT-2008-002, 2008

[59] ATLAS Collaboration, *Readiness of the ATLAS Tile Calorimeter for LHC collisions*, Eur. Phys. J. C 70: 1193-1236, 2010

[60] Kuhn, M.G., *Leap-second considerations in distributed computer systems*, Colloquium on the UTC timescale, 2003

[61] ROOT TTree, `http://root.cern.ch/root/html/TTree.html`

[62] ATLAS TileCal, *The ATLAS Hadronic Tile Calorimeter: From Construction Toward Physics*, IEEE TRANSACTIONS ON NUCLEAR SCIENCE, VOL. 53, NO. 3, 2006

[63] Dotti, A., Santoni, C., Usai, G., Weng, Z., *Calibration of the ATLAS hadronic barrel calorimeter TileCal using 2008, 2009 and 2010 cosmic-ray muon data*, ATL-TILECAL-PROC-2011-005, 2011

[64] Medina, C., *Intercalibration of the Intermediate Tile Calorimeter using 2009 cosmic rays data*

[65] Salzburger, A., *The ATLAS Track Extrapolator Package*, ATL-SOFT-PUB-2007-005

[66] Weng, Z., *TileCal response stability to Collision Muon*, `https://indico.cern.ch/getFile.py/access?contribId=12&resId=0&materialId=slides&confId=125280`, Jul-2011

[67] Dekking, F.M., et al., *A Modern Introduction to Probability and Statistics*, Springer, 2005

[68] Ellis, S.D., Soper, D.E., *Successive Combination Jet Algorithm For Hadron Colliders*, Phys. Rev. D 48, 3160-3166, 1993

[69] Salam, G., *Jets at Hadron Colliders* (`http://indico.cern.ch/conferenceDisplay.py?confId=115078`), CERN, Geneva, 2011

[70] Bentvelsen, S., Meyer, I., *The Cambridge jet algorithm: features and applications*, Eur. Phys. J. C 4, 623-629, 1998

[71] Salam, G., *QCD at hadron colliders, Maria Laach Herbtschule für Hochenenergyphysik*, `http://www.lpthe.jussieu.fr/~salam/repository/talks/2010-MariaLaach-lecture1.pdf`, 2010

[72] Cacciari, M., Salam, G., Soyez, G., *FastJet package*, `http://fastjet.fr`

[73] Seymour, M.H., *Jets in QCD*, arXiv:hep-ph/9506421v2, CERN, Geneva, 1995

[74] Bethke, S., *Vorlesung: Physik mit höchstenergetischen Teilchenbeschleunigern: QCD, Strukturfunktionen*, Jets, TU München, 2011

[75] Soyez, G., *Defining jets at the dawn of the LHC*, `http://het.epfl.ch/data/Soyez.pdf`, EPFL, Lausanne, 2010

[76] ATLAS collaboration, *Jet energy scale and its systematic uncertainty in proton-proton collisions at* $\sqrt{s} = 7$ *TeV with ATLAS 2010 data*, ATLAS-CONF-2011-032, 2011

[77] ATLAS collaboration, *Measurement of multi-jet cross sections in proton-proton collisions at a* 7 *TeV center-of-mass energy*, arXiv:1107.2092v2, 2011

[78] Griffiths, D., *Introduction to Elementary Particles*, WILEY-VCH Verlag GmbH & Co. KGaA, Weinheim, 2004

[79] Baur, U., Glover, E.W.N., *Electroweak interference effects in two-jet production at* $p\bar{p}$ *colliders*, Phys. Let. B 232-4, 1989

[80] Salam, G., *Towards Jetography*, arXiv:0906.1833v2

[81] Miller, J., *The Method of Least Squares*, `http://web.williams.edu/go/math/sjmiller`

[82] Giangiobbe, V., *Variation of the TileCal cells response as a function of time*, ATLAS-PLOT-TILECAL-2011-010

[83] Higgs, P.W., *Broken Symmetries, Massless Particles and Gauge Fields*, Physical Review Letters 12 (2): 132

[84] Englert, F., Brout, R., *Broken Symmetry and the Mass of Gauge Vector Mesons*, Physical Review Letters 13(9): 321-323

[85] Higgs, P.W., *Broken Symmetries and the Masses of Gauge Bosons*, Physical Review Letters 13 (16): 508-509

[86] Guralnik, G.S., Hagen, C.R., Kibble, T.W.B. *Global Conservation Laws and Massless Particles*, Physical Review Letters 13 (20): 585-587